The Influence of Substrate Micro- and Nanotopographies on Essential Cell Functions

Dissertation

zur Erlangung des Naturwissenschaftlichen Doktorgrades

der Julius-Maximilians-Universität Würzburg

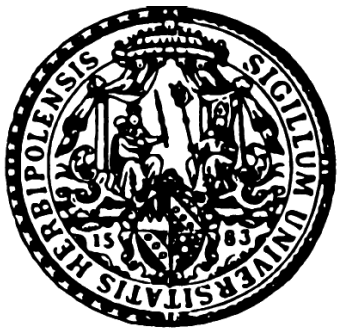

vorgelegt von

Martin Emmert

aus Gnodstadt

Würzburg 2022

Diese Dissertation wurde in der Zeit von Oktober 2014 bis November 2022 am Fraunhofer Institut für Silicatforschung ISC, unter der Leitung von Prof. Dr. Gerhard Sextl, Lehrstuhl für Chemische Technologie und Materialsynthese der Julius-Maximilians-Universität Würzburg, erstellt.

Eingereicht bei der Fakultät für Chemie und Pharmazie am

Gutachter:innen der schriftlichen Arbeit

1. Gutachter: Prof. Dr. Gerhard Sextl
2. Gutachterin: Prof. Dr. Doris Heinrich

Prüfer:innen des öffentlichen Promotionskolloquiums

1. Prüfer: Prof. Dr. Gerhard Sextl
2. Prüferin: Prof. Dr. Doris Heinrich
3. Prüfer: Prof. Dr. Volker Engel

Datum des öffentlichen Promotionskolloquiums

05.05.2023

Doktorurkunde ausgehändigt am

Danke

Ich möchte ich mich bei allen bedanken, die zum Gelingen dieser Arbeit beigetragen haben.

An erster Stelle danke ich meinem Doktorvater und Studiengangsleiter Herrn Prof. Dr. Gerhard Sextl, der mir ermöglicht hat, meine Promotion am Fraunhofer ISC durchzuführen und während meiner fast 10 Jahre am Institut (vom Praktikanten bis zum Doktoranden) und als Leiter der Lehrstuhls für Materialsynthese stets ein offenes Ohr für alle Anliegen und auch Probleme hatte, die sich im Alltag der Student:innen und Mitarbeiter:innen ergeben. Des Weiteren möchte ich ihm auch für die Erstellung des Erstgutachtens danken.

Frau Prof. Dr. Doris Heinrich danke ich ganz besonders, dass sie mir schon zur Masterarbeit die Chance gab, mich in ihrer neuen Gruppe zu beweisen und bei verschiedensten Themen ein unglaublicher Wissens- und Erfahrungsschatz (und auch Sparringpartnerin) war – egal ob es um Biophysik, Mikroskopie, Zellkultur, den Umgang mit Student:innen oder um Probleme und Lebensentscheidungen ging. Ihre unkomplizierte Art und Offenheit hat mich in vielen Dingen sehr weitergebracht und langfristig positiv beeinflusst.

Ganz herzlich bedanke ich mich auch bei Herrn Prof. Dr. Volker Engel für den netten, unkomplizierten Austausch und die Teilnahme als Prüfer im Promotionskolloquium.

Ein Dank geht auch an Dr. Peter Fischer, der im Promotionskolloquium die Rolle des Beisitzers übernahm.

Meinen ehemaligen Bürokolleg:innen Maria, Patrick, Max, Silke und Kai verdanke ich, dass ich all die Jahre immer gerne ins Büro gekommen bin, danke für die schöne Zeit - auch außerhalb der tatsächlichen Arbeit! Der Dank für die tolle Stimmung in der Gruppe geht natürlich auch an Sebastian, Timo und ihre Student:innen.

Meinen Student:innen Jutta, Eva, Moritz, Andreas und Dominik danke ich ganz besonders, da ich mich vollkommen auf sie verlassen konnte und sie alle einen Teil zum Gelingen dieser Arbeit beigetragen haben.

Bei allen Mitarbeiter:innen des Lehrstuhls für Chemische Technologie der Materialsynthese bedanke ich mich sehr herzlich für die nette Arbeitsatmosphäre und die Unterstützung bei chemischen Fragen.

Meinen ehemaligen ISC-Kolleg:innen Kathrin, Miranda und Walter danke ich dafür, dass sie mich als Praktikant so fürsorglich aufgenommen und mich all die Jahre als HIWI behalten haben. Ich habe in diesen Jahren fachlich und menschlich unglaublich viel gelernt!

Dr. Ferdinand Somorowsky danke ich für die Bereitstellung der Proben und die Unterstützung bei der Erstellung unserer Patentanträge und der Veröffentlichungen.

Außerdem möchte ich dem gesamten TERM-Team danken, die mich so nett in ihre Labore aufgenommen haben und immer hilfsbereit waren. Insbesondere danke ich Franziska, Christoph, Sebastian, Joachim und der damaligen Lehrstuhlinhaberin Prof. Dr. Heike Walles.

Meinen Eltern danke ich dafür, dass sie mich stets bedingungslos bei allem unterstützen, was ich tue - und meiner Schwester Barbara, dass sie mir auf meinem akademischen Weg immer wieder mit gutem Rat geholfen hat.

Und zuletzt gilt mein besonderer Dank natürlich Stephie, die mich in den ganzen Jahren bei der Erstellung dieser Arbeit begleitet und mich immer wieder motiviert hat, am Ball zu bleiben.

Abstract

The introduction of novel bioactive materials to manipulate living cell behavior is a crucial topic for biomedical research and tissue engineering. Biomaterials or surface patterns that boost specific cell functions can enable innovative new products in cell culture and diagnostics. This study aims at investigating the interaction of living cells with microstructured, nanostructured and nanoporous material surfaces in order to identify distinct systematics in cell-material interplay. For this purpose, three different studies were carried out and yielded individual effects on different cell functions.

Cell migration processes are controlled by sensitive interaction with external cues such as topographic structures of the cell's environment. The first part of this study presents systematically controlled assays to investigate the effects of spatial density and local geometry of micron scale topographic cues on amoeboid migration of *Dictyostelium discoideum* cells in quasi-3D pillar fields with systematic variation of inter-pillar distance and pillar lattice geometry. We can extract motility parameters in order to elucidate the details of amoeboid migration mechanisms and consolidate them in a two-state contact-controlled motility model, distinguishing directed and random phases. Specifically, we find that directed pillar-to-pillar runs are found preferably in high pillar density regions, and cells in directed motion states sense pillars as attractive topographic stimuli. In contrast, cell motion in random probing states is inhibited by high pillar density, where pillars act as obstacles for cell motion. In a gradient spatial density, these mechanisms lead to topographic guidance of cells, with a general trend towards a regime of inter-pillar spacing close to the cell diameter. In locally anisotropic pillar environments, cell migration is often found to be damped due to competing attraction by different pillars in close proximity and due to lack of other potential stimuli in the vicinity of the cell. Further, we demonstrate topographic cell guidance reflecting the lattice geometry of the quasi-3D environment by distinct preferences in migration direction.

We further investigate amoeboid single-cell migration on intrinsically nano-structured, biodegradable silica fibers in comparison to chemically equivalent plain glass surfaces. Cell migration trajectories are classified into directed runs and quasi-random migration by a local mean squared displacement (LMSD) analysis. We find that directed movement on silica fibers is enhanced in a significant manner by the fibers' nanoscale surface-patterns. Further, cell adhesion on the silica fibers is a microtubule-mediated process. Cells lacking microtubules detach from the fibers, but adhere well to glass surfaces. Knock-out mutants of myosin II migrating on the fibers are as active as cells with active myosin II, while the migration of the knock-out mutants is hindered on plain glass.

We investigate the influence of the intrinsically nano-patterned surface of nanoporous glass membranes on the behavior of mammalian cells. Three different cell lines and primary human mesenchymal stem cells (hMSCs) proliferate readily on nanoporous glass membranes with mean pore sizes between 10 nm and 124 nm. In both proliferation and mRNA expression experiments, L929 fibroblasts show a distinct trend towards mean pore sizes > 80 nm. For primary hMSCs, excellent proliferation is observed on all nanoporous surfaces. hMSC on samples with 17 nm pore size display increased expression of COL10, COL2A1 and SOX9, especially during the first two weeks of culture. In upside down culture, SK MEL-28 cells on nanoporous glass resist the gravitational force and proliferate well in contrast to cells on flat references. The effect of paclitaxel treatment of MDA MB 321 breast cancer cells is already visible after 48 h on nanoporous membranes and strongly pronounced in comparison to reference samples.

The studies presented in this work showed novel and distinct effects of micro- and nanoscale topographies on the behavior of various types of living cells. These examples display how versatile the potential for applications of bioactive materials could become in the next years and decades. And yet this variety of different alterations of cell functions due to topographic cues also shows the crucial part of this field of research: Carving out distinct, robust correlations of external cues and cell behavior is of utmost importance to derive definitive design implications that can lead to scientifically, clinically and commercially successful products.

Publications

This cumulative dissertation is comprised of three different publications, respective first authors are marked with * and contributions of each author are listed in detail at the beginning of each chaper:

Chapter III: "Amoeboid migration mode adaption in quasi-3D spatial density gradients of varying lattice geometry"

By Max Gorelashvili*, Martin Emmert*, Kai Friedrich Hodeck and Doris Heinrich
-- New Journal of Physics, Volume 16, July 2014

Chapter IV: "Nanostructured surfaces of biodegradable silica fibers enhance directed amoeboid cell migration in a microtubule-dependent process"

By Martin Emmert*, Patrick Witzel, Miranda Rothenburger-Glaubitt and Doris Heinrich
-- RSC Advances 7 (2017), Nr.10, S.5708–5714

Chapter V: "Modulation of Mammalian Cell Behavior by Nanoporous Glass"

By Martin Emmert*, Ferdinand Somorowsky, Jutta Ebert, Dominik Görick, Andreas Heyn, Moritz Wahl, Eva Rosenberger and Doris Heinrich
in Advanced Biology 5 (2021), Issue 7, 2000570

In addition, the studies described in Chapter V led to the following patent applications:

- US Patent Application #20190345443 "Method for the Culturing and Differentiation of Cells" (pending)
- EU Patent EP 3561045B1 "Verfahren zur Kultivierung und Differenzierung von Zellen" (granted)

As an addendum, a mini-review published during the course of this thesis is added at the end:

Chapter VII: "Challenges in tissue engineering – towards cell control inside artificial scaffolds"

By Martin Emmert*, Patrick Witzel* and Doris Heinrich
-- Soft Matter, 2016, 12, 4287–4294

I. INTRODUCTION

1. Motivation

1.1 The Problem: Translation Gap Between Research and Clinic

The knowledge of physiological processes is growing rapidly as more and more details of functional units inside the human body get elucidated. However, compared to the billions that are invested in biomedical research every year, very few revolutionary new materials, drugs, or treatments make it to the clinic. Although there is an abundance of technologic innovation coming from research institutions and industry, there is still a giant gap between research and translation into clinical practice[1].

One major reason for this gap lies in the standard methodologies of biomedical research: Most studies on cell behavior are performed with standards that have been developed in the 1960s. For most applications, 2D cell cultures on surfaces made of polystyrene and borosilicate glass cannot reflect the complexity of the physiological, three-dimensional environment inside the human body, where a cell is exposed to a wide range of stimuli[2].

Nevertheless, simple 2D culture is - to this date - still the standard for *in vitro* investigations in the medical device and pharmaceutical industries. A very illustrative example is drug development: Although 2D cell cultures help to robustly identify active agents that have effects on human cells in the first place, many drug candidates fail at the point of translation from *in vitro* to *in vivo*. Failures at this point are not only financially an issue – even more important,

the lives of test animals are often sacrificed for drugs that in the end lack the desired effects[3,4].

However, cell-based research is still the approach that should be followed for biomedical investigations, as most cell types can be easily expanded in cell culture at a moderate cost and in large scales. To yield more realistic results, the focus should be on techniques that mimic functional parts of physiological systems to have more reliable results for translational medicine. Good examples are clearly defined co-cultures to include cell-cell signalling and mechanical interaction[5] or functional surfaces that influence cell behavior by soluble or insoluble cues.

The obvious solution to this problem would be cell culture in a physiological 3D environment similar to tissues in the human body. In accordance with this assumption, cell studies inside 3D models that either mimic biological tissues or are directly derived from biological matrices benefit from a more realistic cell behavior. Unfortunately, biologically derived/produced 3D culture environments such as matrices or cell spheroids have significant disadvantages for use in large-scale high-throughput studies and in standard cell culture[6]:

1. High variability
    a. Matrices: Natural variance due to biological production
    b. Spheroids: Variations due to different history / passage of cultured cells
    c. Number of cells cannot be exactly counted
2. Significantly higher costs
    a. Costly production from biological starting materials compared to cheap, industrial plastic production for 2D culture substrates
    b. More time intensive cell culture
        i. Modifications to standardized culture methods needed
        ii. No cheap, automatic processing possible
3. Limited storage possibilities

   a. Matrices can lose some of their features upon freezing / thawing and need additional storage in the freezer
   b. Spheroids: no storage possible
4. Poor optical characteristics in everyday laboratory use due to dense tissue structure (microscope, optical evaluation)

In contrast, the advantages of simple 2D cultures in transparent Petri dishes, culture bottles, or corrugated plates are obvious:

1. Standardized, simple handling in the sterile bench
2. Planar culture surface
3. Homogeneous cell colonization
4. Optical characteristics suitable for microscope and optical tests
5. Autoclavability or sterilizability
6. Large-scale pre-production and storage

Due to this dilemma between easy handling (2D) and physiological cell behavior (3D), there is a great need for new materials and products which fulfil the above-mentioned advantages, but induce a more realistic cell behavior. In all areas where *in vitro* investigations are carried out on cells, novel, more physiological culture surfaces that map a certain cell behavior better than current surfaces or can accelerate biological processes would be a major step forward. Even more beneficial, research should aim at an easy integration into existing standard laboratory equipment and high-throughput experiments to facilitate existing processes and save both time and money during drug development.

1.2 The Missing Link: Novel Bioactive Materials

For all these approaches, one thing is desperately needed: Novel bioactive materials. In the past decades, biomaterials research has created an abundance of biocompatible materials and today, there are many implantable devices that

are either completely biodegradable (e.g. degradable suture material) or bioinert[7] – but not bioactive. Or even worse, they show adverse effects in long-term use. For example, the major caveats of hip endoprostheses are material-intrinsic: Ceramic-metal bearings have a higher risk of fractures upon traumatic incidents[8]. For metallic-metallic bearings, there is a constant abrasion of potentially allergenic[9] or toxic[10] particles that can cause chronic local inflammation and induce severe osteolysis[11]. This is why the focus in biomaterials research is turning more and more on bioactivity instead of just biocompatibility. Major aims in this field of research are materials that specifically modulate cell functions into a certain direction:

- Maximized cell adhesion of specific cell types
    - E.g. for implants to regenerate bones/cartilage and for the culture of sensitive cells like stem cells
- Minimized general cell adhesion
    - E.g. for medical stents or wound dressings
- Increased/decreased cell migration
    - E.g. for scaffolds after tissue ruptures
- Minimized/maximized protein adhesion and deposition
    - E.g. mimicking specific parts of the ECM
- Minimized encapsulation
    - E.g. for bone prostheses
- Active bio-degradation and release of drugs or nutrients
    - E.g. for scaffold that will be replaced by tissue-ingrowth
- Optimization for different chemical milieus in the human body
    - E.g. scaffolds that withstand the acidity in the stomach
- Alteration of cellular gene expression
    - E.g. to suppress the triggering of further immune reaction
- Induction of cell differentiation
    - E.g. for distinct stem cell differentiation *in vitro* and *in vivo*

These versatile requirements are the reason why studying the cell-material interface and its effect on single cells and multicellular systems is one of the most important topics of biomedical research. In this highly multidisciplinary field at the intersection of chemistry, physics, materials science, mathematics and biology, the number of publications is exponentially growing since the 1980s on PubMed, the standard resource for medical research. In comparison, classic medical research topics like “bone”, “cancer” or “skin” have a rather linear increase in publication numbers. This underlines the growing importance of bioactive materials for medical research.

2. Aim & Outline of this Work

This study aims at investigating the interaction of living cells with microstructured, nanostructured, and nanoporous material surfaces in order to identify distinct systematics in cell-material interplay. For this purpose, three different studies were carried out and yielded individual effects on different cell functions.

After the motivation and outline given in **Chapter I**, **Chapter II** will lead into the topic by giving an overview on the scientific background on the underlying mechanisms and factors involved in cell-material interaction.

Chapters III-V contain the three publications published during the course of this cumulative dissertation.

Chapter VI closes the main part of this thesis with a joint discussion and the deduction of conclusions and implications for future studies and potential applications.

As an addendum outside of the main research topic, **chapter VII** displays the content of a mini-review published during the writing of this thesis. It gives

insight into the challenges of tissue engineering research and the investigation of smaller scale processes inside living cells.

2.1 Cell Migration Inside Controlled Microtopographies

In the first part of this work, cell migration was probed by systematically controlled assays to assess the influence of symmetric and asymmetric micron-scale topographic cues. Polydimethylsiloxane (PDMS) micro-pillar fields were fabricated, consisting of lattices of trigonal (isotropic) and hexagonal/honeycomb (anisotropic) geometry with defined density gradients, providing spatially controlled quasi-3D environments for cell migration. PDMS is a comprehensively characterized and commonly used material, which provides a well-controllable model environment for systematic cell migration studies[12,13].

The eukaryotic slime mold *Dictyostelium discoideum (Dd)* was utilized to study amoeboid migration inside the described PDMS pillar fields. Due to its simple cell culture conditions and its fast migration velocities, it has become the most common model organism for the study of amoeboid cell migration[14].

2.2 Cell Migration on Nanostructured Surfaces

The second part of this work is dedicated to elucidating the interaction of living cells with nanostructured surfaces. As cellular processes like filopodia are in the same size range as surface nanoscale features, the migration can be highly influenced by nanostructures present at the substrate surface.

In this study, biodegradable, intrinsically nanostructured silica fibers were used as substrate for cell migration. The fibers are derived from a sol-gel process and were initially designed to fabricate fleeces that are CE-certified for the use as a wound dressing[15]. This work is based on a previous study on amoeboid migration on single fibers from these fleeces and further investigates

the mechanism of adhesion utilizing mutant cells and cytoskeleton-altering drugs. Again, *Dd* cells were used for the migration experiments.

2.3 Modulation of Mammalian Cell Behavior by Nanoporous Glass

In the human body, there are various types of nanoporous membranes and surfaces that are crucial for many physiological processes: For this purpose, the last and biggest part of the thesis is dedicated to investigating the interaction of living cells with nanoporous glass membranes[16]. Glasses are an interesting material class for biomedical research and have been used in biological applications for decades. Having a long tradition in glass fabrication, processing techniques, and chemical functionalization, Fraunhofer ISC will greatly benefit of novel applications for nanoporous glasses in biomedical application. For this purpose, the reaction of various cell types to the nanoporous glass membranes was probed. This includes the investigation of cell adhesion, proliferation, gene expression, and cell differentiation. In addition, the reactivity to a microtubule-altering drug that is part of the standard treatment for different cancer types was tested in a functional drug assay.

For the experiments in this study, different types of cell lines were utilized. L929 mouse fibroblasts are one of the most common cell lines in today's cell culture. In fact, they are the gold standard for cytotoxicity assays and biocompatibility evaluation studies and were used for proliferation and gene expression experiments in this study. For stem cell differentiation experiments, primary human mesenchymal stem cells extracted from the hip joints of two patients were seeded onto the samples. The melanoma cell line SK-MEL-28 was chosen for adhesion experiments in reaction to nanoporous glass membranes. MDA-MB-321 breast cancer cells were utilized for functional tests on the reaction of tumor cells to a microtubule-diminishing anti-cancer drug.

II. Scientific Background

Chapters II.1 and II.2.5 are partly based on the published mini-review

"Challenges in tissue engineering – towards cell control inside artificial scaffolds"

by Martin Emmert, Patrick Witzel and Doris Heinrich

in Soft Matter, 2016, 12, 4287-4294.

The complete manuscript is part of this work as Part VII (Addendum).

1. Introduction

Managing the reaction of living cells to material surfaces is the crucial aspect of biomaterials research. If essential cell functions are influenced in a direction that is detrimental to the intended use, a material is not suitable for application. Thus, a thorough understanding and analysis of different cell functions in reaction to material surfaces is of utmost importance for this research area, especially the most vital cell functions adhesion, migration, proliferation, gene expression, and cell differentiation.

So what are the key components of this interface interaction on both sides? As for every interface, a high-level look leaves us with two components: Cell and material. Chapter II.2 will have a closer look on the biological concepts and the low-level mechanical and biological building blocks of these two interfacing systems in nature and their influence on different cell functions. After that, Chapter II.3 will provide an overview on the material preparation and analysis methods applied for this work to complement a comprehensive introduction into the three studies carried out in Chapters III-V.

To ensure the viability of living cells, a great variety of biochemical and physical processes have to be coordinated[17]. This sophisticated out-of-equilibrium system is orchestrated by complex interdependent processes within the extremely crowded and active cell interior. Chemical and physical signals in and outside of cells determine biological processes, such as cell migration and morphogenesis[18]. Mechanisms of cell functions are based on highly organized intracellular structures and systems, ranging in size from the nano- to the micron-scale. These structures are intrinsically dynamic, exhibiting active and passive transport phenomena to pass on information between different regions inside the cell[19].

While the genome provides the blueprint for all vital processes, the interaction of living cells with their environment determines cell functions. Not only

molecular concentration gradients[20] but also mechanical interactions with 3D scaffolds of the extracellular matrix determine functionality of living cells, such as adhesion, migration, proliferation, and differentiation[21].

A new insight into disease mechanisms is of utmost importance to develop novel strategies for curing diseases like neuronal degeneracy[22,23], cancer[24], and inflammation[25] or to identify the mechanistic origins of rare diseases. Additionally, this understanding will promote the development of innovative cell guiding strategies, e.g. for scaffold design in tissue engineering and innovative cell sorting techniques for diagnostic purposes.

2. Biological Systems & Cell Functions

2.1 The Extracellular Matrix

In the human body, cells are surrounded by a physical, three-dimensional scaffold, generalized as the extracellular matrix (ECM). All types of tissue are constituted by a specific combination of ECM and cells. The ECM mainly consists of collagen, glycoproteins, fibrin, fibronectin, glycosaminoglycans, and other macromolecules[26,27]. The exact composition differs around different types of tissue and organs, evolutionarily tailored towards the specific requirements for homeostasis, morphogenesis, and cell differentiation inside the respective area of the body. Besides providing cell adhesion and structure within the living organism, the ECM constituents and their density and spatial arrangement also have a triggering function for various essential biochemical and biomechanical pathways[28,29].

Tissue in the human and mammalian body can be subdivided into connective, muscle, nervous, and epithelial tissue. The ECM components of most connective tissues are mainly secreted by fibroblasts who build up the tissue substance. In more specialized connective tissues like bone or cartilage, the ECM is produced

by highly differentiated cells like osteoblasts or chondroblasts[30]. Cells in connective tissues are usually very sparsely distributed and are often not in contact with each other – with the tissue taking up most of the mechanical load[31]. Thus, cell-ECM interfaces are predominant in most connective tissues. In epithelial tissue, a more complex interaction is observed: Here, the stability upon deformation is maintained mainly by cell-cell adhesions, while cell-ECM interaction plays a crucial role in cell polarization and differentiation[32]. These are only exemplary types of interaction – but they display the essential importance for biomaterials research to take the specific physiological interactions of the desired applications and utilized cell types into account. For this work, only cell-matrix adhesion is interesting as the studies investigate direct cell-material interaction.

2.2 The Cytoskeleton

In order to understand the mechanics of cell adhesion and migration, it is necessary to give an overview on the underlying structure that enables a cell to interact with its surroundings, the cytoskeleton. Its main functions are:

1. The spatial organization of the cell components and effective intracellular transport
2. The physical and biochemical connection to the cell's vicinity
3. Force generation at the nanoscale for migration and shape change

To provide these functions, the cytoskeleton is comprised of different, highly dynamic structures that are undergoing constant change[21]: Figure 1 gives a schematic illustration of the three major filament structures of the cytoskeleton. They are build up by monomers that possess a polarity that is conserved in the resulting polymers and can be used by molecular motors like kinesin, dynein, or myosin[33]. Microtubules (green in Figure 1), the most rigid of cytoskeletal polymers, are crucial pathways for intracellular protein and

material transport and serve as central nodes for these processes. In addition, they form the spindle apparatus utilized for chromosome separation during cell division[34]. They can span the whole diameter of a cell and are subject to constant change and reorganization, depending on the regulation of cell functions and the resulting needs for transport of building blocks. Actin filaments (red in Figure 1) are initially much less rigid than microtubules, but can form various architectures of bundled networks that are stabilized by effective crosslinking. Branched, gel-like actin networks can be found in the cell cortex and are very important in cell division, while contractile bundles are present in actin stress fibers. Tight parallel bundles are found in protrusions build up for phagocytosis or inside filopodia, small, finger-like protrusions that are build up for exploring the cell's vicinity[21]. Intermediate filaments are mainly needed to support and stabilize the cell structure and can be made up of different proteins like desmin, keratin, vimentin, lamine, or neurofilaments[35,36].

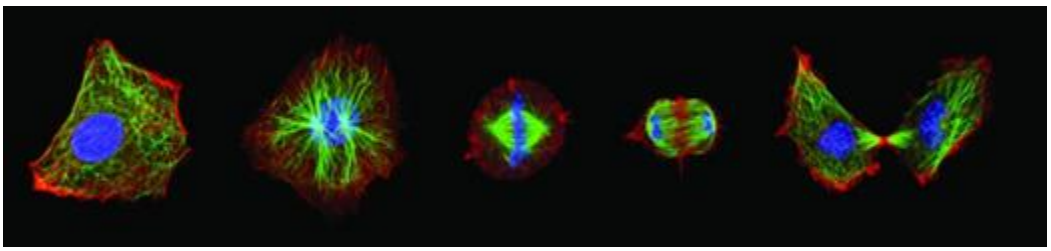

Figure 1: Microscopy images of an eukaryotic cell undergoing mitosis (cell division), with stainings for microtubules (green), actin (red) and DNA (blue)[37].

2.3 Cell Adhesion

Cell adhesion is one of the most crucial mechanisms in the human body. Without cell-matrix adhesion, i.e. cells adhering to tissue or the ECM, and cell-cell adhesion, i.e. cells adhering to each other, there would be no stability in the body. Basically, there are two types of cell adhesion behavior: Adherent cells and non-adherent cells. Prominent non-adherent cells are all types of blood cells and immune cells that are floating around in the blood stream.

Interestingly, cell adhesion is a very dynamic process: Non-adherent leukocytes can quickly react to chemotactic cues, e.g. when pathogens invade a skin wound and the surrounding tissue cells secret chemokines to attract cells of the immune response. In reaction to these chemokines, leukocytes become adherent to the wall of the nearest blood vessel and then exit the vessel to perform amoeboid migration through the extracellular matrix to enter and clear the wound site[26,38–41] (for details, see Chapter 2.5). The majority of cells in living organisms is adherent. Adherent cells live inside the ECM or form functional units themselves to build up different types of tissues, e.g. organs, bones, blood vessels, and the skin. Examples for adherent cells are fibroblasts, neural cells, or epithelial cells. The dynamic cell adhesion in the three-dimensional environment of tissues and organs is very different from behavior in 2D cell culture, where a more static adhesion to the flat surface takes place, while more than half of the cell body is exposed to the fluid cell culture medium instead of being connected to other cells or the ECM[42]. Standard cell culture surfaces are treated for increased adhesion of media proteins onto the surface, for example fibronectin or vitronectin[43].

For exploring its environment during adhesion and migration, a cell builds up lamellipodia and filopodia, actin-rich protrusions that are extended at the leading edge. While lamellipodia are wide, sheet-like protrusions made of dense meshworks of cross-linked actin filaments, filopodia are small, finger-like protrusions consisting of tight parallel bundles of filamentous actin with diameters of 100-300 nm. Due to their sensory machinery, filopodia are important in many physiological processes like contact guidance and chemotaxis. They are often the pioneering cellular processes that probe the extracellular environments in order to evaluate the possibilities for cell adhesion. Their signaling cascades propagate to the inside of the cell to induce changes in the cytoskeleton and the transport processes necessary for the generation of traction forces for the movement of the cell body[44,45]. At the tips of filopodia, proteins for creating first adhesion points are concentrated,

namely integrins and cadherins. Due to this, filopodia act as "sticky fingers" that probe the environment to create first contact points to a novel surface inside the human body or *in vitro*[46]. In addition, filopodia also establish first contacts to neighboring cells to initiate retraction or the buildup of cell-cell adhesion sites. In cell culture, this can be very important, for example when culturing epithelial cells: An underlying substrate that cannot provide the necessary stability or flexibility for the buildup of a stable epithelial cell layer with an active barrier function is not suitable for application[47].

The specific interplay of different cell types with a material's interface can be very different. On stiffer substrates, cells tend to have more and stronger adhesion sites than cells on softer substrates. On the latter, cells exhibit softer and more dynamic adhesion sites. Thus, understanding the mechanisms of cell adhesion in reaction to a material surface is crucial for the development of bioactive materials that actively trigger and support certain cell functions and to influence tissue growth with the surface of a scaffold[48].

The modulation of these processes by a bioactive material is decisive for potential applications in research and medical products: For example, if a material surface exhibiting topographic features diminishes cell adhesion, it is not suitable for most cell culture or drug assays. However, it could be tested for applications where cell adhesion needs to be minimized, e.g. in metal stents and conductive materials[49]. In addition, a minimized cell adhesion area has been shown to trigger the differentiation of specific cell types such as human pluripotent stem cells[50].

2.4 Cell Proliferation

Another vital cell function a biomaterial needs to support is cell proliferation, which is a direct consequence of repeated cell division and cell growth. As adherent cells that undergo mitosis detach most of their body from their

environment during cell division, mitosis is greatly dependent on cell adhesion and migration: Only materials that allow for the active disassembly of adhesion complexes, the post-mitotic re-adhesion, and repulsive migration of the daughter cells[51] can be selected for long-term experiments or utilized as implants. After mitosis, the two daughter cells become fully adherent again and enter their own cell cycle.

The cell cycle of eukaryotic cells is divided into two distinct phases (Figure 2): The interphase between cell divisions and mitosis, the orchestrated process of division into two "daughter" cells. Following cell division, the cell undergoes an initial growth phase (G1), where organelles and cytoskeletal components of the freshly divided cells grow and organize. During the interphase, a cell grows and its chromosomes and centrosomes are duplicated. After that, the cell divides in an orchestrated process: In the prophase, the duplicated chromatin is condensed and the nucleus gets fragmented. Next, in the metaphase, the chromosomes align and attach to the microtubules connected to the two centrosomes. During anaphase and telophase, the chromosomes first segregate and are transported towards the centrosomes. Then, new cell membranes are built up by cytokinesis and the daughter cells finally segregate.

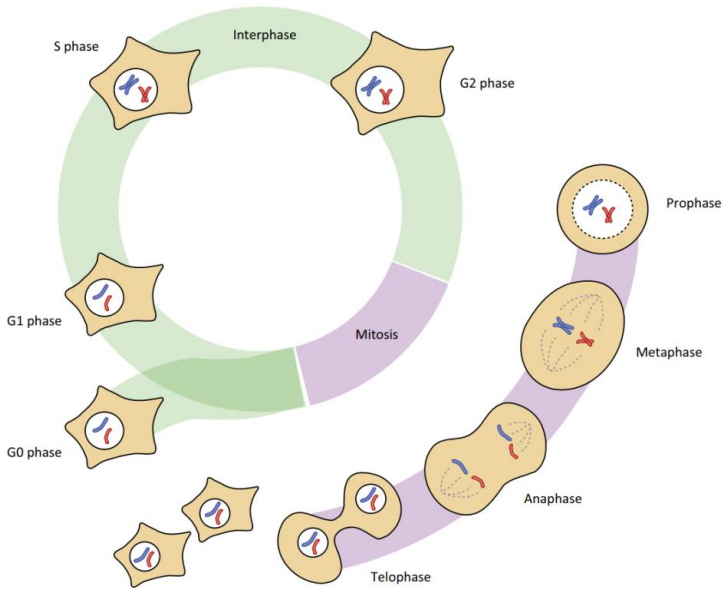

Figure 2: Schematic illustration of the cell cycle in eukaryotic cells[52].

If one of those processes is disturbed or diminished by soluble or insoluble components of the underlying substrate, the cell will either not divide at all or undergo erratic division, potentially leading to apoptosis and genetically altered daughter cells that might be the starting point for tumor growth[53,54].

2.5 Cell Migration

The ability of cells to migrate is an essential cell function for innumerable physiological processes, starting with the development of first cell clusters and tissue structures in embryonic development, the organization inside multicellular tissues, and the homeostasis of the organism.

There are four factors governing cell migration mechanisms[55]:

1. Adhesion
2. Material stiffness
3. Cell confinement
4. Substrate topography

In 2D cell culture on flat substrates, only material stiffness and the adhesion mechanism resulting from adhesion ligand density are influencing cell migration. In migration studies carried out in this work, the influence of cell confinement and substrate topography on amoeboid migration was investigated with a model organism. More detailed introductions on amoeboid migration and the respective topics can also be found in the respective chapters III.2 and IV.2.

In the living organism, amoeboid cell migration plays a major role in both physiological and pathological situations. The human immune response is highly dependent on the ability of leukocytes to leave the blood vessels in response to chemical signals, crawl through tissues to their point of destination, and neutralize pathogens. In contrast, gene defects in the

regulation of immune cell migration can cause chronic inflammatory diseases when immune cells infiltrate random parts of the human body and get activated to create a toxic environment. Instead of killing intrusive bacteria or destroying pathogens, they can cause chronic pain and severe damage in healthy tissue[56,57]. Tumor metastasis is a very prominent example of the malignancy of pathologic aberrations in cell migration: Once a certain tumor size is reached and with ongoing mutations, the tumor gets closer to the basement membrane and blood vessels[58]. Due to mutations, cells can undergo epithelial-mesenchymal transition (EMT) and become motile, allowing them to exit the tumor and crawl through the surrounding tissues. To become even more motile, some cells undergo amoeboid-mesenchymal transition (AMT), allowing them to increase their migration speed and contractility[59]. Eventually, they can penetrate the wall of a vessel and get carried away to be distributed to distant areas of the organism. There, they can become adherent again, proliferate, and build up metastasis. This plasticity of tumor cell migration makes amoeboid and general migration a very important topic, as the identification of near-physiological models for tumor cell migration build up by novel material surfaces could greatly facilitate cancer drug research.

Chapters 2.5.1 and 2.5.2 are published as part of the publication

"Challenges in tissue engineering – towards cell control inside artificial scaffolds" by Martin Emmert*, Patrick Witzel and Doris Heinrich -- Soft Matter, 2016, 12, 4287–4294 (see Chapter VII – Addendum)

2.5.1 Amoeboid Cell Migration

In the absence of external cues, motile amoeboid cells migrate by the formation of stochastically generated pseudopods. The current model assumes two alternating motility modes: a random probing mode and a directed, fast migration mode[60]. This efficient "search strategy" is highly dynamic and can be

characterized by distinct differences in the protrusion frequency and angle distribution of successive turns in the migration direction[61]. Cell velocity and shape analysis during these random migration phases led to simple models of amoeboid random walk[62]. In the last decade, a refined view emerged considering correlations between the cellular orientation and the migration direction[63–66]. In the presence of mechanical or chemical cues, the protrusions can be stabilized and trigger directed migration by cell polarization[67]. This specific type of cell migration is observed in several eukaryotic cell types, *e.g.* stem cells, specific immune cells, or metastatic tumor cells[68], which can travel long distances inside the complex tissues of the human body to reach their point of destination[69]. Thus, a profound understanding of the mechanisms governing amoeboid migration in 3D environments will facilitate novel approaches in diagnostics and therapy. It will give rise to the development of novel drugs in cancer therapy, targeting specific cytoskeletal parts or intracellular proteins that have been shown to promote tumor metastasis. Furthermore, the abilities for cell guidance by topographic cues will be of utmost importance for the 3D distribution of cells inside artificial scaffolds in tissue engineering.

2.5.2 Cell-Substrate Interactions in Amoeboid Migration

Spontaneous generation of pseudopods at random sites is a basic activity of vital cells and can be found in homogeneous cell migration environments lacking topographic and chemotactic stimuli. *D. discoideum* cells perform a special kind of random motion consisting of zig-zag-like motions over distances of about 20 µm and a subsequent change in the direction[61,70,71]. This motion behavior is correlated with the dynamics of pseudopod spreading. Pseudopods protrude constantly for several microns and stop abruptly. Then, the cell rear is retracted by unbinding from the substrate, decreasing the contact area. Subsequently, migration in a new direction is induced. Hence, cell motion is characterized by a concomitant cyclic variation of the contact area[70].

The influence of surface structure and chemistry on this type of cell dynamics in *D. discoideum* cells during adhesion has been investigated quantitatively for different actin manipulating proteins by tracking the cell adhesion area and the protein distribution during the adhesion process[66–69,71]. The analysis of the gain and loss of contact area revealed fluctuations in forces of protrusion and retraction that prevent *D. discoideum* cells from approaching a steady-state of interaction with a substrate. In conclusion, non-monotonic cell spreading is induced by spatio-temporal patterns resulting from the interplay of motor proteins and regulatory proteins, either promoting or terminating the polymerization of actin[66].

The importance of substrate adhesion and interaction was stressed by investigations on the size and number of actin foci in *D. discoideum*, where a negative correlation between the actin foci number and the cell velocity was found[72]. Thus, amoeboid cell motility strongly depends on the interaction with the substrate. This is a very important principle for future studies and potential applications, as similar correlations between focal adhesion dynamics and cell motility have been found for other types of cell migration[73].

2.6 Gene Expression & Cell Differentiation

While each cell nucleus inside the human body contains the exact same DNA, the regulation of the actual expression of these genes is extremely dynamic and individual for every cell. For this purpose, there are global signalling pathways (e.g. controlled by hormone secretion) that provide the baseline for each cell type. In addition, the activation of genes inside a single cell can be heavily influenced by its direct vicinity. As a consequence, every single cell of a certain cell type within a specific biochemical and topographical environment in the human body has its own individual gene expression profile, even though the DNA is the exact same[74].

An abundance of developmental and regenerative processes in the human body is relying on the ability of cells to differentiate into specific subtypes of their original cell type. Cell differentiation is known among most living organisms and does take place during embryogenesis and morphogenesis. In addition, it is of great importance for many reparative and regenerative processes. Cellular differentiation is highly driven by gene expression in reaction to external stimuli – e.g. by other cells, topographic properties of the cell's vicinity and other persistent physiochemical cues that permanently trigger or diminish specific expression pathways[75,76].

Most important for this work is the differentiation of human mesenchymal stem cells (hMSCs), which are a specific type of stem cells that can be found in various tissues inside the human body. They can differentiate into many types of progenitor and mature cells of connective tissue as well as bone, cartilage, muscle, marrow, tendon or ligament tissue (Figure 3).

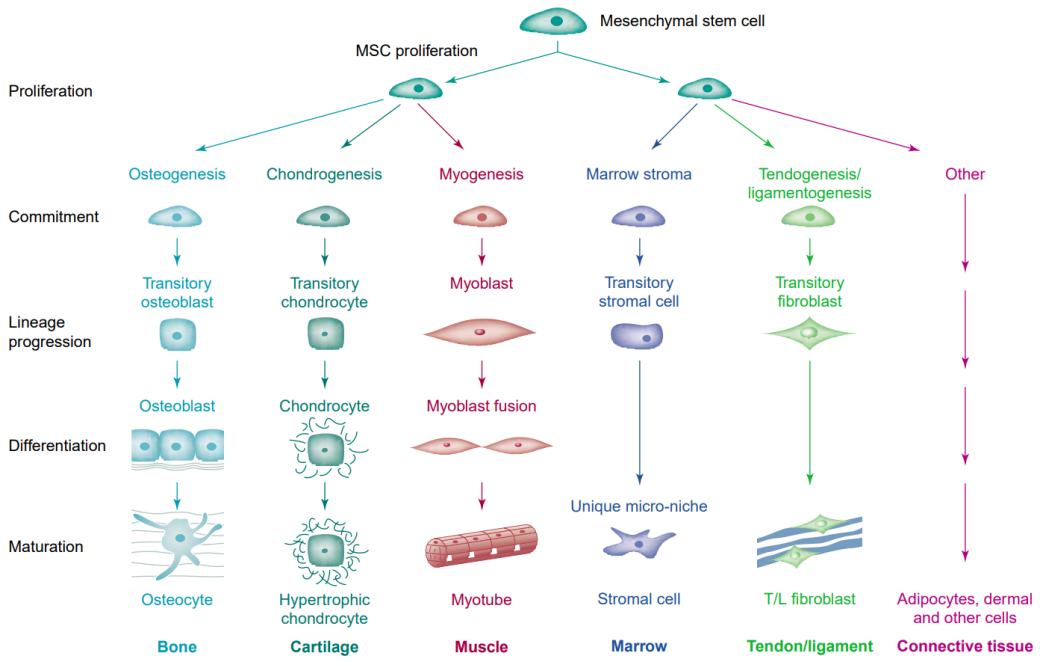

Figure 3: Schematic representation of possilities for MSC differentiation[77]

Due to this regenerative nature and the fact that they can be relatively easy isolated from the bone marrow and expanded in culture, hMCS are a major

research target for regenerative medicine. For example, they could potentially be used for the buildup of *in vitro* tissue models or utilized for implantable devices. For the various differentiation pathways of hMSCs, there are diverse established protocols to trigger the commitment towards specific lineages[78]. As a drawback, these protocols are often very time and cost intensive. Thus, methods for inducing or supporting stem cell differentiation without additional stimuli could be of great benefit for biomedical research.

3. Methodological Background

3.1 Material Preparation

For the different substrates used in cell experiments within this work, different base materials and preparation methods were utilized. As the chemical material synthesis itself was not the focus of this thesis and the author's study program, most steps were performed by collaboration partners. However, the applied methods are explained in brief here to give the reader an insight into the technology.

3.1.1 PDMS Micropillars

In Chapter III of this work, micropillars fabricated by PDMS (Polydimethylsiloxane, Figure 4) molding of masks produced by standard photolithography techniques were utilized. Photolithography is one of the most readily available techniques for the fabrication of micro- and nanostructured materials. Nowadays, standard masks can be ordered from commercial suppliers and highly specialized techniques like soft lithography allow for the creation of masks with surface structures at the nanoscale. These masks can then be used for different polymer molding techniques to produce samples for cell experiments[79]. In recent years, small scale photolithography techniques

were advanced towards the fabrication of biomaterials, e.g. by micromolding, soft lithography or nano imprint lithography[80].

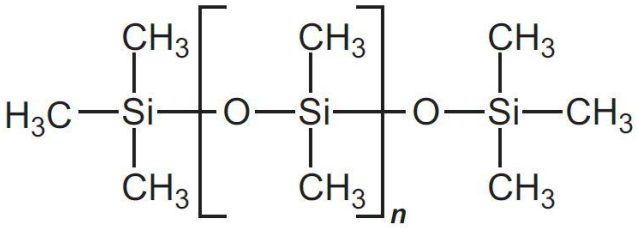

poly(dimethyl)siloxane

Figure 4: Structural formula of PDMS[81].

A stepwise description of the standard clean room photolithography and PDMS molding process used to produce the samples for cell experiments in Chapter III is depicted in Figure 5: (a) A silicon wafer is cleaned in nitrogen flow, (b) spin-coated with a standard negative photoresist, and heated for several minutes (soft-bake). (c) A chromium mask containing the desired structures is aligned over the wafer, followed by UV illumination for several seconds. The lit photoresist is now crosslinked, which is further strengthened by a hard-bake. After that, the unlit, non-crosslinked resist is washed away by several development steps, (d) leaving behind the stable master structure. To improve the unmolding of the PDMS later on, the master can be silanized, e.g. by vapor deposition of a fluorosilane. (e) For sample molding, degassed PDMS master mix, comprised of polydimethylsiloxane and a hardener, is poured onto the silanized master wafer and degassed again. After several hours at 60-70 °C, the PDMS is crosslinked and can be peeled off, (f) yielding a structured PDMS substrate. For use in cell experiments, subsequent Argon plasma treatment is recommended in order to make the surface hydrophilic and thus, ready for cell culture.

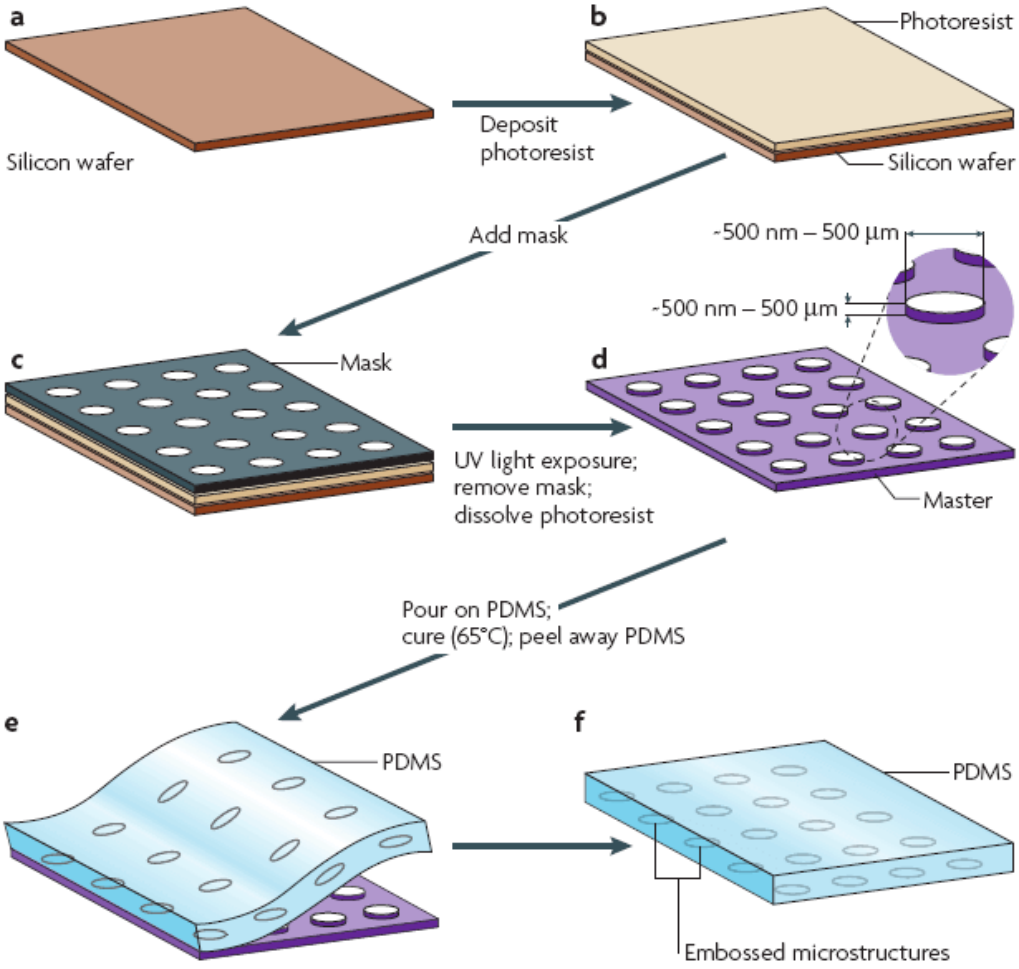

Figure 5: Schematic representation of a standard photolithography process, followed by PDMS molding[82].

3.1.2 Nanostructured Silica Fibers

The sol-gel process is a chemical preparation method for the powderless fabrication of solid materials from colloidal solutions[83]. Different types of end products can be achieved as depicted in Figure 6: Dense films can be deposited as coatings on various substrates via coating processes such as dip-coating or spin-drawing. In addition, uniform (nano)particles, dense ceramics, aerogels and even fibrous materials can be fabricated at much lower temperatures than in usual solid-state processes[84].

In sol-gel process for silica materials, a colloidal solution of inorganic precursors ("sol") is prepared by concurrent hydrolysis and condensation reactions:

Hydrolysis: $Si(OR)_4 + 4\,H_2O \rightarrow Si(OH)_4 + 4\,ROH$

Condensation: $Si(OH)_4 \rightarrow SiO_2 + 2\,H_2O$

Ongoing inorganic polymerization reactions of the species described above give rise to a growing network of siloxane bonds, forming a more viscous "sol". This sol can be further ripened by controlling the evaporation of EtOH, the temperature and the aging time until it is ready for the desired application. In the case of coating processes, further polymerization ("gelation") is triggered by solvent evaporation after the sol film is deposited on the substrate. This can also be supported by additional heat treatment.

Higher volume sols need to be treated in reduced air pressure to form a gel that can be used for further processing[85,86] like fiber spinning: The standard process utilized in this work is consisting of three steps: A mixture of tetraethoxysilane (TEOS), ethanol (EtOH), distilled water (H_2O) and nitric acid (HNO_3) was stirred at room temperature for several hours before removal of EtOH in a rotary evaporator. Then, sol ripening was carried out at low temperature[15]. During this, an abrupt increase of viscosity occurred. The following fiber spinning was performed through nozzle plates of 150 µm nozzle diameter. Fibers were deposited onto an X-Y table that can be used to define various fleece spinning scenarios.

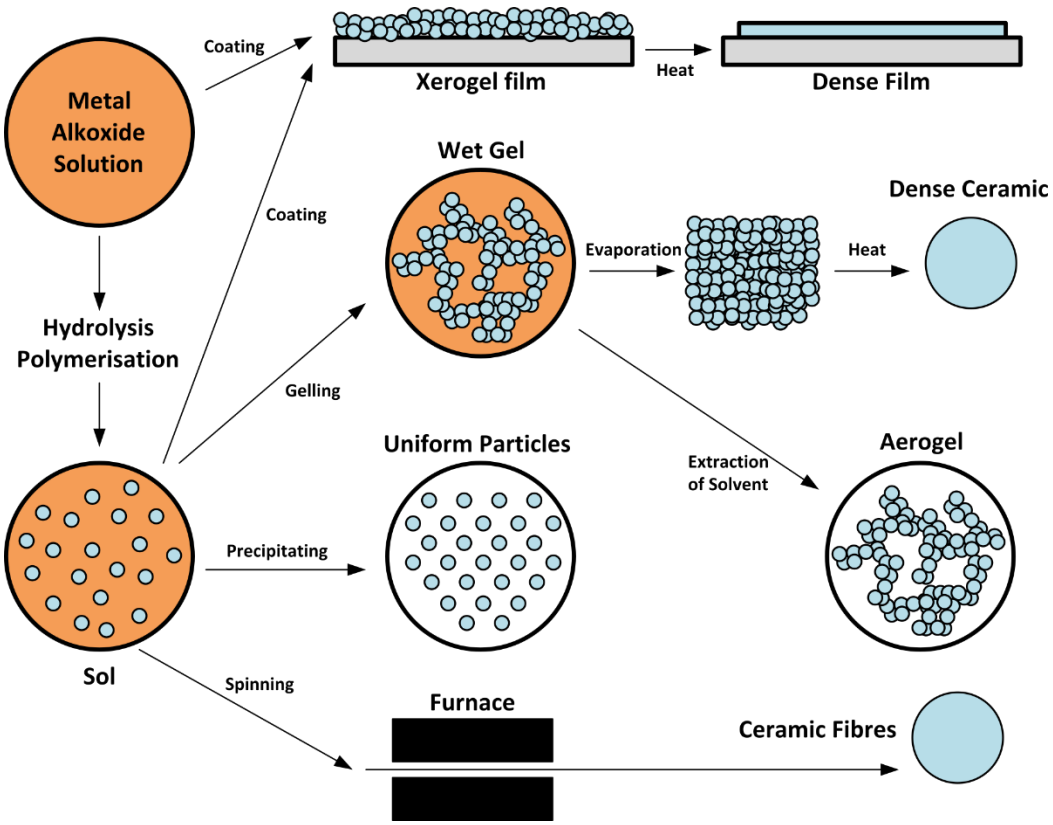

Figure 6: Schematic representation of the sol-gel process with four different end products: Dense Film, Dense Ceramic, Aerogel and Ceramic Fibers[87].

3.1.3 Nanoporous Glass

The ternary glass system $Na_2O - B_2O_3 - SiO_2$ has two miscibility gaps, as visible in the ternary phase diagram (Figure 7), located around an anomaly line A, at which the $B_2O_3 : Na_2O$ ratio is 5.25. Inside these miscibility gaps, there is no stable equilibrium between the three components, causing a separation into at least two distinct phases. These two different phases (SiO_2 and B_2O_3/Na_2O) show different chemical stability and enables acidic dissolution of the B_2O_3/Na_2O phase in order to obtain a stable SiO_2 network. This separation can be initialized and controlled by treatment at elevated temperatures between about 500 °C and 750 °C for several hours: The goal here is to achieve an interconnected, percolated structure of the B_2O_3/Na_2O phase over the whole sample geometry. The heat treatment highly increases mobility inside the glass, enabling the transition from a droplet structure to the characteristic interconnected structure. This is caused by spinodal decomposition processes,

yielding increasing pore sizes for increasing demixing temperatures. As the B_2O_3/Na_2O phase can be leached out in acids or water afterwards, the process yields a SiO_2 framework with interconnected porosity[16,88–90].

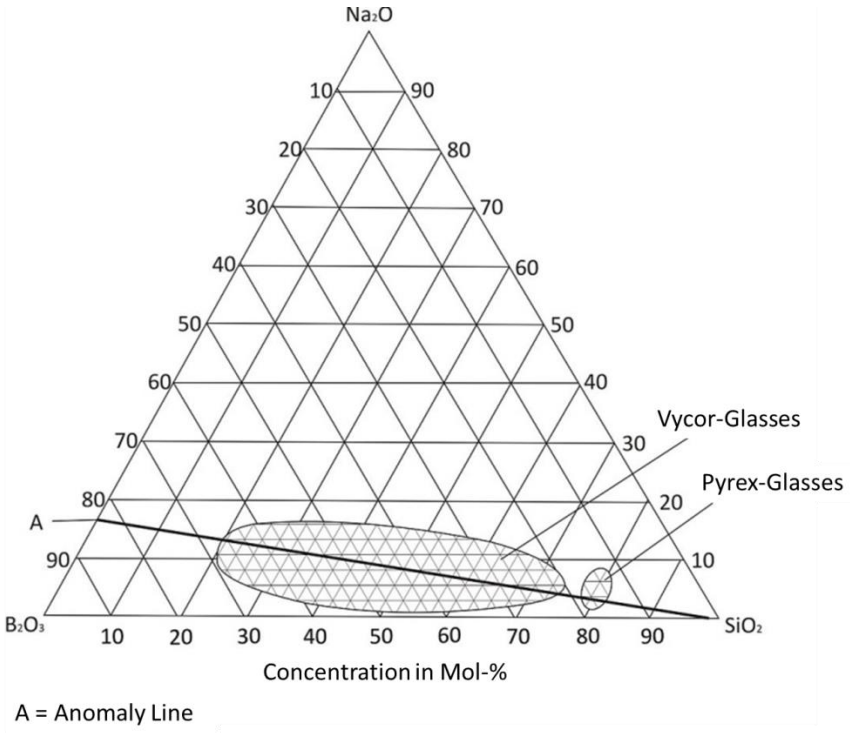

Figure 7: Ternary phase diagram of the glass composition Na_2O – B_2O_3 – SiO_2 (edited from [91]).

In a typical production process for the membrane samples used for experiment in this work, the different components are weighted, dry mixed and melted at ~1500 °C. After slowly cooling down to room temperature, they are cut into small squares and grinded down to 250 µm thickness. These samples were then treated at elevated temperature for 8 h to induce demixing by separation of the phases. In order to achieve the final porous network, the samples were then leached in distilled water at temperatures around 90 °C.

3.2 Material Characterization

3.2.1 UV-VIS Transmission Spectroscopy

UV-VIS spectroscopy is an analytical procedure that gives insights into the molecular composition of fluid samples and the intrinsic structure of fine powders, thin films or thin, porous materials. This spectroscopy method is generally based on different effects caused by the interaction of electromagnetic radiation with matter, like reflection, transmission, scattering or adsorption. A typical double-beam setup is given in Figure 8: UV-VIS spectroscopy utilizes a light source with wavelengths between 180 nm and 1100 nm and a monochromator allowing for measurements at defined wavelengths within this spectrum. For a user-specified spectrum and stepsize, the transmission of light is measured for the sample solution and a reference solution containing pure solvent. The photodetectors then measure the transmission through the material and correlate the sample to the reference signal. The results can then be compared with reference curves of solutions with different concentrations of the target molecule.

The classical use case of UV-VIS spectroscopy in chemistry is the detection of the presence of a certain molecule in a solution. Most organic molecules have an even number of electrons with a big energy gap between the molecular orbitals. Radiation in the UV-VIS spectrum can excite electrons from the HOMO (highest occupied molecular orbital) to the LUMO (lowest unoccupied molecular orbital). The characteristic absorption wavelengths of specific molecules are then observed as reduction in the transmission at this part of the spectrum.

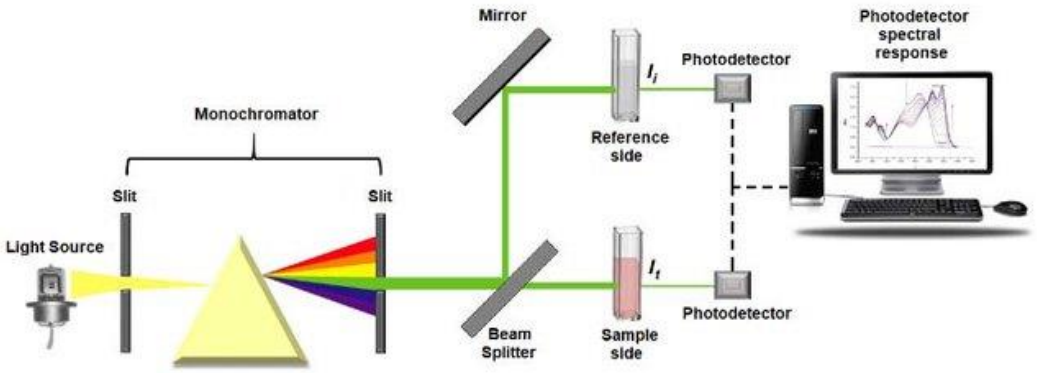

Figure 8: Schematic representation of a double beam setup for UV/VIS spectroscopy[92].

For the nanoporous glass samples measured in this work, the main phenomenon for reduced transmission is scattering. As describe in the previous chapter, the samples are comprised of a nanoporous SiO_2 matrix. Thus, there are two different materials with different refractive index: the SiO_2 matrix and the pores. The opaqueness observed for samples produced at various demixing temperatures (Figure 26) can be explained by that: With increasing demixing temperatures, the nanopore sizes are increasing, scattering a more and more broad spectrum of the visible light on the passage through the sample. The pores are the scatterer inside the material and transmitted light is undergoing repeated scattering processes, most presumably Mie-Scattering which is applicable for particles (pores) larger than one tenth of the wavelength.

3.2.2 Scanning Electron Microscopy (SEM)

Scanning electron microscopy (SEM) is an analytical method to investigate the surface and near-surface region of materials down to the nanoscale. After proper sample preparation, even biological samples can be investigated if they are stable in the evacuated observation chamber. Usually, sample preparation also includes sputtering a thin gold or platinum layer to the surface in order to ensure conductivity and prevent electric charging of the sample.

During measurements, the sample surface is scanned with a focused electron beam, whose electrons interact with the material's surface atoms. When the electron comes in contact with the surface atoms, several elastic and inelastic scattering processes occur that can be observed with different detectors. For every pixel, the microscope software translates the intensities of the detector signals into different greyscales of image information, giving a representation of the measured surface topography.

Elastic and inelastic scattering of the high-energy electrons produces different signals which can be collected by different detectors, namely SE (secondary electron) and BSE (backscattered electron) scanners. The obtained pixel information from the detector is than translated into an image, giving the specimen's surface topography.

3.3 Cell Migration Analysis

3.3.1 Fluorescencent Cell Labelling

All studies in parts III, IV and V of this work are using fluorescent cell labelling for visualization and tracking of cells. Fluorescence is a specific form of photoluminescence: It describes the spontaneous emission of light after excitation by light of a higher energy than the emission wavelength (Figure 9). After absorption of a photon of a certain wavelength, an electron of a fluorophore is raised to an excited state (S2). Fluorophores are typically organic molecules with several aromatic groups or other molecules with multiple π bonds[93]. In a series of multiple, non-radiative internal conversion and vibrational relaxation steps, the electron relaxes back to the lowest excitation state (S1). After that, it relaxes back to the ground state (S0), accompanied by emission of a photon of a certain wavelength that is lower than the excitation wavelength.

Modern techniques for the genetic modification of cells and the targeted expression of specific proteins open up wide possibilities for the observation of cellular and intracellular processes[94]. Vectors for expression of fluorescent proteins, e.g. the Green Fluorescent Protein (GFP)[95], can be incorporated into the genome of eukaryotic cells. As this growing availability of genetic manipulation techniques is accompanied by more and more sophisticated high-resolution microscopy and an ever growing knowledge of the specific genomes of certain organisms and cells and the function of the proteins inside of cells, there is practically no limit to innovations in the observation of specific processes[96].

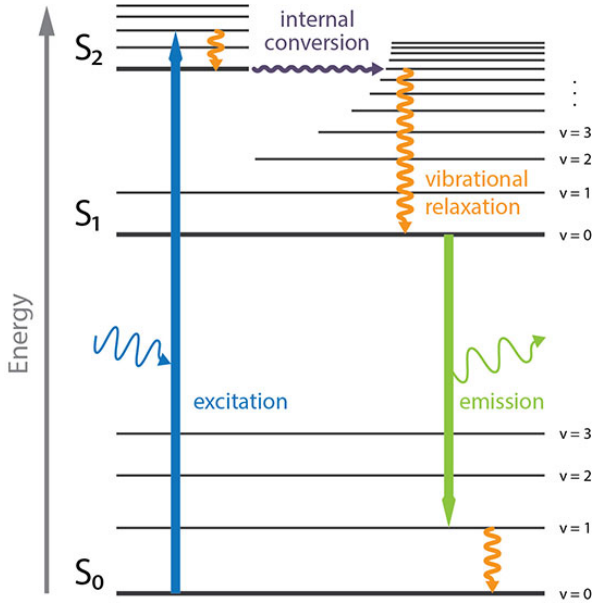

Figure 9: Simplified version of a Jablonski Diagram for Fluorescence[97].

3.3.2 Time-Lapse Fluorescence Microscopy

For cell migration experiments within this work, time-lapse fluorescence microscopy of living cells is an essential measurement technique. A typical buildup of a fluorescence microscope is given in Figure 10: Illumination is provided by a high energy light source and filtered to specific wavelengths by fluorescence excitation filters. A dichroic mirror then focuses the light onto the observation area, thus limiting the exposure and potential radiation damage to

other parts of the sample. The induced fluorescence inside the cells passes through an emission filter and is led to the eyepieces and a CCD camera equipped with a photomultiplier. This specific technique allows for the reduction of excitation intensity and consequential preservation of cell vitality for long-term experiments. For a typical migration experiment, an image of multiple observation areas of the sample is taken every 7 seconds for a duration of 45 minutes.

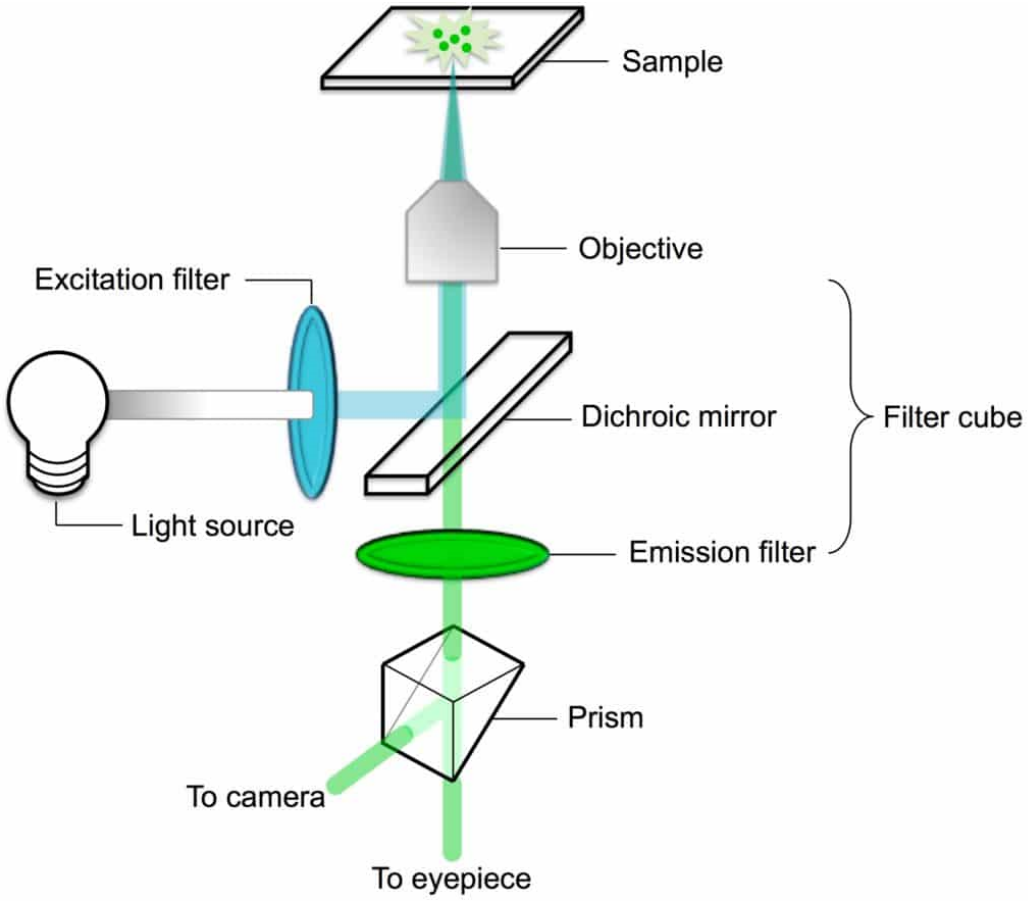

Figure 10: Basic principle of inverted fluorescence microscopy[98].

3.3.3 Mean-Squared Displacement Analysis

Mean squared displacement (MSD) analysis has its origins in statistical physics where it is used to calculate the spatial range of random motion processes. Generally speaking, the mean squared displacement is the area that is explored by a randomly moving object. The advantage of MSD analysis is that it can

utilize an adaptable diffusion coefficient for more realistic outputs and simulations of different environment scenarios[99]. For the studies carried out in this work, a refined local MSD analysis is applied for the analysis of cell migration trajectories obtained from fluorescence microscopy. As this is a central part of this work, the method is laid out in detail in the materials & methods chapters of part III and IV of this work.

III. Cell Migration Inside Controlled Microtopographies

This chapter was published as

"Amoeboid migration mode adaption in quasi-3D spatial density gradients of varying lattice geometry"

by Max Gorelashvili, Martin Emmert, Kai Friedrich Hodeck and Doris Heinrich

in New Journal of Physics, Volume 16, July 2014.

Julius-Maximilians-
UNIVERSITÄT
WÜRZBURG

Fakultät für
CHEMIE UND
PHARMAZIE

Erklärung zur Autor:innenschaft

Amoeboid migration mode adaption in quasi-3D spatial density gradients of varying lattice geometry
Max Gorelashvili*, Martin Emmert*, Kai Friedrich Hodeck and Doris Heinrich -- New Journal of Physics, Volume 16, 2014, 075012 (* = Hauptautor:innen)

Detaillierte Darstellung der Anteile an der Veröffentlichung (in %)
Angabe Autor:innen (ggf. Haupt- / Ko- / korrespondierende/r Autor:in) mit Vorname Nachname (Initialen)

Max Gorelashvili (mg), Martin Emmert (me), Kai Friedrich Hodeck (kfh), Doris Heinrich (dh)

Autor:in	**mg**	**me**	**kfh**	**dh**	**A5**	**A6**	**A7**	**A8**	**A9**	**A10**	**A11**	**∑ in Prozent**
Zellexperimente (Zellkultur, Probenvorbereitung, Mikroskopie)	5%	90%		5%								100%
Post-Processing der Migrationsdaten (Bildbearbeitung, Thresholding, Generierung der X-Y Migrationstracks)	5%	95%										100%
Auswertung der Migration & Interpretation	40%	40%		20%								100%
Verfassen der Veröffentlichung	35%	35%	20%	10%								100%
Korrektur der Veröffentlichung	20%	20%	20%	40%								100%
Koordination der Veröffentlichung	25%	25%	0%	50%								100%
Summe	21,7%	50,8%	6,7%	20,8%								100%

1. Abstract

Cell migration processes are controlled by sensitive interaction with external cues such as topographic structures of the cell's environment. Here, we present systematically controlled assays to investigate the specific effects of spatial density and local geometry of topographic structure on amoeboid migration of *Dictyostelium discoideum* cells. This is realized by well-controlled fabrication of quasi-3D pillar fields exhibiting a systematic variation of inter-pillar distance and pillar lattice geometry. By time-resolved local mean-squared displacement analysis of amoeboid migration, we can extract motility parameters in order to elucidate the details of amoeboid migration mechanisms and consolidate them in a two-state contact-controlled motility model, distinguishing directed and random phases. Specifically, we find that directed pillar-to-pillar runs are found preferably in high pillar density regions, and cells in directed motion states sense pillars as attractive topographic stimuli. In contrast, cell motion in random probing states is inhibited by high pillar density, where pillars act as obstacles for cell motion. In a gradient spatial density, these mechanisms lead to topographic guidance of cells, with a general trend towards a regime of inter-pillar spacing close to the cell diameter. In locally anisotropic pillar environments, cell migration is often found to be damped due to competing attraction by different pillars in close proximity and due to lack of other potential stimuli in the vicinity of the cell. Further, we demonstrate topographic cell guidance reflecting the lattice geometry of the quasi-3D environment by distinct preferences in migration direction. Our findings allow to specifically control amoeboid cell migration by purely topographic effects and thus, to induce active cell guidance. These tools hold prospects for medical applications like improved wound treatment, or invasion assays for immune cells.

2. Introduction

Amoeboid motion is a particularly efficient form of cell migration, characteristic for several cell types, e.g. stem cells, specific immune cells or metastatic tumor cells. In the human body, these cell types exhibit rapid migration through diverse types of tissue, enabling them to travel long distances to their point of destination[100].

The high efficiency of amoeboid migration is the result of interplay of fast cytoskeletal dynamics and relatively weak, short-lived contacts to the substrate.[18,38,61,101–104] These mechanisms allow for a rapid response to chemical and mechanical cues in the cells' environment.[105] For example, amoeboid migration is observed for neutrophils and leukocytes, migrating towards the source of an inflammation in response to molecular signaling cascades.[68] Interestingly, similar signaling cascades and corresponding response mechanisms can be observed in *Dictyostelium discoideum* (Dd) amoebae.[106] Thus, Dd is both a biologically relevant and experimentally robust model organism to study amoeboid cell migration as a response to environmental cues.[107]

Influence on cell migration can be generated by several types of external cues like chemical signals[20,108–112] and mechanical stimuli.[113–115] Topographic variations in the vicinity of migrating cells are a special type of mechanical stimulus, but their importance becomes clear by looking at human tissue: cells are always facing local variations in their natural environment, as the local topography inside tissue of the human body is far from being isotropic. In fact, tissue is the antipode of the flat and smooth glass substrates commonly used in 2D in vitro migration assays. Recent progress in technologies for controlled fabrication of micro- and nano-structures facilitated the investigation of cell behavior in response to topographic variations like grooves or pillars. However, extensive studies on cell orientation[116,116] and migration[64,117] led to sometimes contradictory findings, even for the same substrate structures and

cell types.[118,119] In this context, it is crucial to establish model experimental situations to control and measure the effects of topographic stimuli on migrating cells precisely and reproducibly. By that, more detailed numerical analyses enable reliable interpretations and predictions with respect to realistic 3D conditions inside the human body.

Following this approach, we designed systematically controlled assays to assess the influence of topographic cues on cell migration behavior. In particular, we used PDMS micro-pillar fields consisting of lattices of trigonal (isotropic) and hexagonal/honeycomb (anisotropic) geometry with defined density gradients, providing spatially controlled quasi-3D environments for cell migration. In doing so, we take advantage of the fact that PDMS is a comprehensively characterized standard material, which provides a well-controllable model environment for systematic cell migration studies.[13,60] To exclude surface-induced or chemically related side-effects, the pillar samples were produced from bulk material, exhibiting uniform surface structure and chemical composition. This way, we make sure that the pillars and the bottom in between them are of the same material. For all experiments the pillars are non-flexible posts of the same diameter $d = 4\,\mu m$. This way, changes in the migration behavior of cells in contact with the pillar structures can be related solely to the topographic properties of the environment. By performing local mean squared displacement (l-MSD) analysis of cell trajectories within the pillar fields we extract cell motility parameters from phases of directed runs (dir-runs) and random motion modes (rm-modes) of amoeboid migration. This allows us to analyze changes in cell migration behavior with respect to local variations in pillar density and pillar lattice structure. First, we study the effect of the spatial pillar density on Dd single cells migrating in quasi-3D micro-pillar fields of varying pillar densities. As a second part of this work, we investigate the influence of the local geometry on cell migration by comparison of Dd migration in trigonal (isotropic) and hexagonal (anisotropic) pillar fields.

Finally, we examine topography-induced cell guidance effects in dependence on pillar density gradients and lattice geometry.

With this study, we aim at revealing the mechanisms governing amoeboid cell migration by structural cues in a quasi-3D environment. A detailed understanding of these mechanisms will allow for topographic control of amoeboid cell migration, holding prospects for future applications, e.g. for the design of invasion assays for immune cells and smart materials for wound treatment.

3. Materials and methods

Amoeboid migration of single *D. discoideum* (Dd) cells in the vegetative state was studied. The experiments were performed at low cell density in the absence of cell nutrients, in order to avoid external chemical stimuli biasing cell migration. We observed Dd cells in quasi-3D environments, provided by hexagonal arrays of micro-pillars, fabricated from transparent polydimethylsiloxane (PDMS). For systematic study of cell migration in response to topographic cues, we varied the inter-pillar distance and the geometry of the pillar arrays in a controlled manner. PDMS as a material is stiff (elastic modulus $E = 1.72\ MPa$)[12] with respect to the relatively weak adhesion forces exhibited by Dd cells.[120,121] This allows for the investigation of structural determinants of amoeboid cell migration independent of the details of the particular cell–substrate interaction. Fluorescently labeled Dd cells and transparent PDMS pillar arrays were imaged by fluorescence and bright-field microscopy. Cell migration analysis was performed by using an established cell tracking routine[122] and l-MSD analysis software.[123]

3.1 Cell culture and microscopy imaging

3.1.1 Cell culture

The axenic Dd strain (HG1694) expressing freeGFP (obtained from Dr Günther Gerisch, MPI for Biochemistry, Martinsried, Germany) was grown in HL5 medium (ForMedium™, Hunstanton, UK) adjusted at $pH = 6.7$ and complemented by the antibiotic Gentamycin at a concentration of 20 $\frac{\mu g}{mL}$ (G-418, Biochrom AG, Berlin, Germany). The cell confluence was kept below 40 %.

For microscopy experiments, HL5 medium was substituted by phosphate buffered saline (PBS), adjusted at $pH = 6.0$. The cell–PBS suspension was filled into the observation chamber (composed of a cover glass and a Teflon® frame) and rested for 20 min to let the cells settle down, until a concentration of 10-20 cells per $400 \times 400\ \mu m^2$ (camera field of view) was achieved.

3.1.2 Microscopy

The measurements were carried out with a 20× objective (Nikon, Germany) on a Nikon Eclipse Ti microscope (Nikon, Germany) equipped with an EM-CCD camera (Hamamatsu, Herrsching, Germany) at 19–21 °C. Fluorescence and bright field images of fluorescently labeled cells and transparent pillar arrays were acquired every 10 s for at least one hour to exclude short-time effects. To minimize the excitation stress for the cells, exposure times were kept below 100 ms.

3.2 Preparation of micron-sized PDMS pillar structures

Substrates on which cells were seeded were made out of the transparent polymer polydimethylsiloxane (PDMS), after its casting, cross-linking and unpeeling from a silicon wafer-based master obtained by standard

photolithography procedures. The PDMS structures resulting from this process were two different types of arrays of 10 –12 µm high pillars with a constant diameter of 4 µm.

Experimental characterization by scanning electron microscopy shows that the pillars are in fact highly uniform, with variations in dimension on nanometer scale, due to the precisely controlled fabrication process of the samples (Figure 15). The PDMS micro-pillar array fabrication was done by the standard procedure previously described by Steinberg *et al.*[13] The well-defined character, i.e. constant diameter, of the PDMS micro-pillars used for our cell migration experiments has already been demonstrated by Arcizet *et al.*[60] Accordingly, variations in stiffness of the pillars influencing the cell interaction can be excluded for the experiments.

Pillars were arranged in (i) arrays of trigonal geometry with gradients in lattice constant, ranging from 8.2 µm to 22.5 µm, or in (ii) lattices of hexagons with gradients in hexagon side length ranging from 10.5 µm to 38.4 µm. Please note that all substrates, including the micro-pillars and the areas in between, exhibit the same chemical composition. This way any external chemical bias of cell migration can be excluded.

3.2.1 Master fabrication

Master fabrication was performed by standard clean room microlithography procedures, according to protocols described by Steinberg *et al.*[13] Therefore, a 3 inch silicon wafer (Si-Mat, Landsberg/Lech, Germany) was cleaned under nitrogen flow protection and covered with 5 ml of SU8-10 negative photoresist (Microchem, distributed by Micro Resist Technology, Berlin, Germany) by spin-coating at 3000 rpm for 30 s. After that, the substrate was progressively soft-baked (1 min at 65 °C and 2 min at 85–90 °C, cooling down slowly to room temperature) and illuminated with UV-light in a mask aligner (Süss MicroTec, Garching, Germany) through a chromium mask (ML&C, Jena, Germany), with

varying illumination times of 3–5 s, according to the intended structure sizes. The illumination was followed by a progressive hard bake of 1 min at 65 °C, and 2 min at 85–90 °C, with cooling down slowly to room temperature. After that, the unilluminated photoresist was removed by two bathing steps in SU8-specific developer (MicroResist Technology, Berlin, Germany).

3.2.2 Preparation of the PDMS structures

The resist master was silanized by vapor deposition of fluorosilane (1H,1H,2H,2H-perfluorooctyltrichlorosilane, ABCR, Germany) under vacuum for one hour. The PDMS base and the cross-linking agent were mixed at a 1:10 ratio (Sylgard 184 Silicone Elastomer Kit, Dow Corning, MI, USA) and degassed for 30 min under vacuum. Subsequently 2–3 ml of PDMS was poured on the Si-photoresist master, and degassed again for 15–30 min under vacuum. PDMS cross-linking was obtained after 3–5 h at 65 °C. After cutting and peeling the PDMS structures off the master, the samples were immediately transferred to the observation chambers (consisting of a cover glass and a Teflon® frame), immersed in PBS solution and stored until use for cell migration experiments.

3.3 Cell migration analysis

Cell migration analysis was performed in two steps. First, center of mass positions (X and Y coordinates) of each cell, investigated at each time point of the experiment, were obtained from fluorescence images using a cell tracking plug-in[122] for ImageJ image analysis software (W. S. Rasband, US National Institutes of Health, Bethesda, USA, http://imagej.nih.gov/ij/). This plug-in detects cells as clusters of more than n bright pixels of a certain set intensity I in closer proximity than a distance d. All of these parameters were adjusted optimally for precise cell recognition.

In a second step, the obtained cell position data were processed using a homemade Matlab algorithm. This algorithm was adapted from the previously

developed TRAnSpORT routine[60,123] and is able to distinguish two modes of cell migration—directed runs and random motion phases—in a time-resolved manner. For this purpose, TRAnSpORT routine uses global as well as l-MSD analysis of cell trajectories.

Instantaneous migration velocity and direction are obtained from the changing positions of the center of mass of the cell. A global trend towards a migration state of a more 'diffusive' or a more 'directed' character is determined by global MSD (MSD) analysis over the entire trajectory of each cell.

The l-MSD analysis is based on a two-state model of cell migration, extracting alternate phases of directed runs and diffusive-like random walks.[60,61] The directed parts of the trajectory correspond to phases when the amoeba crawls at a quasi-constant speed in a quasi-constant direction. The directed runs are separated by non-directed phases, during which the cell probes its environment, repolarizes and starts a new directed run in another direction. As a key feature, the l-MSD analysis algorithm is capable of distinguishing the two motility modes in the migration trajectories. After trajectory splitting, the phase durations can be retrieved, together with specific migration parameters, such as velocity for the directed runs, and a diffusion coefficient analogue for the random motion states. The power of this method lies within the fact that the parameters are evaluated only during the corresponding phases of the motion. This prevents, for example, phases of directed motion from biasing the overall statistical analysis by increasing the global diffusion coefficient analogue. Moreover, the local analysis reveals otherwise hidden features of the migration behavior, which are related to local or short-term stimuli.

l-MSD $\Delta R_i^2(\tau_k)$ and angle persistence $\Delta\varphi_i(t_i,\ \tau_k)$ are calculated over a rolling window of $M = 30$ frames for each experiment time point t_i of the trajectory as a function of different lag times $\tau_k = k \cdot \delta t$ as follows:

$$\Delta R^2(t_i,\tau_k) = \Delta R_i^2(\tau_k) = \frac{1}{M-k+1}\sum_{j=-\frac{M}{2}}^{\frac{M}{2}-k} (R(t_{i+j}+\tau_k) - R(t_{i+j}))^2 \qquad (1)$$

$$\Delta\varphi(t_i,\tau_k) = \Delta\varphi_i(\tau_k) = \sqrt{\frac{1}{M-k+1}\sum_{j=-\frac{M}{2}}^{\frac{M}{2}-k} (\varphi(t_{i+j}+\tau_k) - \varphi(t_{i+j}))^2} \qquad (2)$$

Here, $R(t_i) = (X(t_i), Y(t_i))$ is the coordinate of the center of mass of the cell and $\delta t = 10$ s is the inverse frame rate of the experiment. In previous work, the l-MSD analysis algorithm was tested with the precisely controlled motion of latex beads in microfluidic stop-flow experiments.[123] Based on this calibration, the window size is adapted for application to biophysical questions. In this context, we showed that the temporal resolution obtained by the l-MSD analysis is of the order $\frac{M\cdot\delta t}{4}$s .[123] Specifically for cell migration in PDMS pillar fields we determined $M = 30$ frames per time point as suitable window size,[60] which is chosen accordingly for the comparable experimental setting in this work. The l-MSD function is fitted by using a well-established relation from statistical physics:

$$\Delta R^2(t_i,\tau_k) = A\cdot\tau_k^{\alpha}$$

Here, the exponent α characterizes the migration state of the cell and the prefactor A bears either the information about the diffusion coefficient analogue of random diffusive-like migration modes or the velocity of directed runs. For $\alpha \approx 2$ and a persistent angle of motion, the cell migration state is defined as 'directed', otherwise as 'random' migration mode. The l-MSD algorithm defines the probability for directed motion for a certain time point as

$$P_{dir} = \begin{cases} 1 & \text{for } [1.7 \le \alpha \le 2\,] \wedge [\,0 \le \Delta\varphi \le 0.9 \text{ rad}\,] \\ 0 & \text{otherwise} \end{cases}$$

Further, phase durations τ^{rm} and τ^{dir} for random states and dir-runs are computed, as well as the overall probability P^{rm} and P^{dir} for each migration mode.

4. Results and discussion

In this work, we study the influence of structural properties of the local environment on amoeboid migration of Dd cells in the vegetative state, in the absence of any chemical attractors. Specifically, we investigate the influence of spatial density and geometry of the environment, independently of the details of the particular substrate adhesion mechanism of the cells. Therefore, we analyze amoeboid cell migration within well-defined micro-pillar arrays of gradient inter-pillar distance and different lattice geometry. Standard pillars of 4 μm diameter and 10–12 μm height are made of polydimethylsiloxane (PDMS) by standard photolithography and polymer molding procedures. To avoid chemically related side effects, the entire substrate was fabricated from bulk material exhibiting homogeneous chemical composition and surface properties. Please note that within the pillar arrays, the cells migrate in a quasi-3D environment, i.e. on the bottom substrate in between the pillars, not on top of pillars. Migration of fluorescently labeled Dd cells in transparent PDMS pillar arrays is imaged by fluorescent and bright field microscopy.

We analyze first the migration of cells in fields of trigonal lattice structure and different pillar density. For our investigations, we measured cells in pillar arrays of gradient inter-pillar distance ranging from values close to half the average cell size (diameter) up to twice the cell size. Accordingly, we differentiate between three regions of spatial density of the pillar fields: (i) low density regions, where cells contact only one to two pillars simultaneously, (ii) intermediate density regions, where cells sense three to five pillars in their immediate vicinity and (iii) high density regions, where the cells are squeezed in between more than five neighboring pillars. Secondly, we study the effect of

geometry by comparison between cell migration in isotropic trigonal (T-arrays) (Figure 12 A–C) and in anisotropic hexagonal lattices (H-arrays) of gradient inter-pillar distance. Hexagonal arrays are congruent with trigonal lattices, where the pillar in the center of each hexagon is missing (Figure 13 A-C). Thus, H-arrays lack the local topographic isotropy exhibited by T-arrays. Further, hexagonal lattices provide more space for cell migration on the 'floor' (base substrate) in between pillars compared to trigonal pillar arrays. Thirdly, we analyze guidance of cells by topographic cues, specifically with respect to the direction of the pillar density gradient and the respective lattice vectors of the pillar arrays.

For data evaluation, center of mass trajectories of cells within pillar arrays were extracted from the obtained image stacks. A typical cell trajectory in a trigonal pillar array for a time period of 68 min is shown in Figure 11 A. The obtained data were analyzed with respect to cell migration.[60,61] MSD lag-time dependent analysis of the whole cell trajectory bears information on global migration properties of different time-scales, as illustrated by Figure 11 B. Here, a distinct decrease in the exponent α for increasing lag-times is shown. To resolve the migration state of the cell at each experiment time point, we perform l-MSD analysis within a predefined time window (of length $M = 30$ frames), sliding along the entire cell trajectory. By that, each cell trajectory is divided into phases of directed runs (dir-runs) and random motion (rm-mode), as shown in Figure 11 C. This analysis is based on the lag-time dependent l-MSD function as shown in Figure 11 D, which bears the full information of all states for each time point. During directed runs (dir-runs), a cell migrates at nearly constant velocity and exhibits a high directional persistence. In random migration phases, cells probe their environment in a diffusive-like manner without any preferred migration direction. The migration state is identified as dir-run by criterion of the l-MSD exponent $\alpha \approx 2$ and angular persistence $\Delta\varphi \approx 0$, or is assigned the rm-mode in all other cases. The numerical analysis of the cell motility states yields distributions for the l-MSD exponent α, for

instantaneous velocities v^{rm} and v^{dir} and for phase durations $\tau^{rm}$and τ^{dir}, as well as the overall probabilities P^{rm} and P^{dir} to be in the rm-state or to perform a dir-run, which are discussed at first by evaluation of their mean values. Further, the numerical distributions of the cell migration parameters were statistically characterized by their median values and the measures for deviation and relative asymmetry, as listed in Table 2. We find that in all pillar arrays, cell migration can be well characterized by the two-state motility model and cells exhibit dir-runs as well as rm-modes.

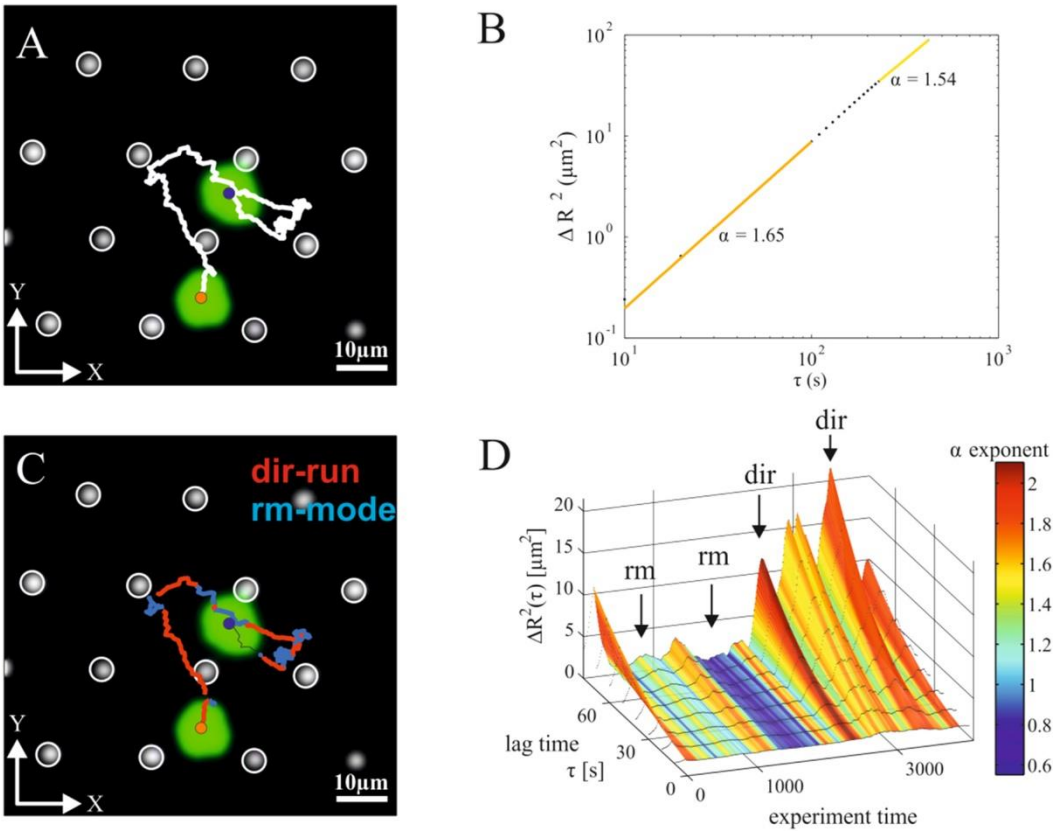

Figure 11: Two-state amoeboid motility model. (A) Typical trajectory (white curve) of a *D. discoideum* amoeba cell (green) migrating in a quasi-3D trigonal pillar lattice (white pillar tops). White circles highlight positions of the pillars, which are of uniform shape and constant diameter of 4 *µ*m. The cell is shown for time points t_1 = 0 min and t_2 = 68.2 min, with corresponding positions of its center of mass in blue (t_1) and orange (t_2). (B) Global mean squared (MSD) analysis of the cell trajectory in (A), revealing different motility state trends, by change of slope as a function of the lag-time *τ*. (C) Cell trajectory of (A) split into directed runs (dir-run) of almost constant velocity and high directional persistence (red), and random migration phases (rm-mode) (blue), using local MSD analysis. (D) Landscape-plot of the local MSD function, bearing information of lag-time dependent motility states for each time point of the experiment. The local MSD exponents, which quantitatively describe the motility state, are color-coded, whereby dir-runs are shown in red and rm-modes in yellow to blue, depending on the value of the exponent.

4.1 Cell migration in isotropic trigonal pillar arrays of varying lattice constant

To study the influence of pillar density on cell motion, we analyze cell migration ($N = 126$ cells, $n = 44\ 200$ data points) within micro-pillar arrays of regular trigonal lattice structure exhibiting a density gradient. With respect to the mean cell size, we define three regimes of the pillar lattice constant a as $a > 16$ µm (region T1), $16\ \mu m > a > 13\ \mu m$ (region T2) and $13\ \mu m > a$ (region T3), representing low, intermediate and high pillar density, respectively. In comparison, the typical cell size (diameter) of Dd amoeba is ~ 8–12 µm. Figure 12 A–C show representative images of cells in pillar fields of trigonal lattice geometry at low (T1), intermediate (T2) and high density (T3). Please note that Figure 12 A–C shows genuine microscopy images which have been optimized for acquisition of the fluorescent cells' positions in the quasi-3D environments of not fluorescently labeled pillar fields. This explains the slightly different image appearance of the pillars, which are in fact highly uniform, with a diameter of 4 µm and extremely small variation in dimension (Figure 15). For Dd cells the pillars act as uniform, non-flexible posts they encounter in their migration paths.

In the low density regime (T1), cells can attach to one or two pillars at the same time (Figure 12 A), but are able to sense more neighboring pillars by filopodia. In the intermediate regime (T2), cells can establish contacts with three to five pillars simultaneously (Figure 12 B). For a high pillar density, cells are squeezed in between more than five pillars (Figure 12 C).

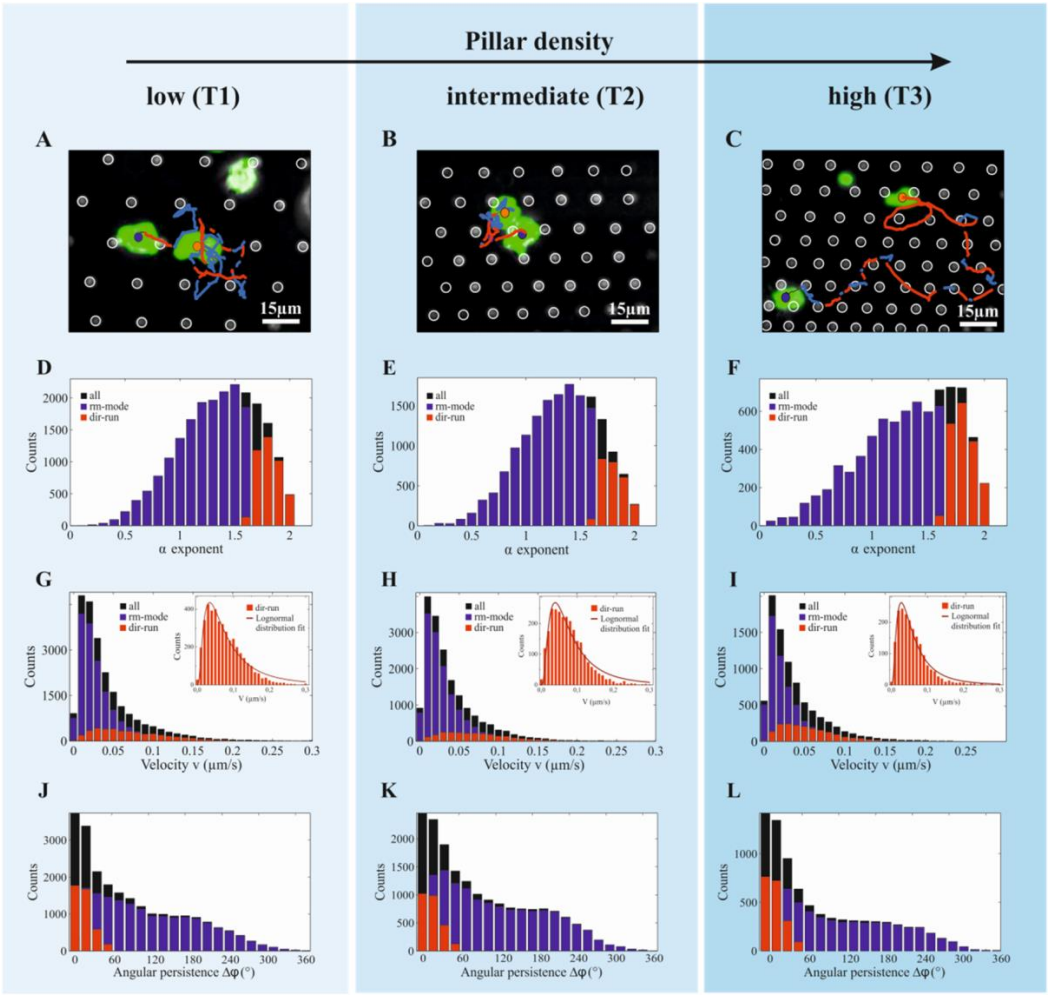

Figure 12: Cell migration in trigonal lattices of varying pillar density regimes. Cell motility state characteristics for cells migrating in isotropic trigonal pillar lattices of low (T1), intermediate (T2) and high density (T3). (A), (B), (C) Typical trajectories of *D. discoideum* cells (green), with phases of directed runs (red) and random migration modes (blue). Cells are shown for time points t_1 = 0 min and t_2 = 50 min (A), t_2 = 53 min (B) and t_2 = 90 min (C), respectively. The corresponding cell center of mass positions are highlighted in blue (t 1) and orange (t_2). White circles highlight positions of the pillars, which are of uniform shape and constant diameter of 4 µm. (D), (E), (F) Distributions of alpha exponents of dir-runs (red), rm-modes (blue) and all values (black) describing the characteristics of cell motion in the different pillar density regimes. (G), (H), (I) Corresponding distributions of instantaneous velocities during dir-runs (red) and rm-modes (blue). The overall distributions of instantaneous velocities are shown in black. Insets show velocity distributions of dir-runs, fitted by log-normal distribution function. (J), (K), (L) Angular persistence of cell migration during directed runs (red) and random migration modes (blue). The overall distribution is shown in black.

4.1.1 High pillar density facilitates dir-runs

Local-MSD analysis of cell motility states (i.e. directed runs and random migration modes) in different density regimes of the trigonal pillar lattices reveals a distinct dependence of amoeboid cell migration on spatial density. The probability for dir-runs shows the highest value at high pillar density

($P_{T3}^{dir} = 25.1\,\%$), followed by the low density regime ($P_{T1}^{dir} = 20.4\,\%$), while it is significantly lower at intermediate pillar density ($P_{T2}^{dir} = 16{,}2\,\%$), for reference: on flat PDMS substrate $P_{2D}^{dir} = 35\,\%$) (Table 1). In addition, the values of angular persistence $\Delta\varphi$ are slightly higher for high and low density regimes than for intermediate spatial density of T-arrays (Figure 12 J–L and Table 1). The mean value of the l-MSD exponent $\langle\alpha_T^{dir}\rangle$ of the dir-run states is nearly equal for all density regimes of trigonal pillar arrays and for 2D substrates (Figure 12 D–F, Table 1). These results reveal that dir-runs are more pronounced in high and low density regions of the trigonal arrays, as compared to intermediate density areas.

Table 1: Parameters describing cell motility in pillar lattices of trigonal (T1, T2, T3) and hexagonal (H1, H2, H3) lattice geometry and different inter-pillar distances, corresponding to Figure 11Figure 12. For reference, cell migration data on flat PDMS substrate are shown (2D).[60]

		T1	T2	T3	H1	H2	H3	2D
		$a > 16\,\mu m$	$16\,\mu m > a > 13\,\mu m$	$13\,\mu m > a$	$r > 16\,\mu m$	$16\,\mu m > r > 10\,\mu m$	$10\,\mu m > r$	
Number of data points in the statistics	N	20 663	15 998	7539	14 402	5794	7504	12 338
Exponents of the l-MSD power law								
Directed runs	α^{dir}	1.81	1.81	1.81	1.78	1.76	1.80	1.81
Random migration states	α^{rm}	1.22	1.21	1.15	1.18	1.17	1.13	1.30
Diffusion coefficient analog ($\mu m^2\,s^{-1}$)	D	0.0090	0.0078	0.0084	0.0068	0.0066	0.0075	0.0072
Instantaneous velocity ($\mu m\,s^{-1}$)								
Directed runs	V^{dir}	0.033	0.036	0.043	0.069	0.053	0.046	0.075
Random migration states	V^{rm}	0.032	0.030	0.028	0.029	0.028	0.027	0.044
Lifetimes of states (s)								
Directed runs	τ^{dir}	119.2	108.0	131.6	91.1	71.5	100.3	155
Random migration states	τ^{rm}	302.2	371.6	286.8	424.7	513.9	555.8	238.7
Angular persistence (deg)								
Directed runs	$\Delta\varphi^{dir}$	14.67	15.83	15.53	17.82	18.85	17.02	16.51
Random migration states	$\Delta\varphi^{rm}$	115.59	116.25	120.31	126.25	127.57	124.84	89.91
Dir-num probability	P^{dir}	20.4	16.2	25.1	8.8	6.4	9.4	35
Random mode probability	P^{rm}	79.6	83.8	74.9	91.2	93.6	90.6	65

Analysis of the instantaneous velocities during directed migration phases reveals a positive correlation with the spatial pillar density, with respective mean values $v_{T1}^{dir} = 0.033\,\frac{\mu m}{s}$, $v_{T2}^{dir} = 0.036\,\frac{\mu m}{s}$ and $v_{T3}^{dir} = 0.043\,\frac{\mu m}{s}$ (Figure 12 G–I). Further, the persistence times of the dir-run modes show a peak in the high density regime (T3), with a mean value of $\tau_{T3}^{rm} = 131.6\,s$. The corresponding distribution of the dir-run phase durations is broadened and shifted to higher values, compared to the low density (T1) and the intermediate regime (T2). Phase duration distributions of the

complementary rm-modes reveal that these phases are shortened in the high density regime (T3) (Figure 16 A–C). In contrast, in the low density regime (T1), the persistence times of the random modes are longer. Compared to trigonal lattices, on flat PDMS substrate cells performing dir-runs exhibit higher migration velocities and larger values for temporal persistence τ, while the temporal persistence of rm-modes is lowered (Table 1 and Table 2).

Together, these results indicate that in the trigonal pillar lattice, the high density regime (T3) facilitates directed cell runs in terms of high velocities and persistence times, as well as increased probability. The enhancement of the dir-run mode by the high density regime supports the concept of pillars acting as topographic 'attractors' to the cells, as introduced by Arcizet *et al.*[60] During directed migration phases, cells show contact-controlled motility and perform pillar-to-pillar runs. While coming into contact with one pillar, a cell simultaneously senses its environment and can start a dir-run to the next pillar, found in its immediate vicinity. At lower pillar densities, cells exhibit a decreased probability of sensing neighboring pillars and thus, dir-runs are less frequent with a smaller mean phase duration, as compared to the high density regions (T3). In conclusion, cells in the dir-run migration state sense pillars as topographic stimuli and orient their motion towards them, performing contact-controlled pillar-to-pillar runs.

4.1.2 Random motion—pillars act as obstacles

In contrast to dir-run states, we find that during random migration (rm) phases the pillars act as obstacles for cell motion. The quantitative analysis of the rm-states reveals a negative correlation of the exponent α_T^{rm} and of the motion velocity v_T^{rm} with the spatial density of the pillar arrays. While the distributions and the mean values of α_T^{rm} exponents are similar for low (T1) and intermediate (T2) density areas, the mean value is lower for dense regions (T3) ($\alpha_{T1}^{rm} \approx \alpha_{T2}^{rm} \approx 1.21, \alpha_{T3}^{rm} = 1.15$, for reference $\alpha_{2D}^{rm} = 1.30$). The distribution of the exponents α_T^{rm} broadens for the high density region (T3) (compared to

(T1) and (T2)), where extremely low values are reached for a large number of data points (Figure 12 D–F and Table 2). A similar trend can be observed for the mean values of migration velocities v_{T1}^{rm} (Table 1). The distribution of the velocities v_{T3}^{rm} shows a distinct shift to lower values compared to less dense pillar regions. Correspondingly, the mean value of angular persistence of cell migration in random mode significantly increases for the high density regime T3 compared to T1 and T2 arrays (Figure 12 J–L and Table 1). Also, the probability for rm-states for high density (T3) areas $P_{T3}^{rm} = 74.9\,\%$ is significantly lower than the respective probabilities $P_{T1}^{rm} = 74.6\,\%$ for low density (T1) areas and intermediate density (T2) areas ($P_{T2}^{rm} = 83.8\,\%$). In addition, the diffusion coefficient analogue decreases for high density areas (T3), compared to T1 ($D_{T3} = 0.0084\ \frac{\mu m^2}{s}$ and $D_{T1} = 0.0090\ \frac{\mu m^2}{s}$). Compared to cell migration on flat substrates, in trigonal lattices the probability for rm-modes as well as the mean velocity in this migration state is lowered and the angular persistence of cell motion is significantly reduced (Table 1). Taken together, these results reflect the 'diffusion-like' character of random probing migration phases, analogue to a passive drift of particles in crowded media: While at high pillar densities the probability for rm-states is reduced in general, the increase in the crowdedness of the environment dampens the particular random motion processes and thus lowers the α_T^{rm} exponent values, as well as the diffusion coefficient analogue D_T (Figure 17). Accordingly, during rm-modes, pillars act as obstacles for cell motion.

4.1.3 Cell trapping at intermediate density regime in isotropic pillar lattice structure

Another important observation is the reduced probability of performing dir-runs for cells migrating in the intermediate density (T2) areas of the trigonal pillar lattices, as compared to the regions of low (T1) and high (T3) pillar density. Here, the inter-pillar distance is in the regime of the typical diameter of Dd cells, so that cells are often attached to several pillars simultaneously. In

this constellation, a cell displaces its center of mass back and forth from one pillar to the other (Figure 12 B). In terms of l-MSD analysis, these cell events are classified as rm-modes, exhibiting low values of the diffusion coefficient analogue, as compared to the migration phases of cells on flat surfaces, which are not 'caged' by topographic cues. Due to this phenomenon, the mean value of diffusion coefficient analogue D_T reaches its minimum, and the mean duration of rm-modes τ_T^{rm} reaches its maximal value in the intermediate density (T2) region. On the other hand, the probability P_T^{dir} and the exponent α_T^{dir} of the dir-runs show the lowest values in the intermediate regime (T2). Additionally, the mean persistence time of dir-runs is minimal in this region ($\tau_{T2}^{dir} = 108.0\ s$). The effect of cell trapping in intermediate density regimes originates from the cell 'attachment' to several pillars at the same time. In this constellation, a stable cell polarization to one particular direction is impeded, and the cell is temporarily trapped in between several pillars, as described in former work.[60] From such a 'trapped' state the cell can only escape by an occasional, strongly asymmetric repolarization, or sensing of distant pillars with exceptionally long protrusions.

4.2 Cell migration in micro-pillar hexagonal arrays of varying side length

To investigate the influence of the local geometric structure of the quasi-3D environment on cell migration, we analyze cell trajectories in micro-pillar arrays of hexagonal lattice geometry (H-arrays) exhibiting a spatial density gradient. H-arrays are congruent with trigonal lattices, where the pillar at the center of each hexagon structure is missing, as shown by Figure 13 A–C. Please consider that the microscopy images are tuned to track the position of the fluorescently labeled cells, thus hiding the high uniformity of the actual pillar dimensions.

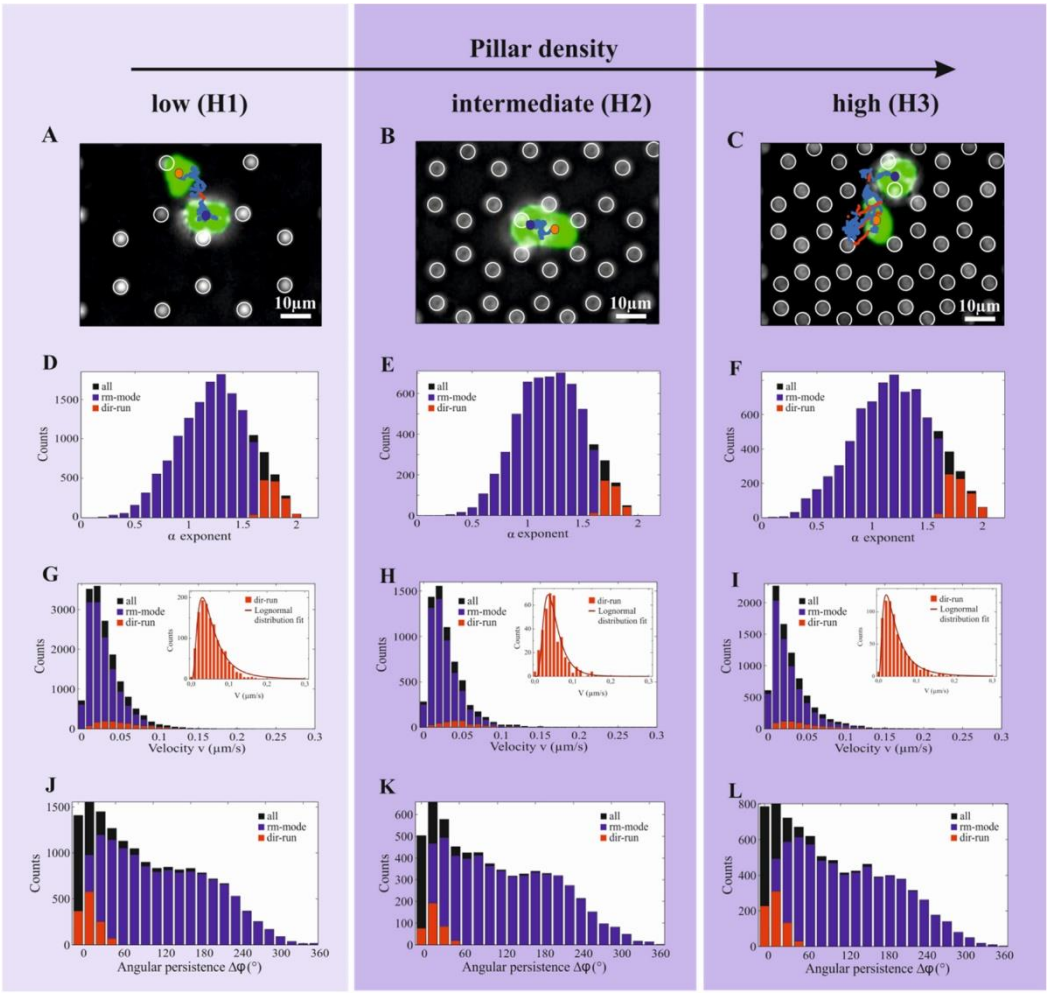

Figure 13: Cell migration in hexagonal lattices of varying pillar density regimes. Cell motility state characteristics for cells migrating in anisotropic hexagonal pillar lattices of low (H1), intermediate (H2) and high density (H3). (A), (B), (C) Typical trajectories of *D. discoideum* cells (green), with phases of directed run states and random probing highlighted in red and blue, respectively. Cells are shown for time points t_1 = 0 min and t_2 = 83 min, with corresponding center of mass positions in blue (t_1) and orange (t_2). White circles highlight positions of the pillars, which are of uniform shape and constant diameter of 4 µm. (D), (E), (F) Distributions of alpha exponents of dir-runs (red), rm-modes (blue) and all values (black), describing the character of cell motion in different density regimes. (G), (H), (I) Corresponding distributions of instantaneous velocities during dir-runs (red) and rm-modes (blue). The overall distributions of instantaneous velocities are shown in black. Insets show velocity distributions of dir-runs, fitted by log-normal distribution function. (J), (K), (L) Angular persistence of cell migration during directed runs (red) and random migration modes (blue). The overall distributions are shown in black.

In trigonal lattices, cells sense a topographically isotropic environment, i.e. the spatial distribution of surrounding pillars is independent of the cell position. By comparison, in the H-arrays the perceived geometry of the surroundings is anisotropic and depends on the position of the cell within the hexagon (honeycomb). In order to extract comparable pillar densities for the analysis of cell migration in hexagonal S2 lattices as in the trigonal lattices, we redefine the

three spatial density regimes as a function of hexagon side length r to $r >$ 16 µm (H1), 16 µm $> r >$ 10 µm (H2), and 10 µm $> r$ (H3) representing low, intermediate and high pillar density in H-arrays, respectively. Again, the inter-pillar distance of intermediate (H2) density region is close to the mean diameter of a Dd cell, while in the low (H1) and in high (H3) density regions, it is comparable to half and to twice the size of these cells, respectively.

4.2.1 General pillar-density dependent cell migration mechanisms

In hexagonal pillar lattices with gradients in inter-pillar distance (H-arrays), l-MSD analysis of cell trajectories ($N =$ 47 cells, $n =$ 27 700 data points) yields analogue trends as for the cell migration behavior observed in trigonal pillar arrays (T-arrays). In detail, the probability for dir-runs P^{dir}, the local-MSD exponents α^{dir} and α^{rm}, as well as the persistence of dir-modes τ^{dir} and the mean instantaneous velocity during rm-modes v^{rm} exhibit analogue dependence on the pillar density in both types of pillar arrays (Table 1). This result suggests that there are general mechanisms controlling cell migration by spatial density in the quasi-3D environment, independent of lattice geometry: contact-controlled pillar-to-pillar guidance during dir-runs and diffusive-like character of rm-modes appear in trigonal as well as in hexagonal arrays of gradient spatial density. In both lattices the migration states show similar dependence on the pillar density. For reference, Table 1 shows respective migration parameters for cell migration in 2D.[60] Reduced probability of topography-induced cell migration confinement in high (H3) density regions leads to increased cell motility in this density regime. The corresponding mean value of D_H is 10–12% higher in high density (H3) regions compared to the low (H1) and intermediate density (H2) regions ($D_{H1} = 0.0068\ \frac{\mu m^2}{s}$, $D_{H2} = 0.0066\ \frac{\mu m^2}{s}$ and $D_{H3} = 0.0075\ \frac{\mu m^2}{s}$).

4.2.2 Influence of topographic anisotropy on cell migration

However, there is also a strong difference in cell migration within the two lattice types. Notably, the absolute values of cell migration parameters are strongly affected by different lattice structures. In particular, the probabilities of dir-runs in H-arrays are less than half compared to T-arrays, and to flat substrates (see Table 1). In addition, the distributions of the exponents α_H^{dir} and α_H^{rm} exhibit a shift to smaller values compared to the corresponding values of α_T^{dir} and α_{HT}^{dir} (Figure 13 D–F and Table 1). Further, the dir-runs in H-arrays are less persistent in terms of state duration and migration direction ($\Delta\varphi$) than in trigonal pillar lattices. Specifically, the duration τ^{dir} is reduced by 23–33 % as compared to T-arrays (and by 36–54 % as compared to flat substrates). The distinct suppression of dir-runs in H-arrays is related to the locally anisotropic structure of the cells' environment. Therefore, the trapping of cells in between several pillars as described above is more probable in hexagonal arrays than in trigonal lattices. Due to the absence of the pillars at the center of each hexagon, the probability for a cell to sense other pillars as topographic stimuli and escape from the trapped state is significantly lowered. Correspondingly, in H-arrays a strong increase in the mean duration of random probing modes τ^{rm} is found. Compared to the respective values found for T-arrays, the values of τ^{rm} are increased by ~40 % for low (H1) and intermediate (H2) regions and even 94 % for the high (H3) density region (and by 78–132 % as compared to 2D substrate) (Table 1). Further, the values of the diffusion coefficient analogue D_H are decreased by 10–25 % with respect to D_T. Thus, although in H-arrays cells can migrate in regions containing fewer obstacles than in the trigonal lattices, cells exhibit reduced motility in terms of the diffusion coefficient analogue D_H.

Another interesting observation concerning the hexagonal lattices is the overall increase in instantaneous velocities of the dir-runs, as compared to T-arrays, in spite of the reduced probability and mean duration of dir-runs. This

means that in H-arrays the rare pillar-to-pillar runs are performed at velocities v_H^{dir} higher than v_T^{dir} (but still lower than v_{2D}^{dir}). This effect can be explained by the absence of center pillars in the hexagons: As the cells sense less topographic stimuli sideways while migrating in dir-run mode, they continue their runs with less disturbance and change of direction.

In summary, we find local anisotropy of lattice structure in H-arrays strongly influences cell migration, leading to a more complex variety of behavior, compared to our findings in isotropic trigonal arrays.

In particular, the probability of topographic cell trapping is significantly increased. Further, due to topographic anisotropy in H-arrays, instantaneous velocities of dir-runs exhibit higher values than in T-lattices, indicating a bias in cell migration behavior.

4.3 Effect of pillar density gradients in trigonal and hexagonal pillar arrays

The above findings reveal that cell motility states are sensitive to the spatial density and local geometry of the cell environment. We identified different mechanisms how cell migration is influenced by the topographic properties of the pillar lattices. To investigate topographic guidance mechanisms in detail, we analyzed the direction of cell motion as a function of both lattice constant and local geometry of the pillar arrays. Therefore, we compared angular distributions of cell motion during dir-runs and rm-modes in both types of pillar lattices.

4.3.1 Cell guidance by topographic cues

To investigate topographic guidance of cells induced by the gradient in pillar density, we analyze all migration directions with respect to dir-runs and rm-modes, along (parallel to) the pillar density gradient. As a most important

result, our data reveal cell guidance in T-arrays (isotropic lattices) towards regions of intermediate pillar density. This bias of cell migration is governed by dir-run states on the one side, coming from low pillar density regions, and by rm-cell motion on the other side, coming from high pillar density regions. In detail, we find that in trigonal pillar arrays, cells preferably migrate from low density areas (T1) towards more dense (T2) regions (Figure 14 A) in dir-run mode. Further, we find that during random probing in high density (T3) regions, the migration direction towards intermediate density area is favored (Figure 14 E). Together, these findings substantiate an overall cell drift to the intermediate density region, which is confirmed by long-term experiments on cell migration in the T-arrays (see last paragraph). We seeded Dd cells ($N = 249$ cells) in trigonal micro-pillar arrays with a gradient in lattice constant and performed spatial distribution statistics of cell positions with respect to the three density regions (T1, T2 and T3) at time points $t_0 = 0$ h and $t_1 = 12$ h. Before starting the measurement, we waited 20 min to let the cells settle firmly, in order to run the experiment from equilibrium conditions. This way, we minimized convection flows and a possible bias by floating of cells. In order to identify non-biased cell migration behavior, we accordingly kept the experimental setting from any mechanical disturbance during the measurement. At time point $t_0 = 0$ h, we find a homogeneous cell distribution over all density regions of the T-arrays. Compared to the time point t_0, at $t_1 = 12$ h the number of cells found in the intermediate pillar density region (T2) increased by 12 %, while it decreased by 3 % in the low density region (T1) and by 33 % in the high density region (T3). To account for cell proliferation during the measurement duration, the acquired cell numbers at time point $t_1 = 12$ h are weighted with the proliferation factor of 1.3. Similar long-time experiments in hexagonal pillar lattices with a gradient in pillar density confirm this trend of a net migration of cells towards regions of intermediate pillar density over 12 h. By these results we show that in both trigonal as well as hexagonal lattices with gradients in pillar density, cells tend

to invade an intermediate density regime. For longer times, we expect this general trend to progress.

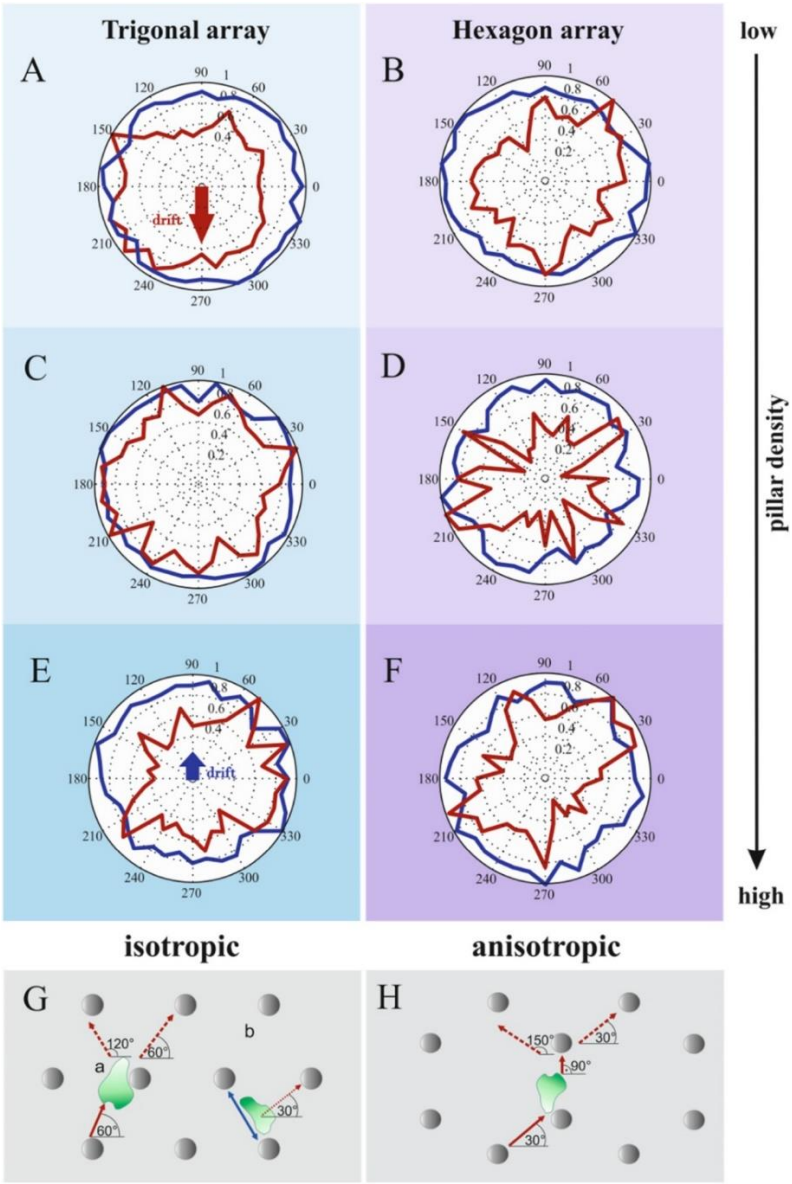

Figure 14: Cell migration in pillar lattices of trigonal and hexagonal lattice geometry. Angle distributions of directed (red) and random (blue) cell motion in trigonal versus hexagonal lattices of large (A) (B), intermediate (C) (D) and small (E) (F) inter-pillar distances. Direction of increasing pillar density is indicated by a black arrow. Blue and red arrows indicate directions of long-term (12 h) cell drift along the gradient in inter-pillar distances in trigonal arrays (A), (E). (G) and (H) illustrate the effect of lattice geometry on contact-induced directed runs in trigonal versus hexagonal pillar fields, respectively. Pillars are shown in gray, cells are shown in green, possible directions of contact-induced runs in isotropic trigonal pillar lattices and anisotropic hexagonal lattices are illustrated by arrows. The resulting peaks in the angular distributions are highlighted by way of example for the intermediate density regimes (C) and (D). (G) shows possibilities for cells to either continue a dir-run (a), or to leave a migration-confined rm-state (b) upon sensing a pillar. In the trigonal lattices (a) yields a 60° peak distribution, while (b) adds peaks every 30° (C). (H) illustrates possible way for a cell to perform a succession of dir-runs in a hexagonal lattice, leading to peaks in angular distributions every 30° (D).

4.3.2 Effect of pillar lattice geometry on cell guidance

In order to investigate mechanisms of the topography-induced cell guidance with respect to the lattice geometry, we analyze the distribution of velocity vector angles of all migrating cells in trigonal and in hexagonal pillar arrays, as shown in Figure 14 A–F. Please note that, by tilt of the trigonal lattice structure of 30° against the gradient in pillar density, we separate guidance effects along the gradient from guidance effects related to the lattice geometry, i.e. the directions of the lattice vectors. More precisely, the peaks in angular distribution of dir-runs reflect the geometry of the pillar arrays (Figure 14 A, C, E), indicating pillar-to-pillar runs in directed migration mode (red).

These peaks originate from the fact that a cell has a significantly increased probability to perform a dir-run upon finding a migration target, i.e. another pillar. In the trigonal pillar lattices, the following mechanisms contribute to the appearance of the peaks. At first, a cell performing a contact-induced pillar-to-pillar run follows a direction along a pillar lattice vector. This mechanism leads to peaks at 60° angles, respectively, as illustrated by cell (a) in sketch principle of Figure 14 G. Secondly, if a cell is trapped between several pillars in rm-state, as described above, sensing another pillar can trigger a switch to a dir-run state and to migration leaving the 'trap'. In this case, the cell starts the run somewhere between the pillars, as illustrated by cell (b) in Figure 14 G. In the trigonal array with equilateral triangles the probability for the new migration direction is tilted by 30° against the lattice vectors, thus resulting in peaks at 30° angles, respectively.

For a cell in the hexagonal pillar field, the lattice geometry provides a reduced number of choices for contact-induced runs between next neighbor pillars, compared to trigonal lattices (T-arrays: six options, H-arrays: three options). This results in a distinct 30°-angle distribution of dir-run peaks in H-arrays, as illustrated by Figure 14 F. Corresponding to the above explanation, the peaks

are most pronounced for angular distributions in intermediate density regions, respectively (Figure 14 C and D), showing that for cells performing pillar-to-pillar runs the migration direction is most precise when the inter-pillar distance approximately corresponds to the cell diameter. Moreover, in H-arrays, the reflection of lattice geometry by the angular distribution of dir-runs is more pronounced than in T-arrays (Figure 14 B, D, F). This highlights again the effect of the different lattice geometries: in comparison to the isotropic trigonal lattice, in the anisotropic hexagonal array the number of pillars perceived by a cell during dir-runs is lower and thus, the cell polarization and the run towards a target pillar is less disturbed (Figure 14 G and H).

In contrast, distinct contact guidance of cells by the pillars is lacking during rm-modes: The angular distributions of random migration phases (blue) in both trigonal and hexagonal arrays do not exhibit a correspondence to lattice geometry (Figure 14 A–F). These results are in good agreement with the findings by Arcizet *et al.*[60]

5. Conclusions

In this work we investigate the influence of the quasi-3D environmental topography on cell migration in order to reveal the underlying mechanisms of cell guidance by local topography. For that purpose, two parameters of the quasi-3D environment are systematically varied: the spatial density and the local geometrical structure. In our experiments, we study amoeboid migration of Dd cells within micro-pillar arrays under controlled variation of lattice constant and lattice geometry. In particular, we compare cell migration in trigonal, isotropic pillar lattices to hexagonal, anisotropic pillar arrays. Based on our observations, we identify general mechanisms governing amoeboid cell migration in quasi-3D environments. We consolidate our findings in a model for the controlled modulation of the two states of amoeboid migration, directed runs and random probing motion.

5.1.1 Effect of spatial density on cell motility

We discriminate cell motion characteristics in three regimes of spatial density with respect to the mean cell size and the cells' radius of sensing. Specifically, the lattice constants range from values close to half the average diameter of a cell to twice the cell size. Our results reveal that spatial density clearly influences amoeboid cell migration modes of directed runs and diffusive-like random probing. Strikingly, directed pillar-to-pillar runs of the cells are facilitated by a high pillar density. This effect is caused by the increased probability for a cell to contact multiple pillars at the same time while performing directed runs, effectively triggering cell polarization. Consolidating this result with the concept of contact-controlled modulation of cell motility, pillars are sensed as attractive topographic stimuli by the cells. In contrast, the random probing motion of cells migrating in arrays of high pillar density shows a diffusive-like character. Here, the mobility is significantly damped by an increasing pillar density, and pillars rather act as obstacles for cell motion. Notably, we find that in a regime where the inter-pillar spacing is in the range of the average cell diameter, cell migration is often confined to small areas in between three and five pillars. As revealed by our analysis, this effect is density-related and results from the geometry of the cell–pillar constellation. Here, the competing attraction by simultaneous pillar contacts inhibits cell polarization that could lead to an escape to the side. Thus, cells are dynamically trapped, moving back and forth between the pillars, without covering large migration distances.

5.1.2 Effect of local geometry on amoeboid migration

To get a detailed view on the specific effect of the local environment geometry on cell migration, we compare cell migration behavior in pillar fields of similar spatial density, but with different lattice structures. Interestingly, we observe distinct changes in the migration behavior upon variation of the pillar lattice geometry: While the density-related effects on cell motility states are analogue

in both environments, the absolute values of the migration parameters are strongly affected by the local geometry of the pillar arrays. Significantly, in hexagonal, anisotropic pillar arrays we find a drastic reduction of the overall cell motility. In particular, the probability of a cell to perform a directed run is significantly decreased for the hexagonal pillar arrays. This effect is the result of an increased occurrence of cell trapping in hexagonal lattice geometry, as compared to the trigonal lattices. Due to the modified lattice geometry with the pillar in the center of each hexagon missing, the cells that are in contact with pillars sense fewer topographic attractive stimuli. This lack of topographic attractors prohibits polarization and thus, cell migration to the side. Accordingly, the area probed by cell motion is reduced, even though the hexagonal lattice basically provides the cells with more space due to the missing center pillar. Interestingly, the same geometric condition leads to a more pronounced pillar-to-pillar guidance along the lattice vectors in terms of increased velocity and directional persistence. This effect is due to the fact that in hexagonal pillar fields, directed cell motion is less disturbed by side attraction.

5.1.3 Topographic guidance of amoeboid cell migration

Our results show that the different topographic influences on amoeboid migration result in guidance of migrating cells. The observed effects reflect the changes in spatial density and local lattice geometry of the pillar fields. In order to investigate the mechanisms of density-gradient guidance, we analyze the angle distributions of the migration directions in trigonal pillar fields with respect to the amoeboid motility modes. By that, we demonstrate that in the low density regime the influence of the local topography on the probability for directed runs is prevalent, leading cells out of these regions towards higher pillar densities. By contrast, in the high density regime, the pillars act as obstacles for the diffusive-like random probing motion. This leads to net shifts of cell positions to lower densities. Consolidating these results, we find that

cells tend to invade regions where the inter-pillar spacing is close to the mean cell diameter.

In terms of guidance by the lattice geometry, we show that the angle distributions of the directed run states reflect the directions of the lattice vectors. This effect is more pronounced for the hexagonal lattice, due to the pronounced pillar-to-pillar guidance. In effect, we demonstrate how the analysis of amoeboid cell migration can yield information on the topographic structure of the cell environment, holding interesting perspectives for further investigations.

5.1.4 Perspectives

Our results provide detailed insights into the mechanisms governing amoeboid cell migration in interaction with the topographic structure of 3D environments. We show that cell migration behavior in specific environments can be predicted in detail by the design of quantitative assays. Thoroughly controlled guidance of amoeboid cell migration holds great prospects for medical applications, such as the design of analytical assays for immune cells and smart materials for wound treatment.

Upon transfer of this piloting approach to migration studies of other cell types, the concept is promising for the development of therapeutics and novel materials for regenerative medicine or tissue engineering. In particular, topographic control of mesenchymal cell migration may offer new opportunities for the design of implant materials upon variation of the density and geometrical properties of micron-scaled surface patterns[124].

6. Appendix

6.1 Competing interests

The authors declare that they have no competing financial interests.

6.2 Acknowledgements

The authors acknowledge Dr Delphine Arcizet and Sofia Capito for optimizing the PDMS structure fabrication technique and Dr Delphine Arcizet for the initial version of the l-MSD analysis algorithm.[12360] We thank Dr Günther Gerisch (MPI for Biochemistry, Martinsried, Germany) for providing the Dd cells. DH acknowledges funding from the Deutsche Forschungsgemeinschaft (grant HE5958-2-1) and Volkswagen-Foundation (grant I85100).

6.3 Supporting information

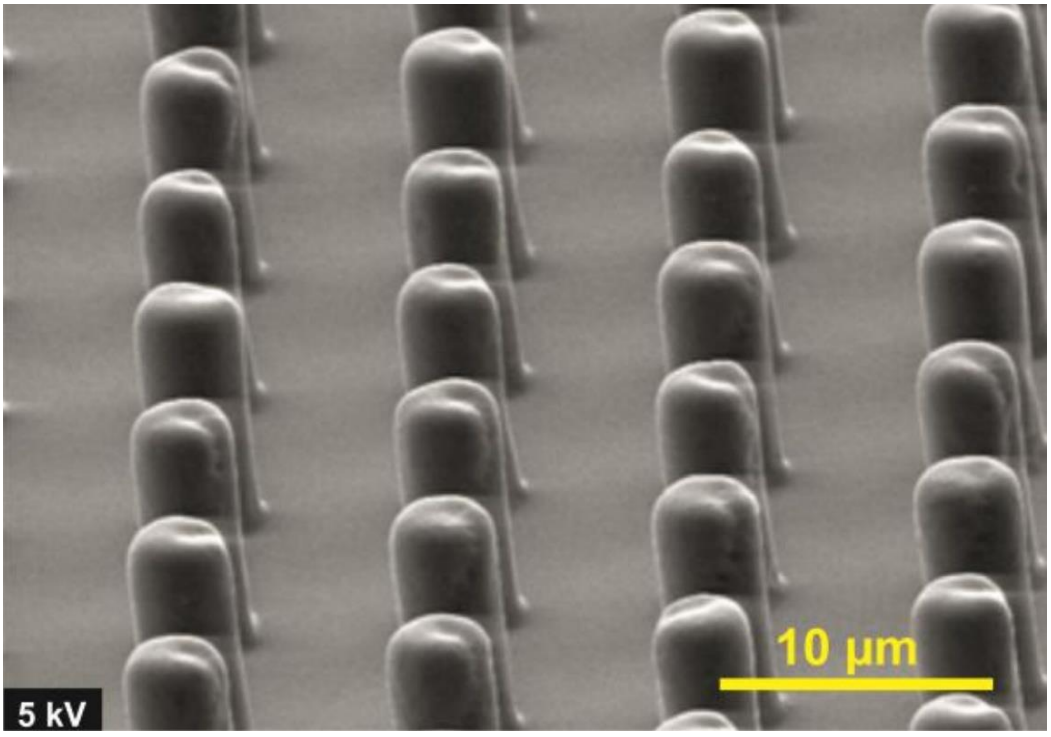

Figure 15: Scanning electron microscopy (SEM) image of PDMS micro-pillar sample fabricated by standard procedure. Pillars are highly reproducible with variations on nm-scale, due to the precisely controlled fabrication process.

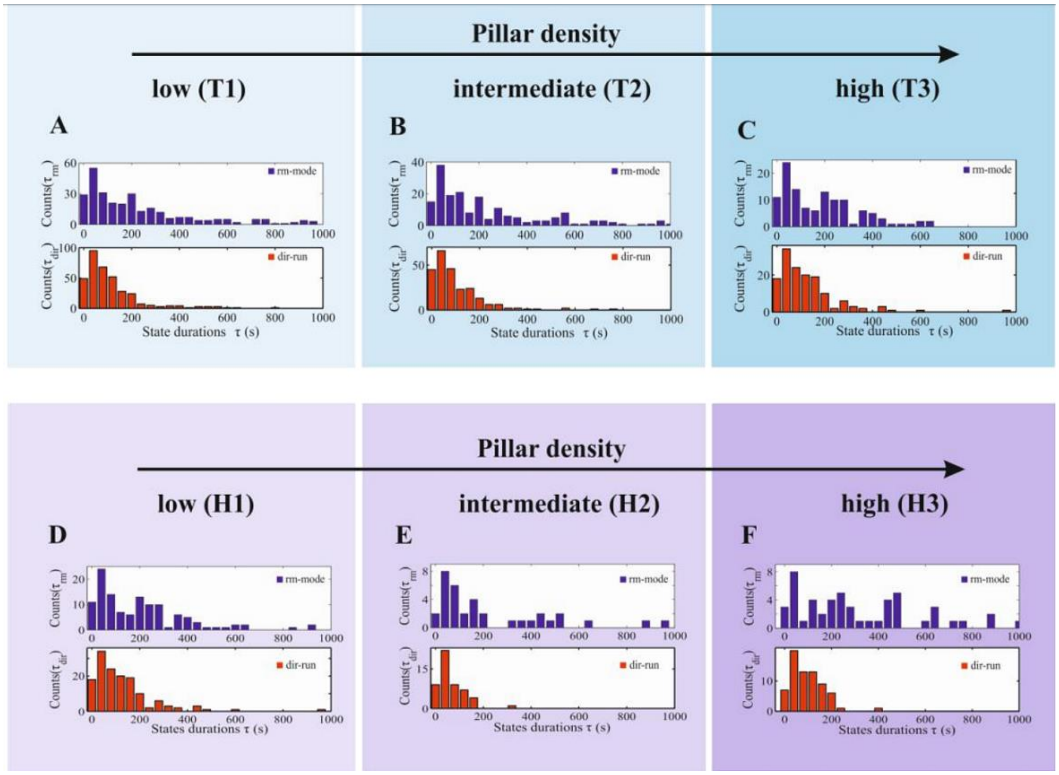

Figure 16: (A-C) Distributions of the duration of cell migration states for cells migrating in isotropic trigonal pillar lattices of low (T1), intermediate (T2) and high density (T3) (see Figure 12). Lifetimes found for directed runs and random probing states labeled by red and blue color, respectively. (D-E) Distributions of the duration of cell migration states for cells migrating in anisotropic hexagonal pillar lattices of low (H1), intermediate (H2) and high density (H3) (see Figure 13). Lifetimes found for directed runs and random probing states are labeled by red and blue color, respectively.

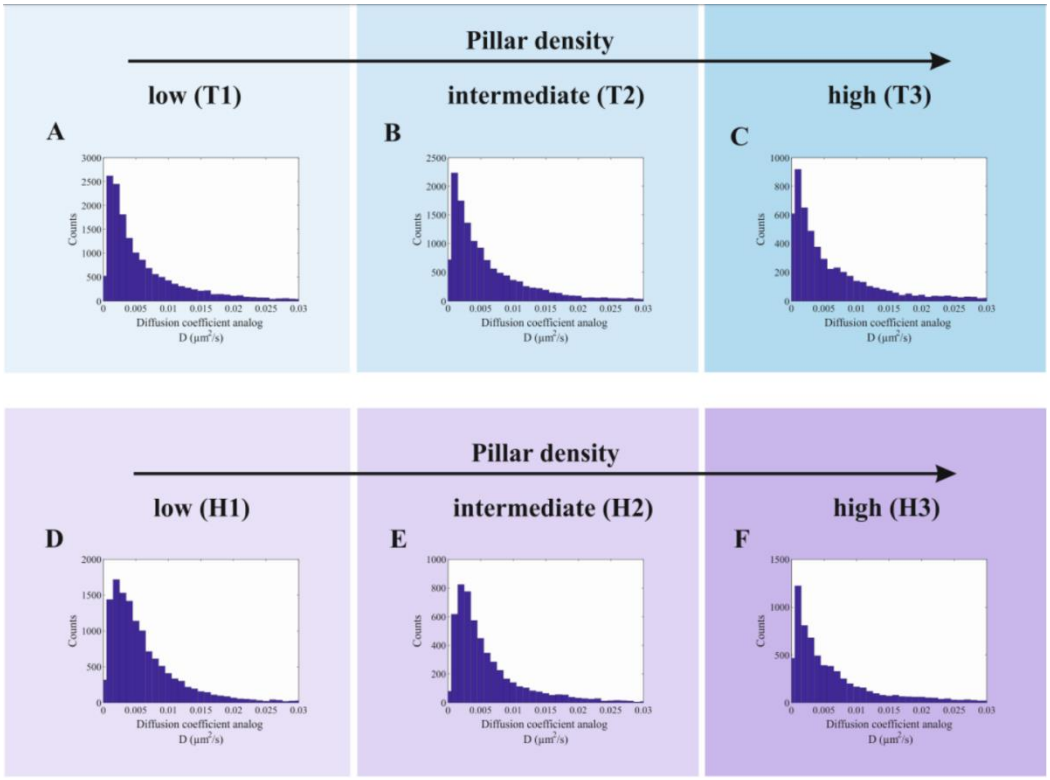

Figure 17: (A-C) Distributions of the diffusion coefficient analog D of random cell migration (rmmodes) for trigonal pillar lattices of low (T1), intermediate (T2) and high density (T3). (D-E) Distributions of the diffusion coefficient analog D of random cell migration (rm-modes) for hexagonal pillar lattices of low (H1), intermediate (H2) and high density (H3).

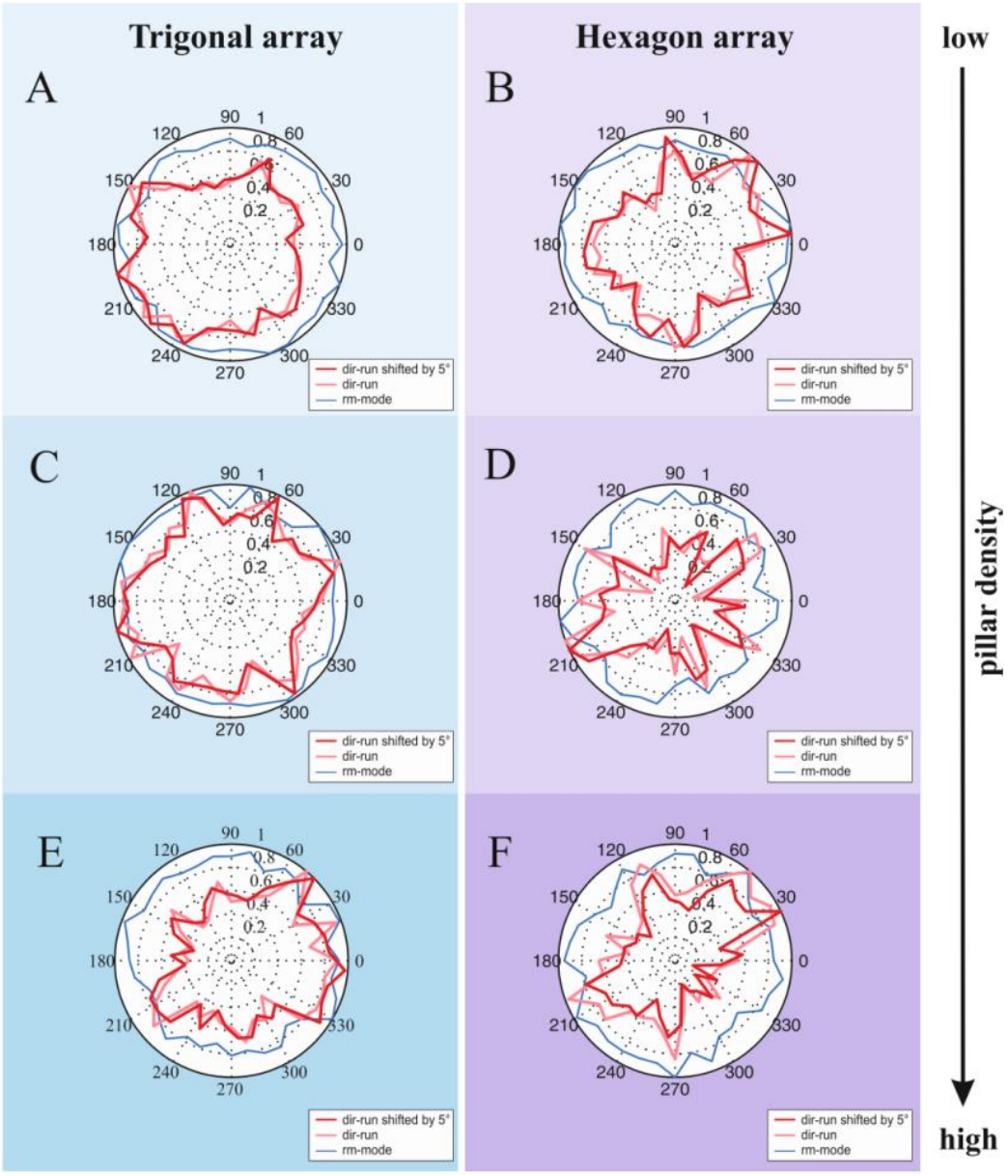

Figure 18: Robustness test of angle distribution analysis of directed cell motion (dir-runs). All angle distributions of cell migration in low (A,B), intermediate (C,D) and high density regimes (E,F) of trigonal and hexagonal pillar arrays are shown with 10°-cumulated values. The original angle distributions for rm-modes (light blue) and dir-runs (light red) are shown corresponding to Figure 14 A-F, respectively. A second analysis of the same data under 5°-shifted data binning is additionally shown for directed cell migration (dir-runs) (dark red). Comparison shows that the peaks found in the original angle distributions are retained in the shifted distributions, proving the robustness of the results. Representative peaks are indicated by arrows.

Table 2: Statistical analysis of variables characterizing cell migration in T-arrays as a function of pillar lattice geometry and spatial density by the motility state parameters, the diffusion coefficient analog D, the exponent α, α_{dir}, α_{rm}, the instantaneous velocities V, V_{dir}, V_{rm}, the durations of the states τ_{dir} and τ_{rm}, and the direction persistence $\Delta\varphi$, $\Delta\varphi_{dir}$, and $\Delta\varphi_{rm}$.Cell migration in T-arrays is evaluated at first by the mean values and the median of the obtained numerical distributions (see Figure 12). The distributions are characterized further by the different measures for deviation: the mean absolute deviation, the median absolute deviation and the standard deviation of the mean value, which allow determining the relative asymmetry of the distributions (skewness), respectively. Additionally, the 1- quantile and the 3-quantile of the distributions are shown.

		Diffusion coefficient analog [$\mu m^2/s$]	Exponent of I-MSD power law			Instantaneous velocity [µm/s]			Life times of states [s]		Angular persistence [°]		
		D	α	α_{dir}	α_{rm}	V	V_{dir}	V_{rm}	τ_{dir}	τ_{rm}	$\Delta\varphi$	$\Delta\varphi_{dir}$	$\Delta\varphi_{rm}$
T1	Mean value	0.0090	1.3384	1.8129	1.2170	0.0317	0.0332	0.0317	119.20	302.17	95.04	14.67	115.59
	Mean absolute deviation	0.0084	0.2942	0.0858	0.2420	0.0200	0.0160	0.0200	83.53	261.70	68.97	9.97	66.75
	Median	0.0041	1.3641	1.8062	1.2566	0.0232	0.0291	0.0232	80.00	180.00	72.65	10.78	100.85
	Median absolute deviation	0.0028	0.2544	0.0790	0.2146	0.0119	0.0134	0.0119	50.00	130.00	56.81	7.07	60.85
	Standard deviation	0.0166	0.3588	0.1026	0.2943	0.0295	0.0203	0.0295	130.30	415.99	81.39	12.41	78.77
	Quantile 0.25	0.00189	1.13798	1.7297	1.0209	0.0169	0.03647	0.0131	40.00	60.00	14.84	4.783	48.56
	Quantile 0.75	0.00949	1.66094	1.8889	1.4585	0.0606	0.10375	0.04	142.5	340.00	137.12	21.17	175.53
	Skewness	6.61811	-0.3682	0.2518	-0.616	2.1232	1.10588	2.9832	3.11	3.34	0.88	1.086	0.54
T2	Mean value	0.0078	1.3054	1.8054	1.2088	0.0301	0.0364	0.0301	107.95	371.62	99.98	15.83	116.25
	Mean absolute deviation	0.0069	0.2842	0.0864	0.2402	0.0188	0.0170	0.0188	79.41	344.98	69.57	10.70	67.42
	Median	0.0041	1.3286	1.7965	1.2473	0.0226	0.0318	0.0226	70.00	190.00	77.82	11.75	102.29
	Median absolute deviation	0.0029	0.2480	0.0812	0.2124	0.0122	0.0099	0.0122	50.00	140.00	58.22	7.77	62.69
	Standard deviation	0.0143	0.3488	0.1027	0.2924	0.0259	0.0228	0.0259	129.04	511.75	81.12	13.01	78.66
	Quantile 0.125	0.0017	1.07516	1.719	1.0132	0.014	0.03876	0.0122	30.00	60.00	22.36	5.187	46.69
	Quantile 0.175	0.00905	1.58983	1.8812	1.4437	0.051	0.10058	0.0396	140.00	497.5	155.94	23.83	179.05
	Skewness	11.0048	-0.3137	0.3257	-0.602	2.1549	1.12805	2.0791	4.06	2.87	0.70	0.92	0.48
T3	Mean value	0.0084	1.3138	1.8128	1.1462	0.0280	0.0431	0.0279	131.59	286.79	93.97	15.53	120.31
	Mean absolute deviation	0.0079	0.3492	0.0847	0.2887	0.0192	0.0175	0.0192	88.22	236.58	74.00	10.71	72.86
	Median	0.0039	1.3604	1.8041	1.2021	0.0193	0.0408	0.0192	95.00	190.00	60.20	11.34	104.94
	Median absolute deviation	0.0032	0.3120	0.0779	0.2490	0.0114	0.0145	0.0113	55.00	140.00	49.89	7.70	67.41
	Standard deviation	0.0123	0.4221	0.1017	0.3505	0.0276	0.0226	0.0276	129.01	377.94	86.42	13.03	84.62
	Quantile 0.125	0.00137	1.0391	1.7322	0.9195	0.0123	0.02912	0.0098	50.00	57.5	16.43	4.97	44.28
	Quantile 0.175	0.0099	1.67679	1.8904	1.4317	0.0491	0.07688	0.036	180.00	315	151.05	23.03	186.65
	Skewness	3.0414	-0.5117	0.2568	-0.631	2.1103	1.75268	2.5447	2.76	2.89	0.89	0.96	0.50

Table 3: Statistical analysis of variables characterizing cell migration in H-arrays as a function of pillar lattice geometry and spatial density by the motility state parameters, the diffusion coefficient analog D, the exponent α, α_{dir}, α_{rm}, the instantaneous velocities V, V_{dir}, V_{rm}, the durations of the states τ_{dir} and τ_{rm}, and the direction persistence $\Delta\varphi$, $\Delta\varphi_{dir}$, and $\Delta\varphi_{rm}$. Cell migration in H-arrays is evaluated at first by the mean values and the median of the obtained numerical distributions (see Figure 13). The distributions are characterized further by the different measures for deviation: the mean absolute deviation, the median absolute deviation and the standard deviation of the mean value, which allow determining the relative asymmetry of the distributions (skewness), respectively. Additionally, the 1- quantile and the 3-quantile of the distributions are shown.

		Diffusion coefficient analog [$\mu m^2/s$]	Exponent of I-MSD power law			Instantaneous velocity [µm/s]			Life times of states [s]		Angular persistence [°]		
		D	α	α_{dir}	α_{rm}	V	V_{dir}	V_{rm}	τ_{dir}	τ_{rm}	$\Delta\varphi$	$\Delta\varphi_{dir}$	$\Delta\varphi_{rm}$
H1	Mean value	0.0068	1.2289	1.7815	1.1756	0.0289	0.0691	0.0288	91.07	424.68	116.72	17.82	126.25
	Mean absolute deviation	0.0047	0.2583	0.0723	0.2307	0.0160	0.0257	0.0159	60.75	344.06	69.94	10.75	67.46
	Median	0.0046	1.2427	1.7707	1.2085	0.0236	0.0711	0.0235	70.00	280.00	103.00	14.33	116.19
	Median absolute deviation	0.0026	0.2225	0.0658	0.2029	0.0116	0.0210	0.0116	40.00	210.00	65.77	8.86	63.67
	Standard deviation	0.0073	0.3197	0.0878	0.2812	0.0214	0.0315	0.0212	79.85	474.06	81.54	12.92	78.99
	Quantile 0.25	0.00239	1.01792	1.7105	0.9846	0.0143	0.02892	0.0136	30.00	80.00	37.06	7.14	57.61
	Quantile 0.75	0.00843	1.47806	1.8431	1.394	0.0415	0.06945	0.0383	120.00	527.5	174.89	25.9	187.41
	Skewness	3.51838	-0.1651	0.483	-0.461	2.0458	1.06237	1.6902	1.54	2.02	0.50	0.77	0.40
H2	Mean value	0.0066	1.2049	1.7604	1.1668	0.0280	0.0537	0.0279	71.53	513.90	120.59	18.85	127.57
	Mean absolute deviation	0.0048	0.2420	0.0582	0.2198	0.0153	0.0267	0.0152	43.16	523.27	70.01	10.24	68.12
	Median	0.0042	1.2079	1.7505	1.1793	0.0228	0.0482	0.0227	60.00	160.00	109.18	14.73	118.86
	Median absolute deviation	0.0023	0.2148	0.0518	0.2010	0.0108	0.0128	0.0107	30.00	120.00	67.93	6.98	65.40
	Standard deviation	0.0075	0.2953	0.0692	0.2650	0.0207	0.0380	0.0205	59.52	757.73	81.66	12.24	79.73
	Quantile 0. 25	0.0023	0.99328	1.7101	0.9752	0.0141	0.03023	0.0135	30.00	70.00	37.16	9.465	57.81
	Quantile 0. 75	0.00802	1.43328	1.8128	1.3757	0.0393	0.06095	0.0368	95.00	502.5	179.01	27.34	190.86
	Skewness	3.76634	-0.0333	0.2655	-0.285	1.8243	1.21285	1.9102	2.11	2.13	0.45	0.75	0.36
H3	Mean value	0.0075	1.1875	1.7956	1.1248	0.0272	0.0460	0.0271	100.28	555.78	114.76	17.02	124.84
	Mean absolute deviation	0.0066	0.2862	0.0826	0.2521	0.0174	0.0196	0.0174	56.61	484.67	69.35	10.18	66.77
	Median	0.0039	1.1942	1.7779	1.1502	0.0203	0.0371	0.0202	90.00	290.00	101.28	14.22	115.14
	Median absolute deviation	0.0029	0.2492	0.0714	0.2260	0.0117	0.0098	0.0116	50.00	200.00	64.76	8.30	63.41
	Standard deviation	0.0116	0.3529	0.0987	0.3071	0.0235	0.0241	0.0234	70.97	802.62	80.95	12.40	78.27
	Quantile 0. 25	0.00152	0.94699	1.7152	0.9136	0.0109	0.0223	0.0103	40	110	35.981	6.73	57.58
	Quantile 0. 75	0.00882	1.456	1.8674	1.3665	0.0388	0.06098	0.0362	140	525	172.05	24.5	186.14
	Skewness	6.75969	-0.109	0.4258	-0.407	1.8908	1.55468	1.8039	1.27	2.90	0.51	0.78	0.40

IV. Cell Migration on Nanostructured Surfaces

This chapter was published as

"Nanostructured surfaces of biodegradable silica fibers enhance directed amoeboid cell migration in a microtubule-dependent process"

by Martin Emmert, Patrick Witzel, Miranda Rothenburger-Glaubitt and Doris Heinrich

in RSC Advances 7 (2017), Nr.10, S.5708-5714.

This study builds upon my master's thesis "Investigation and analysis of living cell interaction with silica fibers" that was prepared in 2014 at Fraunhofer ISC.

Julius-Maximilians-
UNIVERSITÄT
WÜRZBURG

Fakultät für
CHEMIE UND
PHARMAZIE

Erklärung zur Autor:innenschaft

Nanostructured surfaces of biodegradable silica fibers enhance directed amoeboid cell migration in a microtubule-dependent process
Martin Emmert*, Patrick Witzel, Miranda Rothenburger-Glaubitt and Doris Heinrich, RSC Advances 7, 2017, Nr.10, 5708-5714 (* = Hauptautor:innen)

Detaillierte Darstellung der Anteile an der Veröffentlichung (in %)
Angabe Autor:innen (ggf. Haupt- / Ko- / korrespondierende/r Autor:in) mit Vorname Nachname (Initialen)

Martin Emmert (me), Patrick Witzel (pw), Miranda Rothenburger-Glaubitt (mrg), Doris Heinrich (dh)

Autor:in	me	pw	mrg	dh	A5	A6	A7	A8	A9	A10	A11	∑ in Prozent
Materialherstellung	30%	0%	70%	0%								100%
Materialcharakterisierung	95%	0%	0%	5%								100%
Zellexperimente	90%	5%	0%	5%								100%
Auswertung	45%	35%	0%	20%								100%
Verfassen der Veröffentlichung	95%	5%	0%	0%								100%
Korrektur der Veröffentlichung	30%	30%	0%	40%								100%
Koordination der Veröffentlichung	50%	0%	0%	50%								100%
Summe	62,1%	10,7%	10,0%	17,1%								100%

1. Abstract

Cell motion and in particular amoeboid migration is crucial for the survival of living organisms. To advance biomedical research, a constant need for novel materials and surface structures arises, improving immigration of cells into artificial structures used for tissue engineering and for advancing therapy in modern medicine. This work focuses on investigating amoeboid single-cell migration on intrinsically nano-structured, biodegradable silica fibers in comparison to chemically equivalent plain glass surfaces. Cell migration trajectories are classified into directed runs and quasi-random migration by a local mean squared displacement (LMSD) analysis. We find that directed movement on silica fibers is enhanced in a significant manner by the fibers' nanoscale surface-patterns. Further, cell adhesion on the silica fibers is a microtubule-mediated process. Cells lacking microtubules detach from the fibers, but adhere well to glass surfaces. Knock-out mutants of myosin II migrating on the fibers are as active as cells with active myosin II, while the migration of the knock-out mutants is hindered on plain glass. Identifying relevant cytoskeletal compounds for cell migration in 2D *vs.* 3D will help to optimize materials or surfaces that boost specific migration strategies to open up new opportunities for innovative diagnostic and therapeutic concepts.

2. Introduction

Cell migration is crucial in the human organisms, involving essential processes like embryonic morphogenesis[125,126] or wound healing.[39,40] The introduction of novel scaffold materials to support or enhance cell migration is a major topic in tissue engineering and modern medicine, as cell behavior *in vitro* and *in vivo* is strongly influenced by the nanostructured surface of artificial scaffolds[127] or the extracellular matrix.[128] Amoeboid-like cell migration is an efficient concept of cell migration,[100] *e.g.* performed by stem cells and different types of immune cells like monocytes,[68] neutrophils[129] and lymphocytes.[130] These cell types can

travel long distances in reaction to chemical cues, exit blood vessels and crawl through tissues.[38,129] As several signalling cascades and basic cytoskeletal mechanisms are similar to mammalian cells, the social amoeba *Dictyostelium discoideum* is a perfect model organism for the study of amoeboid migration.[131] Amoeboid cells react to changes in their environment very quickly, which manifests in the amoeboid cells' ability to respond to external cues within seconds and to change their direction of movement within a few minutes.[112,132] The cytoskeleton provides the highly dynamic system for the transport of regulatory proteins and cellular polymers that realize these rapid changes in migration direction or the switching from resting states to active migration: in reaction to external topographic and chemotactic stimuli, an amoeboid cell polarizes by force generation of the actomyosin cytoskeleton.[133] At first, the center of mass is moved into the direction of migration by extension of protrusions upon actin polymerization and material transport by stabilized microtubules.[107] Migration is then achieved by further protrusion at the front and myosin II-driven contraction and concurrent retraction of adhesion sites at the rear.[102] This complex interplay between actin polymerization, motor proteins and the microtubule network is crucial for force generation between substrate and cell.[70]

As eukaryotic cells possess sensing and adhesion features in the nanometer range, directed cell migration can be induced and supported by topographic cues on the substrate.[134] In the model of contact-reinforced motility, these topographic guidance effects are explained by a stabilization of pseudopods upon contact with a topographic stimulus, increasing the probability for directed migration in the direction of the stimulus.[60,135] Thus, the introduction of three-dimensional structures or surface patterns that support cytoskeletal migration mechanisms can enhance cell migration without presentation of additional chemical attractants and find wide applications in medicine and medical research. For example, scaffolds made from such smart materials could greatly increase the efficiency of cell seeding in tissue engineering or serve as

a scaffold for the repair of tissue injuries.[136] This work investigates (i) the influence of the intrinsic surface nanotopography of biodegradable silica fibers on amoeboid single cell migration and (ii) the role of specific cytoskeletal structures during migration on these fibers, in particular microtubules and myosin II. Our findings will contribute to the evaluation of the fiber material as a scaffold for applications in *in vitro* and *in vivo* situations.

3. Materials and methods

3.1 Fabrication and characterization of silica fiber samples

Silica fibers were spun directly onto microscopy cover glasses for cell migration experiments. The standard precursor was prepared in a three-step synthesis: a mixture of tetraethoxysilane (TEOS), ethanol (EtOH), distilled water (H_2O) and nitric acid (HNO_3) (all from Sigma-Aldrich Chemie GmbH) was stirred at room temperature for several hours. EtOH was removed from the mixture in a rotary evaporator, followed by sol ripening carried out at low temperature.[15] During sol ripening, an abrupt increase of viscosity was detected. For fiber spinning, the gel was filled into a pressure vessel and extruded through a nozzle plate at pressures of 15–20 bar. After exiting the 150 µm nozzle diameter, the fibers were led through a laminar air flow with a drop distance of two meters onto microscopy cover glasses (borosilicate glass 3.3, 80.6 % SiO_2, 12.5 % B_2O_3, 4.2 % NaO, 2.2 % Al_2O_3, 0.5 % trace elements, Th. Geyer GmbH & Co. KG), placed on a programmable *X*–*Y*-table (Bosch Rexroth AG). The chemical composition of the resulting silica gel fibers was determined to be $[Si(OH)_{0.2}O_{1.9}]_n$ by thermal analysis in a previous work.[15] Due to the high silica content, the chemical composition of the cover glasses is very similar to the fiber surface. The fiber diameter, shape and surface homogeneity were analyzed by SEM (Supra 25, Carl Zeiss Microscopy GmbH) after platinum sputtering. Figure 19 A shows a fiber fixed on a glass substrate. Due to a collapse of the circular surface upon

solvent diffusion and evaporation in laminar air flow, free-standing fibers exhibit a dog-bone-like shape (Figure 19 B). The dog-bone-shape at the surface is retained upon when fibers are directly spun onto cover glasses for migration experiments (Figure 19 C). Fiber widths were measured to be 60 ± 20 µm with fiber heights of 24 ± 8 µm. The surface of freshly fabricated fibers is smooth, with no distinct surface patterns (Figure 19 D). As the fiber material is biodegrading at a rate of 10–100 nm per day,[15] nano-sized surface patterns emerge upon contact to aqueous media. SEM investigations on fibers that have been stored in simulated body fluid for several days revealed pits and elevations on the fiber surface with feature sizes below 200 nm (Figure 19 E). In comparison, the surface of the cover glass around the fibers appears smooth (Figure 19 A and Figure 25), exhibiting an average surface roughness below 0.3 nm[137]. Thus, the comparison of amoeboid cell migration on silica fibers with cover glasses of similar chemical composition – but a flat surface – is expected to reveal the impact of the fibers' nanoscale topography on amoeboid cell migration.

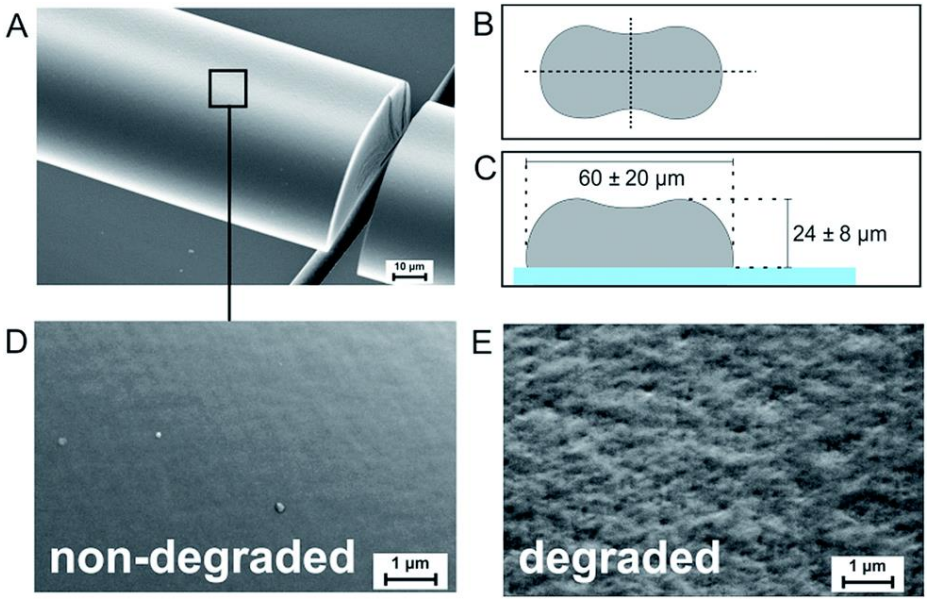

Figure 19: SEM micrograph of the silica fibers. (A) Silica fiber spun onto microscopy cover glass as used in the migration experiments (glass broken for visualization of fiber cross section). (B) Schematic illustration of the typical dog-bone shape of the fibers. (C) Schematic illustration of fiber samples for migration experiments (grey = fiber, blue = cover glass). (D) Surface of a freshly prepared silica fiber. (E) Silica fiber after 10 days of degradation in simulated body fluid (SBF) with pronounced surface patterns.

3.2 Cell preparation and migration experiments

Different mutants of the *D. discoideum* strain AX2 were cultured for the experiments. For wild-type migration, cells expressing homogenously distributed Green Fluorescent Protein (GFP) in the cytoplasm (FreeGFP) were used. Additional experiments on myosin II-deficient cells were carried out with a myosin II null mutant with GFP-tagged LimEΔcc. All cell cultures were grown at 19-21 °C in Petri dishes at ambient air. $20\,\frac{\mu g}{mL}$ gentamycin (G-418-Biochrom A2912, Biochrom AG) was added to the culture medium of FreeGFP cells. For myosin II null mutants, gentamycin and the additional antibiotic blasticidin (Sigma-Aldrich Chemie GmbH) were used at a concentration of $10\,\frac{\mu g}{mL}$. Prior to the experiments, the cells were washed (four times) with phosphate buffered saline (PBS). Each step consisted of centrifugation at 2000 rpm for 4 minutes (Eppendorf MiniSpin® Plus, Eppendorf AG) and resuspension of the obtained cell pellet in PBS. For experiments, *D. discoideum* cells suspended in PBS were pipetted onto silica fibers on cover glasses at densities ranging from 300 000 to 410 000 cells per cm^2, the suitable cell number for the observation of up to 10 cells in a field of view while excluding direct cell–cell interactions during cell tracking. Image acquisition was performed with a Nikon Eclipse Ti microscope (Nikon, Germany) and a 20× objective (Nikon, Germany). Fluorescence white light illumination was obtained by Intensilight (Nikon, Germany). For GFP imaging, an excitation filter (F36-525 HC, AHF, Germany) ensured excitation wavelengths of 457–487 nm and detection wavelengths of 500–540 nm. The setup is equipped with an EM-CCD camera (Hamamatsu, Japan) for detection of the fluorescence signal. A 100 W halogen lamp contained in the microscope was used for bright field illumination. Fluorescence images were acquired every 7 seconds for at least 45 minutes to exclude short-time effects. To minimize the excitation stress for the cells, exposure times were kept below 100 ms. Additionally, a bright field image was taken for every time point to ensure proper fiber localization.

For experiments with cells deprived of microtubules, the microtubule-depolymerizing agent benomyl (Sigma-Aldrich Chemie GmbH) has been used at a concentration of 50 µM on FreeGFP cells. Cell adherence after benomyl treatment was investigated by moving the microscopy table during live video-acquisition and the determination of the number of adherent and non-adherent cells.

3.3 Migration analysis

For tracking analysis of migrating cells, the fluorescence image stacks were loaded into the image processing software ImageJ (National Institutes of Health, USA), analogously edited and converted to binary images. The obtained sequences of binary images were then analyted by the ImageJ plugin "Cell Evaluator" which tracks the center of mass of each cell.[122] A text file is created, containing the X–Y coordinates for each time point. The cell trajectories were analyzed by the MATLAB® algorithm "CellMovement",[60,138] distinguishing two modes of cell migration: directed cell runs and quasi-random migration phases. It utilizes a local mean squared displacement (LMSD), which is calculated for every time point t_i over a rolling time window of 16 frames (corresponding to a duration $T = 112$ s) as a function of different lag times τ:[123]

$$\langle \Delta R^2(\tau) \rangle_i = \langle (R(t_i + \tau) - R(t_i))^2 \rangle_{t - \frac{T}{2} < t_i < t + \frac{T}{2}} \qquad (1)$$

The obtained $\langle \Delta R^2(\tau) \rangle$ is then fitted by the power law

$$\frac{\langle \Delta R^2(\tau) \rangle}{l^2} = A \left(\frac{\tau}{\tau_0} \right)^{\alpha} \qquad (2)$$

Where $l = 1$ µm is a chosen unit reference length and $\tau_0 = 1$ s is a reference time, so the prefactor A carries no physical dimension.[139] The exponent α is a dimensionless coefficient describing the migration mode of a cell together with the trajectory's angle deviation. For a directed run with constant velocity v_d, α is expected to be ≈ 2 and the variation in angle < 0.9. For $\alpha < 2$,

the trajectory is classified as quasi-random motion with a generalized diffusion coefficient D retrieved from the prefactor A of the power law fit of equation (2) by

$$D = \frac{\langle \Delta R^2(\tau_0) \rangle}{2d\tau_0} = \frac{Al^2}{2d\tau_0} \quad (3)$$

where d is the number of spatial dimensions.[139] For the directed run modes a new fit of the data is performed with $\alpha = 2$, returning the local directed velocity v_d by

$$\langle \Delta R^2(\tau) \rangle = v_d^2 \tau^2 \quad (4)$$

4. Results and discussion

4.1 Migration analysis

We investigate amoeboid cell migration on nanostructured silica fibers in comparison to chemically analog flat glass surfaces in order to reveal the impact of the fibers' nanoscale topography on amoeboid cell migration. Fibers exhibit a dog-bone-shape (Figure 19 A, width = 60 ± 20 µm, height = 24 ± 8 µm) and nanoscale surface patterns emerging upon biodegradation in aqueous media (Figure 19 E).

Figure 20 A shows a cell migration trajectory: every 7 s, *D. discoideum* cells were imaged in bright field and the fluorescent channel. The fluorescent channel image was binarized and each cell's center of mass was tracked for every time point. By local mean squared displacement (LMSD) analysis, the trajectories were divided into directed cell runs (red) and quasi-random migration (black). This analysis is based on a rolling window of 16 frames, in which the LMSD is calculated as (1) (see Materials and methods) and the exponent α (2) (see Materials and methods) determines directed runs. In these directed migration states, cells are more polarized (Figure 20 B) and exhibit

extended sections of directionally persistent movement. These are interrupted by short phases of quasi-random migration, where the cell is protruding into different directions without significant movement of the center of mass (Figure 20 B). We analyzed 24 438 data points (47.5 h) on flat glass and 22 413 data points (43.6 h) on silica fibers. Figure 21 displays cell migration parameters of the LMSD analysis and their mean values.

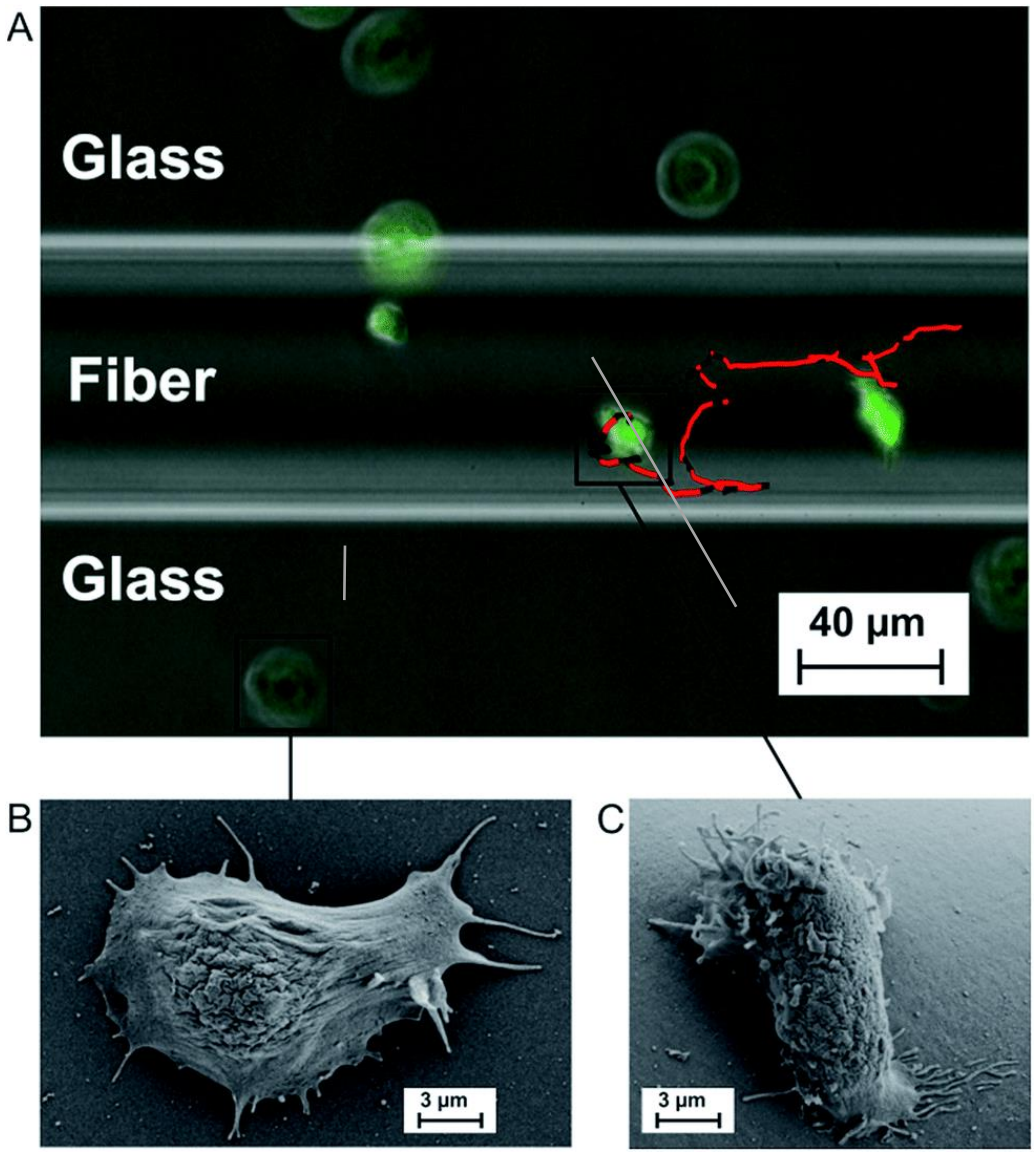

Figure 20: (A) Multi-channel microscopy image (brightfield + fluorescence) with overlayed single cell trajectory over the whole experiment. In the trajectory, random (black) and directed (red) migration states are distinguished. (B) SEM micrograph of a single non-polarized D. discoideum cell on plain glass. (C) SEM micrograph of a polarized D. discoideum cell on the fiber surface.

The distribution of instantaneous velocities for cells migrating on silica fibers (Figure 21 B) is significantly shifted to higher values as compared to migration on plain glass (Figure 21 C). The overall mean velocity increases by 78 % for cells migrating on the fibers. The velocity distribution of directed states (red) is clearly increased on silica fibers, while the number of non-directed, slow tracks is significantly decreased as compared to the 2D glass surface.

Table 4: Extracted migration parameters, FreeGFP representing wild-type migration, MyoII^0 the migration of myosin II deficient cells.

		Coverglass		Fiber	
		FreeGFP	**MyoII^0**	**FreeGFP**	**MyoII^0**
Number of cells	N	46	31	49	30
Data points	n	24 438	10 212	22 413	10 084
Mean alpha value	$\bar{\alpha}$	1.45	1.34	1.62	1.61
Mean diffusion coefficient $\left(\frac{\mu m^2}{s}\right)$	$\bar{D}$	0.0026	0.0014	0.0056	0.0038
Mean instantaneous velocity					
Of directed states $\left(\frac{\mu m}{s}\right)$	$\bar{v}_A$	0.057	0.046	0.104	0.081
Overall $\left(\frac{\mu m}{s}\right)$	$\bar{v}_{all}$	0.041	0.029	0.073	0.059
Mean duration of state lifetimes					
Of directed states (s)	$\bar{\tau}_{all}$	32.5	39.2	45.4	52.0
Of quasi-random states (s)	$\bar{\tau}$	199.5	171.7	92.1	99.2
% of time spent in phases					
Directed		11	15	27	30
Quasi-random		85	81	64	61

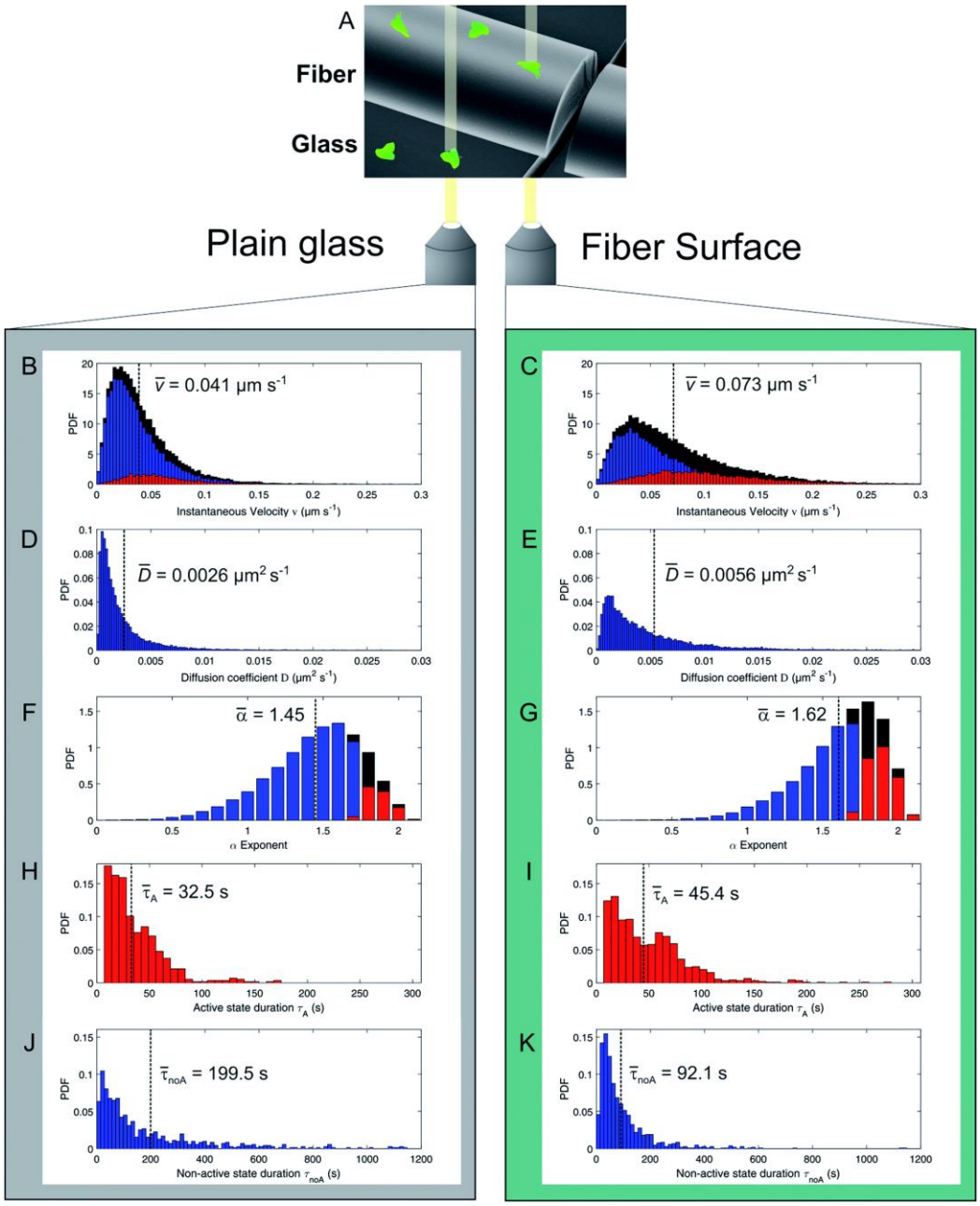

Figure 21: Cell migration analysis of D. discoideum FreeGFP cells. (A) Experimental setup for cell migration assay on silica fibers vs.on plain glass. (B/C) Probability density function (PDF) of the instantaneous migration velocities (red = directed migration velocities, blue = quasi-random migration velocities, black = all values) with corresponding mean value (black dotted line). (D/E) PDF of the cells' diffusion coefficients with corresponding mean value (black dotted line). (F/G) PDF of the LMSD alpha coefficient (red = directed states, blue = quasi-random states, black = all values) with corresponding mean value (black dotted line). (H/I) PDF of the directed state durations with corresponding mean value (black dotted line). (J/K) PDF of the quasi-random state durations with corresponding mean value (black dotted line).

The mobility of cells in quasi-random migration states is characterized by the generalized diffusion coefficient D,[123,140] displayed in Figure 21 D-E. In general, cells migrating on flat glass (Figure 21 D) exhibit lower diffusion coefficients than cells on silica fibers (Figure 21 E). The mean diffusion coefficient increases by 115 % for cells on the fiber surface. Thus, quasi-randomly migrating cells are highly motile on silica fibers. For a measure of the motility mode of cells on a substrate, the dimensionless α coefficient of the LMSD is analyzed. It is the exponent of the MSD power law fit (2) (see Materials and methods) and describes the migration mode of a cell for every time point of the cell trajectory. For α values ≈ 2, a cell performs directed migration, while $\alpha < 2$ characterizes diffusive, quasi-random motion. The α distributions (Figure 21 F-G) and the corresponding mean values are shifted to higher values on the silica fibers. Compared to the migration on plain glass, we find an increase by 12% from $\alpha = 1.45$ to $\alpha = 1.62$. Additionally, the lifetime distributions of directed and quasi-random migration states confirm this trend: on fibers, directed states are prolonged compared to on cover glass (Figure 21 H-I), with a 37% increase of the mean value from 33 s to 45 s. The distribution of the lifetimes of quasi-random states is shifted to smaller values on silica fibers (Figure 21 J-K), with the mean value decreasing from 200 s to 92 s. This result is strengthened by the significantly longer total time spent in directed migration phases on silica fibers: the portion of directed cell tracks on silica fibers (27 %) is twice larger than on cover glasses (11 %) (Table 4). This indicates a stabilization of directed migration phases and a nanotopography-triggered induction of directed migration for cells in the reorientation phase.

4.2 Direct impact of surface nanotopography on amoeboid migration

The presented results indicate a direct impact of the surface topography of the silica fibers on amoeboid cell motility. Due to biodegradation upon contact with aqueous media, nanoscaled surface features emerge at the fiber surface (Figure 19 E). On the cell level, sensing of these nanoscale features by filopodia leads to polarization with stabilized protrusions and enhanced directed migration.[46,134] When analyzing cell migration on fibers, it is important to consider the effect of surface curvature. In a study on amoeboid migration of lymphocytes Song *et al.* fabricated sinusoidal wavy surfaces with constant amplitude but different wavelengths.[141] They found an enhancement of amoeboid migration for small wavelengths but a less pronounced to no effect for higher wavelengths and flat surfaces. Transferring this curvature-dependence from this study to the fiber surfaces we investigated, none or only a very slight effect of curvature on amoeboid migration can be expected in our study. Additionally, even the most pronounced effect of surface curvature on migration velocities found by Song *et al.* was four-fold lower than the difference we found between flat glass and fiber surfaces. Thus, the migration data clearly display the differences in amoeboid migration with pronounced directed runs on nano-structured silica fibers and significantly decreased motility on the flat surface (Table 4). The mean generalized diffusion coefficient D is significantly higher on silica fibers than on plain glass substrates (Figure 21 D-E). This indicates that even cells in quasi-random migration states are more motile on the fiber surface than on plain glass. SEM micrographs of *D. discoideum* cells on the different surfaces underline these findings: more polarized, motile cells are found on the silica fibers (Figure 20 C), whereas cells on plain glass surfaces mostly lack polarization (Figure 20 B).

4.3 Migration of cells lacking myosin II

For the elucidation of the underlying mechanisms and the involved key players in cell migration, we investigate cell migration of myosin II null mutant *D. discoideum* cells in the same experimental setup. Myosin II deficient cells lack an important part of the actomyosin migration machinery that is involved in the induction of directed migration phases. In healthy cells, actin filaments at the cell rear are contracted by myosin II-mediated cross-linking, creating pushing forces by cell cortex contraction and inducing the detachment of actin foci at the surface. In myosin II deficient cells, this mechanism is suppressed, greatly impeding actin foci retraction from highly adhesive surfaces[142] and thus, cell locomotion. Previous studies have shown that myosin II-deficient cells are generally capable of creating pseudopods and to exhibit quite normal locomotion characteristics, but with reduced velocities and polarization.[143,144] This reduction in motility is believed to be due to a lack of cortical tension that hinders contraction and retraction at the trailing edge and thus pseudopod stabilization at the leading edge and translocation of the cell body.[145,146] Additionally, myosin II null mutants exhibit a clearly increased number of actin foci,[72] which might be the reason for their slow migration velocities.

In our experiments, migration of myosin II null mutant cells of *D. discoideum* on plain glass is clearly hindered compared to FreeGFP-cells. This effect is consistent throughout the whole set of migration parameters: we see a distinct decrease in the mean values of the α coefficient from 1.45 to 1.34 and decreases in the mean diffusion coefficient and the mean instantaneous velocities (Figure 22 A and Figure 23) (Table 4). In contrast, cell migration analysis of myosin II null mutant cells on the silica fibers reveals the same mean value for the α coefficient as for the FreeGFP cells (Figure 22 A). This indicates that the enhanced overall motility is conserved compared to FreeGFP cells, with distinct decreases in the other migration parameters due to the loss of

actin cortex tension and contractibility. Therefore, we can conclude that the nanoscale topography of the silica fibers induces and supports pseudopod stabilization and facilitates cell migration even in cells with greatly decreased cortical tension.

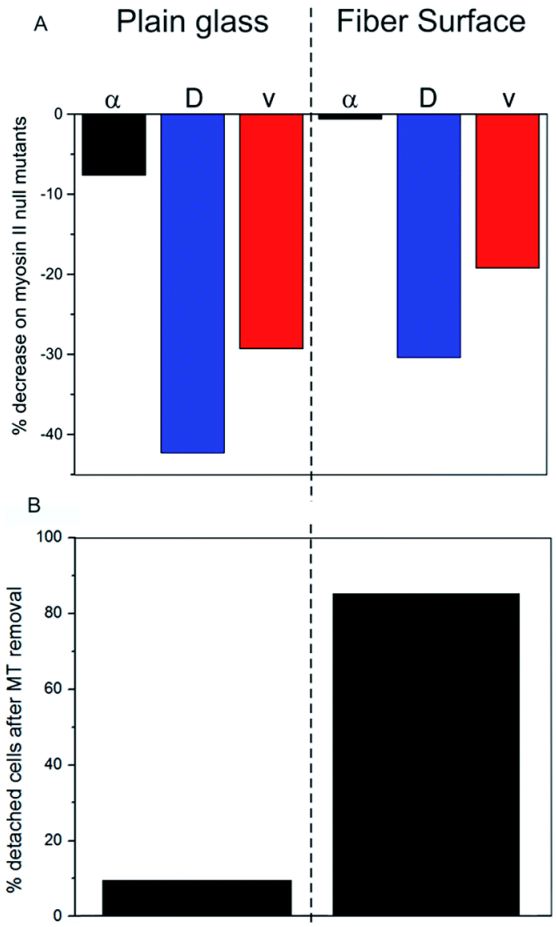

Figure 22: Comparison of the importance of cytoskeletal proteins for cell migration on the different substrates. (A) Decrease in migration parameters in cells lacking myosin II. (B) Quantification of cell detachment upon removal of microtubules.

4.4 Investigation of cells lacking microtubules

As microtubule-driven protrusion stabilization is the main migration mechanism in amoeboid cells, we investigate the behavior of *D. discoideum* cells deprived of microtubules in our experimental setup by a shaking assay. Our studies reveal that cell adhesion on silica fibers is mostly lost after treatment with benomyl, a microtubule-depolymerizing agent, while cells on plain glass are still adherent. Only 14.5 % of cells on the fibers are

adherent after benomyl treatment, in contrast to 91.0 % of the microtubule-deprived cells on flat glass (Figure 22 B). The impact of benomyl on cell adhesion is visualized in a comparison of images at $t = 0$ and $t = 15$ min after microtubule depolymerization (Figure 24): most cells have fallen off the fibers, while cells on the glass surfaces do not detach and remain in place. The process of cells sliding down from the fibers to the plain glass surface, where they adhere again.

This result points towards a migration mechanism based on actin foci as a direct functional dependency between microtubules and the actin cortex. This relation has also been found in axon growth cones: benomyl treated cells lost adhesion on microtubule deprivation due to a loss of actin foci, pointing towards an analog mechanism in mammalian cells.[147]

5. Conclusion

We investigated the influence of the intrinsically nano-patterned surface of biodegradable silica fibers on amoeboid cell migration. We found pronounced directed runs on the silica fibers compared to plain glass surfaces and further investigated underlying mechanisms. Experiments with *D. discoideum* deprived of microtubules revealed that the adhesion and migration mechanisms on silica fibers were greatly microtubule-dependent: adhesion to fibers was lost without microtubules, while microtubule-deprived cells on flat glass surfaces remained adherent. We found that the migration effect on fibers was less influenced by myosin II, as null mutant cells were as active as cells with active myosin II, while migration of cells lacking myosin II was greatly hindered on plain glass.

Our work demonstrates the importance of nanoscale surface features and scaffold structure for the motility of cells in physiological processes and thus, in the application for medical purposes. The fact that amoeboid motion is

greatly facilitated by the silica fibers used in this work opens future prospects for the use as a scaffold material in regenerative medicine. As some important cells of the innate and adaptive immune system, namely neutrophils, monocytes and some leukocytes exhibit amoeboid movement, the immune response after wounding might be greatly enhanced: a 3D silica fiber scaffold implanted into the site of injury can serve as a guiding structure, enabling immune cells to immigrate into the injury and facilitating cell movement in every spatial direction. An accelerated infiltration of immune cells could down-regulate the overall immune response which has been shown as a potential route to scarless regeneration of tissue.[41,148] Knowledge of the functional connectivities and the underlying intracellular mechanisms may lead to novel strategies for cell guidance and the manipulation of cell functions. For patients, such "smart implants" for tissue regeneration would have great benefit.

6. Appendix

6.1 Acknowledgements

D. discoideum cells were kindly provided by Dr Günter Gerisch (Max-Planck Institut für Biochemie, Martinsried). D. H. acknowledges funding from the Deutsche Forschungsgemeinschaft (grant HE5958-2-1), the Volkswagen-Foundation (grant I85100) and the Fraunhofer Attract Program.

6.2 Supporting Information

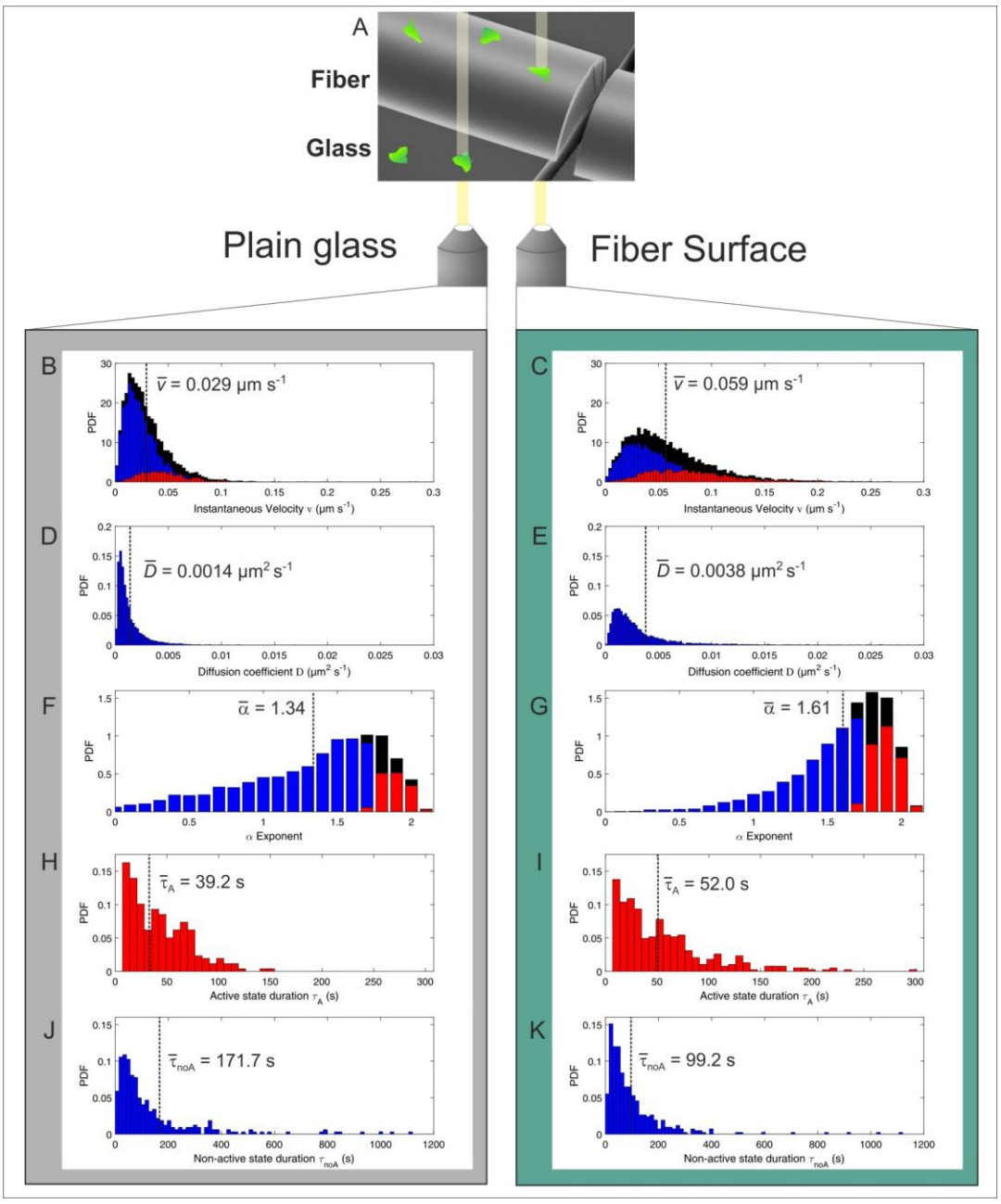

Figure 23: Cell migration analysis of *D.discoideum* myosin II null mutant cells. (A) Experimental setup for cell migration assay on silica fibers vs. on plain glass. (B/C) Probability densitiy function (PDF) of the instantaneous migration velocities (red = directed migration velocities, blue = quasi-random migration velocities, black = all values) with corresponding mean value (black dotted line). (D/E) PDF of the cells' diffusion coefficients with corresponding mean value (black dotted line). (F/ G) PDF of the LMSD alpha coefficient (red = directed states, blue = quasi-random states, black = all values) with corresponding mean value (black dotted line). (H/I) PDF of the directed state durations with corresponding mean value (black dotted line). (J/K) PDF of the quasi-random state durations with corresponding mean value (black dotted line).

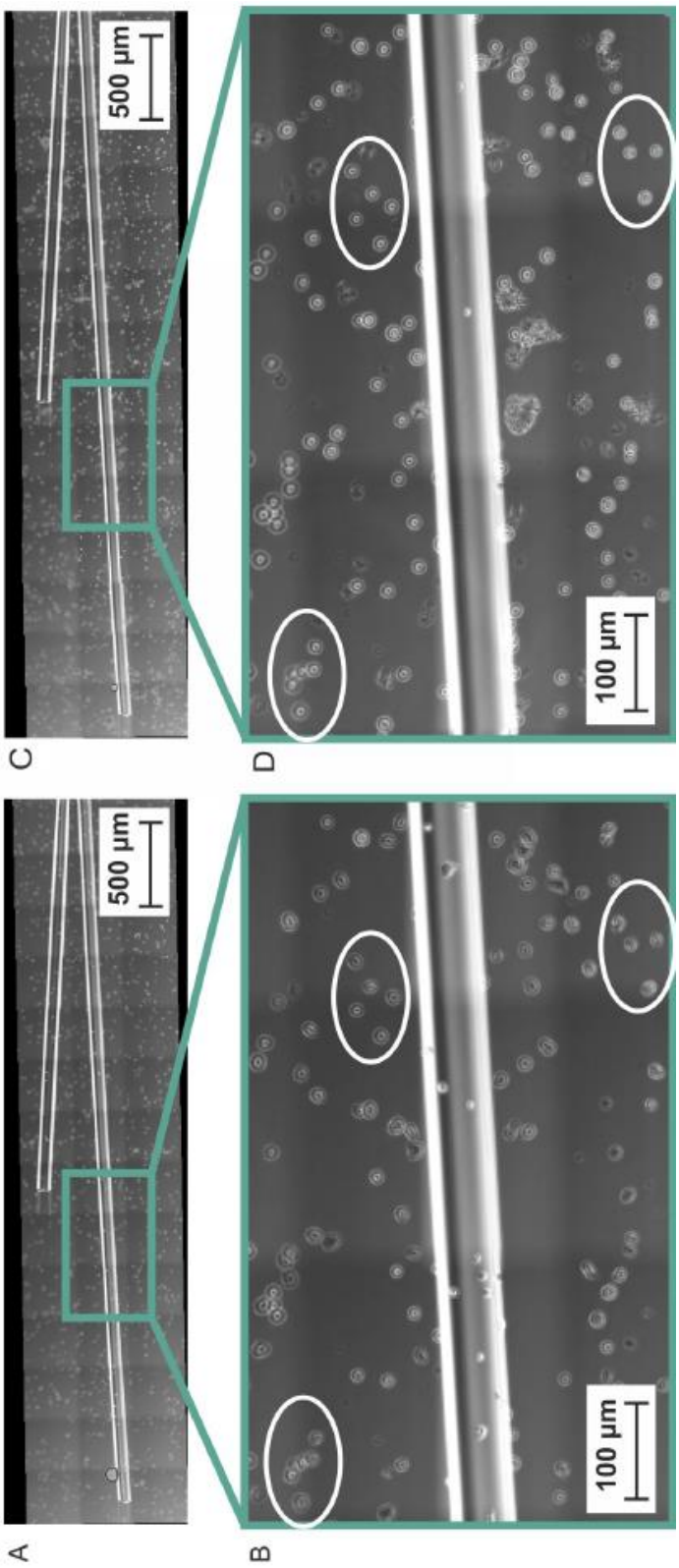

Figure 24: Comparative microscopy images of Dd cells on flat glass samples and silica fibers at the same sample positions. (A/B) Before Benomy treatment. (C/D) After Benomyl treatment, cells have detached from the fibers while they are still adherent to the flat glass.

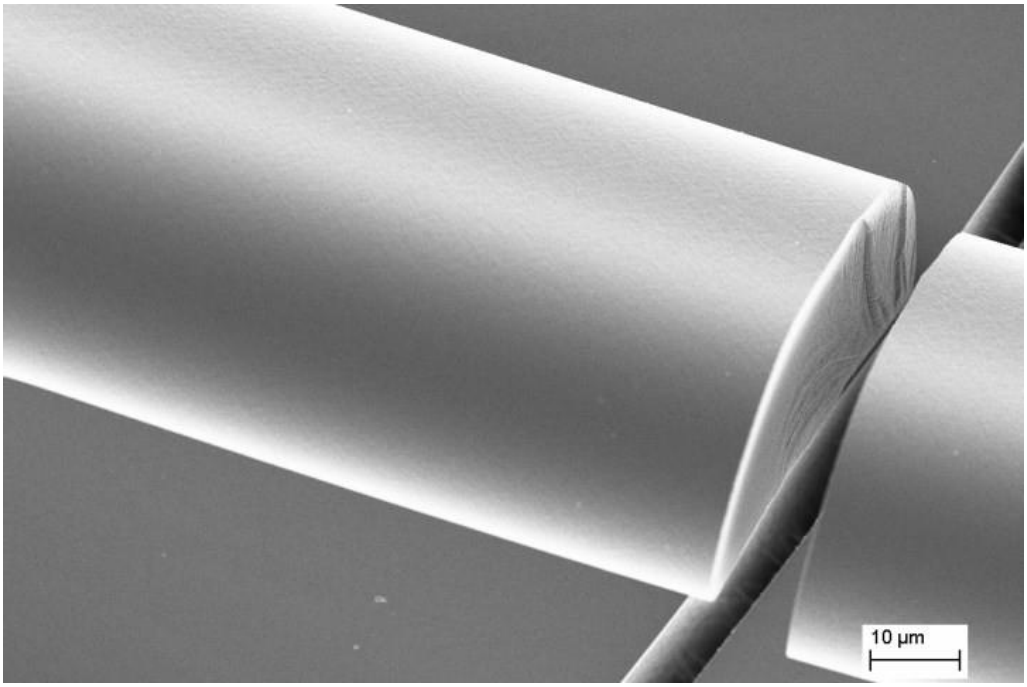

Figure 25: High-resolution SEM micrograph of silica fiber spun onto microscopy cover glass as used in the migration experiments (glass broken for visualization of fiber cross section). The surface roughness of the cover glass is observed to be smaller than that of the biodegradable fiber surface.

V. Modulation of Mammalian Cell Behavior by Nanoporous Glass

This chapter was published as

“Modulation of Mammalian Cell Behavior by Nanoporous Glass”

by Martin Emmert, Ferdinand Somorowsky, Jutta Ebert, Dominik Görick, Andreas Heyn, Moritz Wahl, Eva Rosenberger and Doris Heinrich

in Advanced Biology 5 (2021), Issue 7, 2000570.

Part of this research is part of the EU Patent EP 3561045B1 “Verfahren zur Kultivierung und Differenzierung von Zellen" and the US Patent Application #20190345443 “Method for the Culturing and Differentiation of Cells”.

Julius-Maximilians-
UNIVERSITÄT
WÜRZBURG

Fakultät für
CHEMIE UND
PHARMAZIE

Erklärung zur Autor:innenschaft

Modulation of Mammalian Cell Behavior by Nanoporous Glass
Martin Emmert, Ferdinand Somorowsky, Jutta Ebert, Dominik Görick, Andreas Heyn, Moritz Wahl, Eva Rosenberger and Doris Heinrich, Advanced Biology 5 (2021), Issue 7, 2000570

Detaillierte Darstellung der Anteile an der Veröffentlichung (in %)
Angabe Autoren:innen (ggf. Haupt- / Ko- / korrespondierende/r Autor:in) mit Vorname Nachname (Initialen)

Martin Emmert* (me), Ferdinand Somorowsky (fs), Jutta Ebert (je), Dominik Görick (dg), Andreas Heyn (ah), Moritz Wahl (mw), Eva Rosenberger (er), Doris Heinrich (dh) (* = Hauptautor:innen)

Autor:in	me	fs	je	dg	ah	mw	er	dh				∑ in Prozent
Materialherstellung	30%	55%	0%	10%	0%	0%	5%	0%				100%
Materialcharakterisierung	75%	0%	0%	5%	10%	5%	0%	5%				100%
Zellexperimente	60%	0%	15%	5%	5%	5%	5%	5%				100%
Auswertung	65%	0%	5%	2,50%	2,50%	2,50%	2,50%	20%				100%
Verfassen der Veröffentlichung	100%	0%	0%	0%	0%	0%	0%	0%				100%
Korrektur der Veröffentlichung	45%	2,50%	2,50%	2,50%	2,50%	2,50%	2,50%	40%				100%
Koordination der Veröffentlichung	50%	0%	0%	0%	0%	0%	0%	50%				100%
Summe	60,7%	8,2%	3,2%	3,6%	2,8%	2,1%	2,1%	17,1%				100%

1. Abstract

The introduction of novel bioactive materials to manipulate living cell behavior is a crucial topic for biomedical research and tissue engineering. Biomaterials or surface patterns that boost specific cell functions can enable innovative new products in cell culture and diagnostics. We investigate the influence of the intrinsically nano-patterned surface of nanoporous glass membranes on the behavior of mammalian cells. Three different cell lines and primary human mesenchymal stem cells (hMSCs) proliferate readily on nanoporous glass membranes with mean pore sizes between 10 nm and 124 nm. In both proliferation and mRNA expression experiments, L929 fibroblasts show a distinct trend towards mean pore sizes > 80 nm. For primary hMSCs, excellent proliferation is observed on all nanoporous surfaces. hMSC on samples with 17 nm pore size display increased expression of COL10, COL2A1 and SOX9, especially during the first two weeks of culture. In upside down culture, SK MEL-28 cells on nanoporous glass resist the gravitational force and proliferate well in contrast to cells on flat references. The effect of paclitaxel treatment of MDA MB 321 breast cancer cells is already visible after 48 h on nanoporous membranes and strongly pronounced in comparison to reference samples, underlining the material's potential for functional drug screening.

2. Introduction

The behavior of living cells in the complex 3D environment of tissues and organs inside the human body vastly differs from *in vitro* cell culture on simple 2D culture surfaces that are state of the art in medical products and the pharmaceutic industry. This imposes a vast need for novel surfaces that influence cellular behavior in a defined manner to trigger or support specific cell functions.[149] For example, the efficient clinical translation of promising experimental studies on stem cells is still impeded by the lack of culture substrates for their robust expansion and differentiation.[6,78,150] In drug

development, there is a great demand for functional assays with novel culture surfaces for the investigation of drug effects on different cellular functions like adhesion, migration or spreading behavior.[151] Elucidating these effects will facilitate the early identification of drug candidates for specific applications, reduce the number of substances that finally go into animal testing and clinical studies and eventually, increase the safety of the product and the benefit for the patient.

One of the most promising approaches to design such next-generation biomaterials is adding a defined surface topography or porosity in the micron- or nanometer scale.[152] Topographical features at these scales are on dimensions of subcellular structures and have been identified to be a modulator of various intracellular processes like cytoskeletal ordering, gene expression and transport mechanisms.[153–155] When being exposed to a new substrate, a cell explores the surface with actin containing protrusions of the cell membrane called filopodia, inducing mechanical interaction. In the case of positive interaction, the cell increases its contact with the new substrate by actin polymerization towards the material surface, leading to novel focal adhesions. The cell-substrate interaction can depend on the material type, the functional surface groups or proteins, or on topographic stimuli. In the growing field of topographic surface research for cell culture, various kinds of topographies are being examined, e. g. pillars, gratings, grooves, ridges or pores. For porous substrates, it has been shown that the cell-substrate interaction can be controlled by alterations of the pore size or the pore distribution. As an example, seeding hepatoblastoma cells on nanoporous alumina membranes with a pore diameter of ~ 60 nm, ~ 85 nm or ~ 200 nm results in an increase in proliferation with increasing pore diameter.[156] Fibroblasts show increased adhesion and cell proliferation on nanoporous surfaces, opening up opportunities to intentionally impede the proliferation of certain cell types. All of these examples display the potential of porous substrates as future biomaterials for cell culture and tissue engineering.

Another material group for the fabrication of porous cell culture substrates is nanoporous glass. Glass is a material class that has been routinely used in biology and biomedical research since the first days of cell culture.[157] Thus, identifying distinct effects of glassy materials on living cells might lead to applications more quickly due to shortened approval processes compared to completely novel material compositions. Glasses from the ternary glass system $Na_2O–B_2O_3–SiO_2$ show a big miscibility gap and become porous after temperature treatment and a leaching process with hot water or acid. After leaching, only the SiO_2 framework remains and constitutes the nanoporous framework of the glass with an interconnected pore system.[88] The main characteristics of the resulting glasses are a tuneable porosity, a nearly pure SiO_2 matrix leading to a high chemical and thermal stability, a narrow pore size distribution and a good accessibility of the pores. When fabricated into thin membranes, they exhibit a high optical transparency ready for microscopy in biological application. Their nano-sized porous surface structure represents a topographic 3D stimulus for living cells, resembling their natural environment of the human body. Thus, nanoporous glass meets all requirements for the use in advanced biomedical applications. A scaffold made of glass with bioactive properties could be a promising and cost-effective approach towards novel, more physiological cell culture surfaces. In this work, we investigated the suitability of nanoporous glass membranes as a novel culture surface for more realistic cell culture and in vitro assays. We seeded different murine and human cell lines on surfaces with varying nanopore sizes and analyzed their proliferation and gene expression behavior. Furthermore, we performed a functional assay probing the effect of a microtubule-targeted drug on the adhesion of breast cancer cells. In summary, we systematically investigate nanoporous glass membranes as a potential cell culture surface.

3. Materials and Methods

3.1 Membrane preparation

We produced nanoporous glass samples with two different material compositions and multiple mean pore sizes (Table 5).

Table 5: Properties of nanoporous glass samples.

Mean pore size / Sample name	Demixing Temperature	% SiO_2	% B_2O_3	% Na_2O
10 nm	500 °C	80,0	16,5	3,5
20 nm	650 °C	80,0	16,5	3,5
17 nm	585 °C	70,0	23,0	7,0
26 nm	615 °C	70,0	23,0	7,0
46 nm	645 °C	70,0	23,0	7,0
81 nm	700 °C	70,0	23,0	7,0
124 nm	730 °C	70,0	23,0	7,0

Smelting of initial components was performed at 1500 °C for 2 h. The smelted samples were slowly cooled down (10 K h^{-1}) to room temperature and cut into pieces of 16 x 16 mm before they were grinded down to a thickness of 250 µm. To achieve nanoporous glasses of different pore sizes, a second heat treatment step was performed at temperatures between 500 °C and 730 °C for 8 h (Table 1). After slowly cooling down, the samples were leached out for 2 h in distilled water at a temperature of 90 °C. After the leaching process, the hot water was exchanged in parts with 25 °C warm water. When the water in the beaker reached 60 °C, the samples were taken out of the beaker and washed in warm distilled water before they were placed in the oven over night to dry at 60 °C. This process was necessary to prevent cracks in the glass samples. All

samples were stored at room temperature. The nomenclature for this work is defined in Table 1. Borosilicate microscopy cover glass slips were used as flat glass reference (FLAT) (Menzel-Gläser, Thermo Fischer Scientific) to compare the results with a flat surface of the same material class. Tissue culture polystyrene (TCPS) was utilized as the "gold standard" control for standard cell behavior in 2D cell culture.

3.1 Membrane characterization

Membranes with 70 % SiO_2 were characterized in detail by UV-VIS transmission and SEM measurements, followed by pore size calculation. 80 % SiO_2 samples were characterized by SEM (Figure 31).

3.1.1 UV-VIS

Transmission spectra of nanoporous glass membranes with 70 % SiO_2 were recorded with a „Cary 50 UV-Vis"-spectrophotometer (Varian Inc). The wavelength range was from 180-900 nm.

3.1.2 SEM and pore size analysis

We acquired SEM micrographs of all samples. Measurements were performed with a Supra 25 Scanning Electron Microscope (Carl Zeiss Microscopy) at different magnifications and voltages. For pore size analysis, images were binarized with FIJI (ImageJ, National Institutes of Health, USA) by manual thresholding. Then, the plugin „DiameterJ" was used to determine the mean pore diameters. "DiameterJ" includes "OrientationJ", which consists of several scripts for analyzing fiber orientation and the pores inside scaffolds, e.g. the mean pore diameter used as a sample classifier in this study.

3.2 Biological Studies

3.2.1 Proliferation and qRT-PCR studies on L929

3.2.1.1 Cell Culture

Lentivirally transfected L929 mouse fibroblast cells expressing a free Green Fluorescent Protein (L929-GFP) in the cytoplasm were used for the experiments. Cell culture was performed at standard conditions. For proliferation and SEM studies, cells were kept in "Minimum Essential Medium (MEM) EBS with stable Glutamine without Phenolred" (Amimed), 10 % FCS (Bio&Shell) and 1 % PenStrep (Sigma-Aldrich). For mRNA expression experiments, cells were cultured in „Dulbecco's Modified Eagle Medium (DMEM) with GlutaMAX" (Gibco), 10 % FCS and 1 % PenStrep. Medium exchange was performed at standard rates for cell culture (every 2-3 days).

3.2.1.2 Proliferation experiments

Prior to the experiments, nanoporous glass membranes with four different mean pore sizes (17 nm, 45 nm, 81 nm, 124 nm) and FLAT glass reference samples were glued to glass sample holders for upside-down culture and autoclaved. The glasses and TCPS reference surfaces were pre-incubated with phosphate buffered saline (PBS, Sigma-Aldrich) for 15 min and culture medium for 30 min. Cells were seeded on the glass samples at a density of ~ 15.500 cells cm^{-2}. For the TCPS control, cells were seeded directly into multi-well plates at a density of ~ 4.000 cells cm^{-2}. The difference in initial seeding density was chosen to correct for the height of the sample holder / sample compound (> 50 % of total medium level) that decreases effective seeding density on the glass substrates. For microscopy, the glass samples were reversed in the well. Images were acquired at days 1-4, 7, 10 and 14. For each time point, bright field and the fluorescent images of the same ten positions were taken. The images were processed and aligned with Corel Photo-Paint X5 (Corel DRAW) prior to cell counting. Cell counting was performed manually with the "Cell Counter"

plugin of FIJI. Relative cell counts compared to day 1 were calculated. The cell doubling time T_d was calculated for each time interval. For this, the following exponential function was applied:

$$N(t) = N_0 e^{kt} \quad T_d = \frac{ln\,2}{k}$$

where N_0 is the cell count at day 1, k is the growth rate, t the time and T_d is the doubling time. For further analysis, the mean daily doubling rate per cell for each day was calculated as the inverse of the doubling times with the general assumption of exponential growth.

3.2.1.3 SEM preparation and measurements

For SEM visualization of L929-GFP cells on nanoporous glasses and reference samples, cells were seeded at a density of ~ 125.000 cells/cm^2 and cultured for 48 h. After that, the samples were rinsed three times with warm and once with ice cold PBS (Sigma-Aldrich) for one minute. Subsequently, they were placed on ice and treated with 6 % glutaraldehyde (Sigma-Aldrich) in PBS (Sigma-Aldrich) for 30 minutes. Then the samples were stored in PBS (Sigma-Aldrich) on ice for five minutes three times, medium was exchanged between steps. Afterwards, PBS was exchanged with distilled water at room temperature. Then water was replaced by acetone in five concentration steps: 15 min 30 % acetone, 20 min 50 % acetone, 30 min 75 % acetone, 45 min 90 % acetone and 5 times for 30 min 100 % acetone. Finally, acetone was exchanged with CO_2 by critical point drying in a pressure chamber at 7 °C by repeated sucking of acetone from the chamber and replacement by CO_2. This was repeated 15 times before heating the chamber up to 40 °C over the critical point of CO_2 (31 °C, 73.8 bar) to reach a final pressure of about 80 bar. Then the CO_2 was slowly released from the chamber. After that, the samples were sputtered with platinum and analyzed in a scanning electron microscope (Supra 25, Zeiss).

3.2.1.4 qRT-PCR analysis

The expression of different adhesion-related and physiologically relevant genes of L929-GFP cells in reaction to nanoporous glass membranes was analyzed using quantitative reverse transcription polymerase chain reaction (qRT-PCR). Nanoporous glass membranes with mean pore sizes 17 nm, 26 nm, 45 nm, 81 nm and 124 nm were analyzed, as well as flat reference samples (FLAT, TCPS). Pieces of the glass samples were placed in petri dishes, while for TCPS, the bottom of the petri dishes was used as culture substrate. All samples were pre-incubated with cell culture medium for 15 minutes prior to the experiments. L929-GFP cells were seeded at a density of 10.000 cells cm^{-2}. The glass samples were moved to new petri dishes the day after seeding to exclude the influence of the cells at the bottom of the original petri dishes on qRT-PCR results. After 48 h of culture, the cells were harvested and lysed directly in the petri dishes with the RNase MicroKit (Qiagen). Equivalent amounts of all samples were reverse transcribed into cDNA with the iScript cDNA Synthesis Kit (Biorad). qRT-PCR was performed in a CFX96 Real-Time PCR system (Bio-Rad) using the SsoFast EvaGreen Supermix (Bio-Rad). The primers for the experiments are listed in Table 6, ACTB was used as the housekeeping gene for normalization.

3.2.1 hMSC culture, phalloidin staining and qRT-PCR

3.2.1.1 Cell Culture

Human mesenchymal stem cells from two patients (male, 35 and female, 62) were isolated under the approval of the Local Ethics Committee of the University of Würzburg (approval number 182/10) and informed consent of the patients. Cells were cultured at standard conditions. The cell culture medium was “DMEM/F12” (Gibco) with 10 % FCS (Bio&Shell) and

1 % PenStrep (Aldrich). Medium exchange was performed at standard rates for cell culture (every 2-3 days).

Table 6: Primers for L929 qRT-PCR experiments.

Name	Sequence (5'-3')		PCR product length
	Forward primer	Reverse primer	
ACTB	*ACTGTCGAGTCGCGTCCA*	*TCATCCATGGCGAACTGGTG*	88
MKI67	*CAGAGCTAACTTGCGCTGAC*	*CGCTTGATGGTGACCAGGTG*	148
MCM2	*ACATCGAGTCCATGATCCGC*	*ACATCGAGTCCATGATCCGC*	133
FAK	*ACCAAAGAAACCTCCTCGCC*	*AGGCACAGATACCCACCTTG*	110
ITGB1	*GGACGCTGCGAAAAGATGAA*	*CCACAATTTGGCCCTGCTTG*	152
COL1A1	*GAGAGGTGAACAAGGTCCCG*	*AAACCTCTCTCGCCTCTTGC*	153
FN1	*CGACTCTGACTGGCCTTACC*	*ACCGTGTAAGGGTCAAAGCA*	166
ACTA2	*GTTCAGTGGTGCCTCTGTCA*	*ACTGGGACGACATGGAAAAG*	101

3.2.1.2 Phalloidin staining

Small pieces of nanoporous glass samples with 17 nm, 46 nm and 81 nm mean pore size and FLAT glass were autoclaved, distributed to 48-well plates and pre-incubated with PBS for 20 minutes and cell culture medium for 1 h. Additionally, TCPS petri dishes were cut into small pieces, sterilized and pre-incubated in the same way in 48-well dishes. Cells were seeded at a density of ~ 70.000 cells cm^{-2} on nanoporous glass samples and ~ 25.000 cells cm^{-2} on

references (to prohibit confluence). Cells were cultured at standard conditions until fixation on days 1, 2, 5, 7, 9, 14, 21 and 28 after seeding. For fixation and Phalloidin / DAPI staining, the samples were washed three times with PBS, then fixated for 20 minutes in 4 % Histofix™ (Carl Roth) and washed three times with PBS again. After that, the cells were permeabilized with 0.2 % Triton X-100 (Sigma-Aldrich) and washed three times with PBS again. Then, blocking was performed by incubating with 1 % BSA (Sigma-Aldrich) in PBS for 20 minutes before staining in Alexa Fluor™ 555 Phalloidin (Invitrogen) (diluted 1:40 with PBS). Samples were then mounted with Fluoromount™ with DAPI (ThermoFisher) and left to dry overnight. Imaging was performed with a Keyence fluorescence microscope.

3.2.1.3 qRT-PCR experiments

Nanoporous glass samples with mean pore sizes of 17 nm, 46 nm and 81 nm, FLAT reference glasses and TCPS were used for hMSC experiments. We took the decision to limit the number of different nanoporous glass samples to three due to limitations in the availibilty of primary human cells, in order to ensure sufficient RNA material for all samples at all timepoints. These three mean pore sizes were the logical choice, being not too far apart and still representing three distinctly different regimes of mean pore sizes. Samples were placed into 12-well plates and cells were seeded with a densitiy of ~ 85.000 cells cm^{-2} (nanoporous glass samples) and ~ 30.000 cells cm^{-2} (references). The glass samples were moved to new well plates the day after seeding to exclude the influence of the cells at the bottom of the original wells on qRT-PCR results. At timepoints 7 d, 12 d, 21 d and 28 d of culture, cells were harvested and lysed directly in the wells. For subsequent analysis, samples from day 7 and day 12 were pooled due to limitations in cells available for initial seeding. All further steps were performed as described in 2.3.1. The primers for the experiments are listed in Table 7, GAPDH was used as the housekeeping gene for normalization.

Table 7: Primers for hMSC qRT-PCR experiments.

Name	Sequence (5'-3')		PCR product length
	Forward primer	Reverse primer	
GAPDH	TGACGCTGGGGCTGGCATTG	GCTCTTGCTGGGGCTGGTGG	154
Col2a1	CGGCTTCCACACATCCTTAT	CTGTCCTTCGGTGTCAGGG	92
Col10	ACAGGCATAAAAGGCCCACT	GCACACCTGGTTTCCCTACA	247
Sox 9	GCTCAGCAAGACGCTGGGCA	TCCGTGGCCTCCTCTGCCTC	180

3.2.2 Short-term adhesion and proliferation studies of SK-MEL-28

3.2.2.1 Cell Culture

SK-MEL-28 with lentivirally transfected GFP were cultured under standard conditions in "Dulbecco's Modified Eagle Medium (DMEM) with GlutaMAX™" (Life Technologies), with 10 % fetal calf serum (FCS) (Bio&Shell) and 1 % Penicillin Streptomycin (PenStrep) (Sigma-Aldrich). The cells were kindly gifted by Sebastian Kress (Fraunhofer ISC, Würzburg). Before fluorescence microscopy experiments, the medium was switched to "Minimum Essential Medium (MEM) EBS with stable Glutamine without Phenolred" (Amimed), 10 % FCS and 1 % PenStrep. Medium exchange was performed at standard rates for cell culture (every 2-3 days).

3.2.2.2 Adhesion experiments

Prior to the experiments, the glass samples were autoclaved. Cells were trypsinized, counted and suspended to ~ 50.000 cells mL^{-1}. 10 µL drops of this suspension containing ~ 500 cells were applied onto nanoporous glass samples

with a mean pore size of 10 nm, 20 nm and FLAT reference glass samples. After 3 h incubation in upright culture to allow the cells to adhere to the surfaces under the drops, the samples were put upside-down into "µ-Dishes 50 mm" (ibidi GmbH) containing cell culture medium and spacers to prevent the sample surface from touching the bottom of the dish. After flipping, samples were incubated overnight. Image acquisition (brightfield and fluorescence) was performed on days 1, 2, 3 and 4 after seeding. A stage top incubator (Tokai Hit) was used to ensure optimal conditions for living cells during imaging. After imaging at day 4, the samples were stored in the incubator until day 9. Then, samples were embedded in a solution of Mowiol (Sigma) and DAPI (D 8417, Sigma) and covered with a coverslip. They were imaged in a fluorescence microscope (Keyence) with a DAPI excitation filter. Automatic cell counting of all images was performed with the "Spot Detection" feature of NIS-Elements Software (Nikon). The mean error of the automatic detection of cells was determined by manual cell counting of three samples on different days with the "Cell Counter" plugin in FIJI. Relative cell counts normalized to day 1 cell counts were calculated as ratio of cell count at current day to cell count at day 1 (i.e. a relative cell count of 1.5 at day x equals to 50 % increase in cell numbers relative to day 1). Furthermore, the mean value for the different samples were determined.

3.2.2.3 SEM Preparation and Morphological Analysis

For SEM visualization of SK-MEL-28 cells on nanoporous glasses and FLAT reference samples, 50 µL droplets containing ~ 625 cells were placed onto all samples and incubated for 4 h. Then, full culture medium was added to the dishes and samples were incubated for 12 h. After that, the samples were rinsed three times with warm and once with ice cold PBS (Sigma-Aldrich) for one minute. Subsequently, they were placed on ice and treated with 6 % glutaraldehyde (Sigma-Aldrich) in PBS (Sigma-Aldrich) for 30 minutes. Then the samples were stored in PBS (Sigma-Aldrich) on ice for five minutes three

times, medium was exchanged between steps. Afterwards, PBS was exchanged with distilled water at room temperature. Then water was replaced by acetone in five concentration steps: 15 min 30 % acetone, 20 min 50 % acetone, 30 min 75 % acetone, 45 min 90 % acetone and 5 times for 30 min 100 % acetone. Finally, acetone was exchanged with CO_2 by critical point drying in a pressure chamber at 7 °C by repeated sucking of acetone from the chamber and replacement by CO_2. This was repeated 15 times before heating the chamber up to 40 °C over the critical point of CO_2 (31 °C, 73.8 bar) to reach a final pressure of about 80 bar. Then the CO_2 was slowly released from the chamber. After that, the samples were sputtered with platinum and analyzed in a scanning electron microscope (Supra 25, Zeiss). For morphological analysis, SEM micrographs of the cells on the different culture surfaces were used. Prior to analysis, the image magnification was normalized, single cells were cropped by hand in a detailed process and images were binarized. Cell morphology was then analyzed using the "Analyze Particle" tool in FIJI.

3.2.3 Proliferation Studies on MDA-MB-231 Upon Paclitaxel Treatment

3.2.3.1 Cell Culture

MDA-MB-231 cells were cultured at standard conditions. The cell culture medium was "RPMI 1640 modified with GlutaMAX" (Gibco) with 10 % FCS (Bio&Shell). Medium exchange was performed at standard rates for cell culture (every 2-3 days).

3.2.3.2 Paclitaxel Treatment Experiments

Nanoporous glass samples with mean pore sizes of 17 nm, 26 nm, 46 nm, 81 nm and 124 nm and FLAT reference glasses were glued to glass sample holders for upside-down culture and autoclaved. Before cell seeding, the samples were pre-incubated for 15 min with PBS (Sigma-Aldrich) and for 30 min with cell

culture medium. The glass samples were seeded at a density of ~ 30.000 cells cm^{-2} and incubated in an upright position for 24 h to enable complete adhesion of cells on all samples. Before the imaging was started, paclitaxel (LC Laboratories) was thawed and diluted in dimethyl sulfoxide (DMSO) (Sigma-Aldrich) and culture medium to a stock concentration 1 µM paclitaxel. For the long-term microscopy experiments, the samples were flipped into "µ-Dishes 50 mm" (ibidi GmbH) containing 1.5 mL of pre-warmed culture medium (upside-down culture). Then, 1.5 mL of additional cell culture medium was added to the samples in the "Control" group. For the "Treatment" group, 1.5 mL of the paclitaxel stock was added, giving a final paclitaxel concentration of 500 nM. After 3 h of incubation, the samples were placed in an incubation chamber (Tokai Hit) mounted on a florescence microscope (ECLIPSE Ti, Nikon), where they were kept for the duration of the experiment. For each sample, images of 12 positions were taken at time points 0 h, 24 h and 48 h. For each timepoint and position, cells were counted manually and relative cell counts normalized to day 1 cell counts were calculated as ratio of cell count at current day to cell count at day 1 (i.e. a relative cell count of 1.5 at day x equals to 50 % increase in cell numbers relative to day 1). Furthermore, the mean value for the different samples were determined.

4. Results

4.1 Physical properties of nanoporous glass membranes with different pore sizes

To probe the influence of nanoporous glass on living cell behavior and to derive pore-size dependencies, we prepared membranes of different mean pore sizes. For a systematic investigation on the influence of nanoporous glass membranes' pore sizes on living cells, we optimized the leaching and cooling process: We were able to fabricate reproducible, stable membranes of 16 x 16 x 0.25 mm in batches of up to 90 membranes per leaching step. The membranes could be readily autoclaved prior to cell culture. With increasing demixing temperature, the membranes become more opaque, indicating an increase in the pore size (Figure 26a). This macroscopic observation is confirmed in SEM measurements of the nanoporous glass surfaces, displaying a significant increase in the nanopore sizes with increasing demixing temperatures. The overall pore structure is conserved (Figure 26b). The pore size analysis of the porous nanoporous glass samples was performed on binarized and segmented SEM micrographs. We were able to robustly prepare nanoporous glass membranes with mean pore sizes between 17 and 124 nm and a mean thickness of only 250 µm (Figure 26c). As visible in the SEM micrographs, the overall pore structure is highly anisotropic, which is where the large deviations in the measurement of mean pore sizes originate from. The UV/VIS transmission spectra clearly display a broadening of the absorbed wavelength range with increasing mean pore sizes (Figure 26d). The characterization results display the expected trend: The nanoporous glass samples show an increasing pore size with higher demixing temperature. For 80 % SiO_2 samples, two demixing temperatures were applied, yielding nanoporous glass membranes with mean pore sizes of 10 nm and 20 nm (Figure 31).

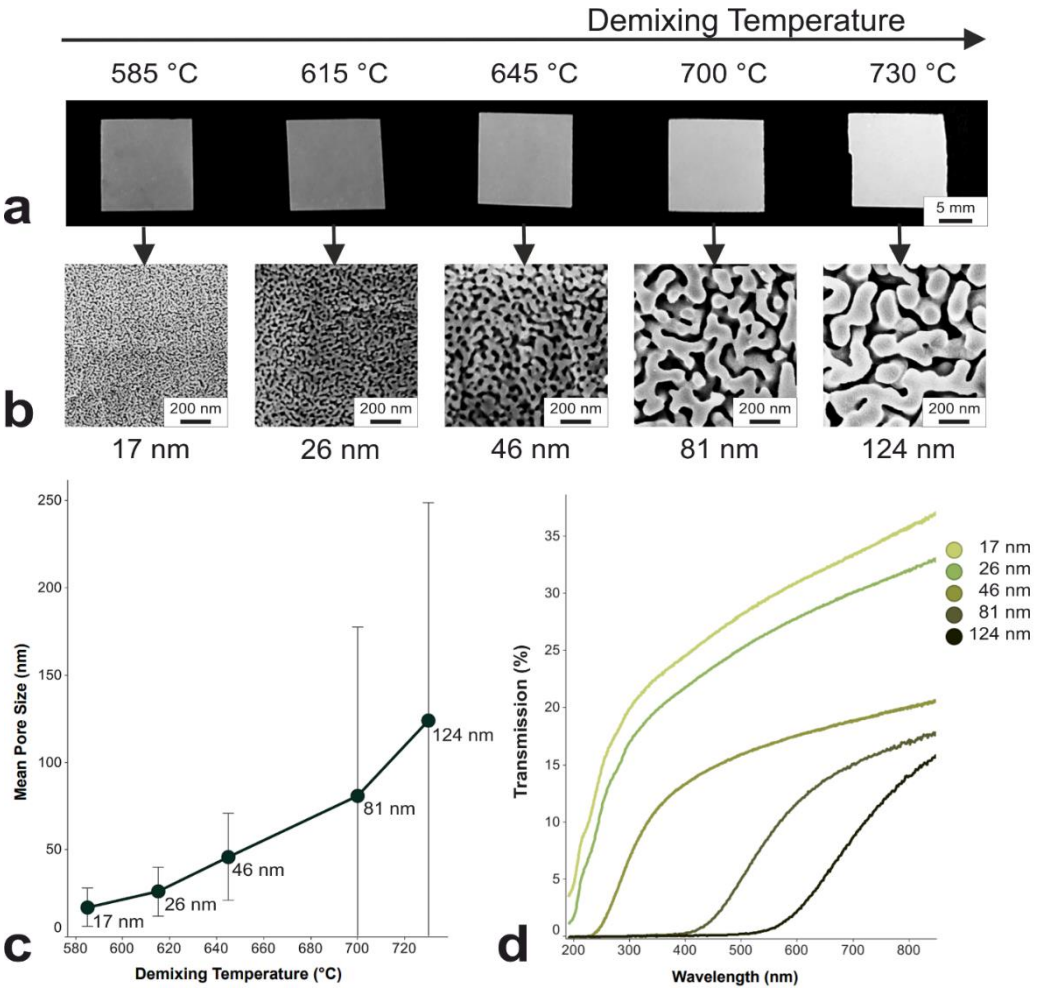

Figure 26: Characterization of nanoporous glass samples with 70 % SiO_2 and different demixing temperatures. a) Photographies for macroscopic evaluation of samples treated at demixining temperatures 585 °C, 615 °C, 645 °C, 700 °C and 730 °C. b) SEM micrographs of the nanoporous glass membranes from a). c) Mean pore sizes of samples treated at demixining temperatures 585 °C, 615 °C, 645 °C, 700 °C and 730 °C as calculated by DiameterJ with standard deviations (high deviations caused by anisotropic pore structure). d) UV-VIS transmission spectra of samples with mean pore sizes 17 nm, 26 nm, 46 nm, 81 nm and 124 nm.

4.2 L929 mouse fibroblast proliferation on nanoporous glasses is pore size dependent

To elucidate cell behavior on nanoporous glass membranes, we analyzed the proliferation of L929 cells under standard cell culture conditions. For this purpose, cells were seeded onto nanoporous glass membranes with four different mean pore sizes (17 nm, 45 nm, 81 nm, 124 nm) and two flat reference surfaces (FLAT / TCPS). Microscopy and cell counting was performed for days 1, 2, 3, 4, 6, 7 and 10 after cell seeding (Figure 27a). On TCPS, proliferation started immediately, with a daily doubling rate of following days, cells on TCPS displayed the expected exponential proliferation behavior known from standard cell culture. Cell counting on TCPS had to be stopped at day 7 to ensure reliable cell counting results, which was not possible on the fully overgrown substrates. Cell proliferation on all of the glass samples, including FLAT, exhibited an initial proliferation delay during the first days of culture. While cells on the FLAT reference started to slightly proliferate after two days of culture, there was a delay in proliferation or a slight decrease in cell number on most nanoporous glass samples until day 4, indicated by negative cell doubling rates displaying a small degree of apoptosis. After this initial delay, cells started to proliferate steadily on the nanoporous glass samples with a clearly positive trend towards mean pore sizes above 80 nm, almost reaching the cell doubling rates of the reference samples (Figure 27b).

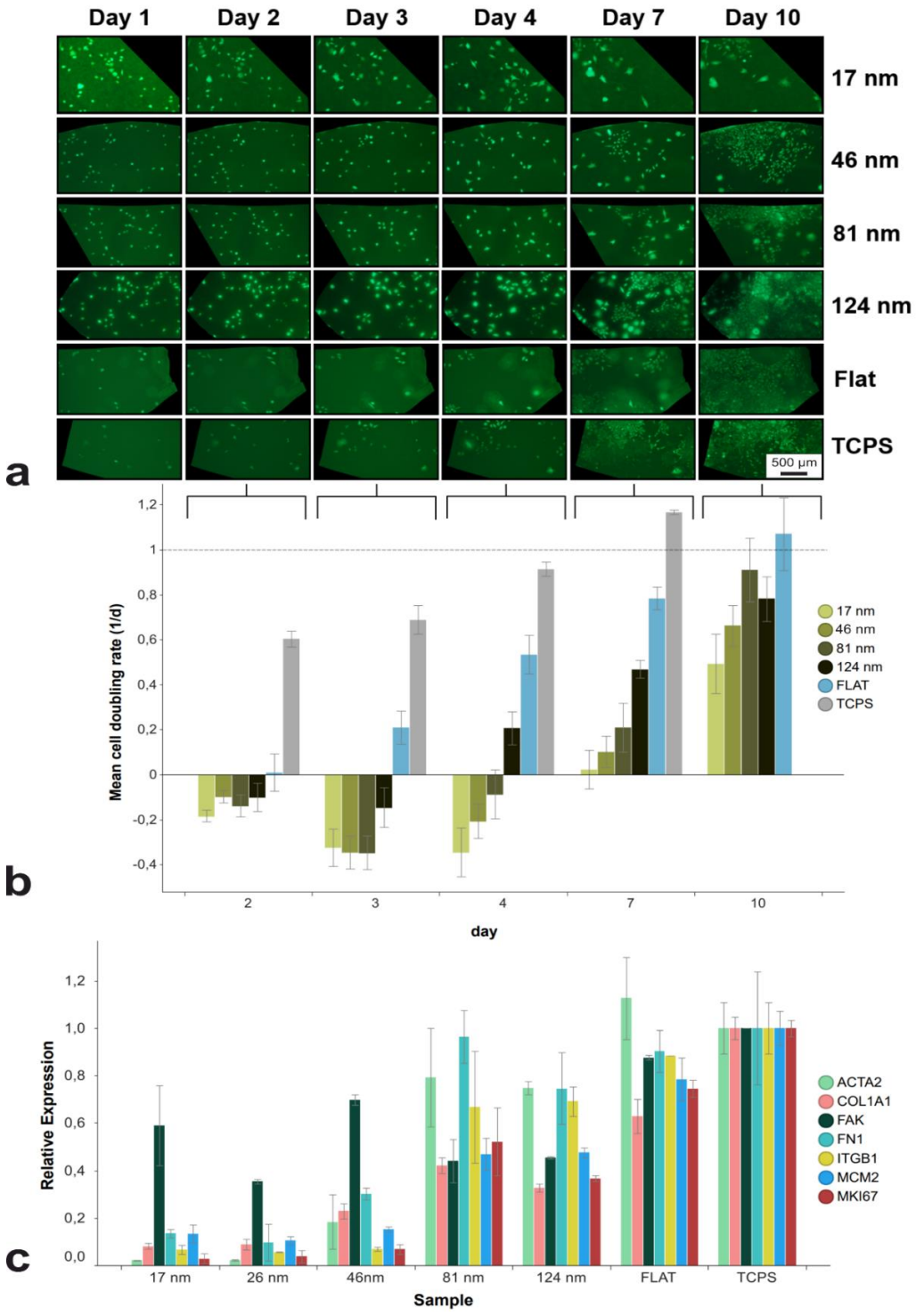

Figure 27: Analysis of the interaction of L929 mouse fibroblasts with nanoporous glass samples of different pore sizes (17 nm, 26 nm, 46 nm, 81 nm and 124 nm), compared to flat references (FLAT glass and TCPS). a) Exemplary fluorescence microscopy image series of one (out of 10 total) sites of analysis at different timepoints from day 1 to 10. Images show L929 GFP cells (green) on different substrates at different timepoints. b) Mean cell doubling rates for each timepoint at days 2, 3, 4, 7, and 10; brackets to connect the bar graphs with the corresponding image columns from a) . Cell doubling rates were calculated via an exponential function with mean cell counts at day 1 as reference points. c) Relative mRNA expression after 48 h culture on the different pore size samples and FLAT glass, normed to TCPS expression.

4.3 Differential mRNA expression on different pore sizes – Elucidation of a cut-off pore size for attractive interaction

mRNA expression of L929 cells seeded on nanoporous glass membranes with mean pore sizes of 17 nm, 26 nm, 45 nm, 81 nm and 124 nm and the two reference samples was analyzed by qRT-PCR after 48 h of culture – i.e. during the initial resting phase when the cells settle on the surface and explore their surroundings. Cells seeded on nanoporous glass membranes with mean pore sizes of 81 nm and 124 nm show an expression profile that is very similar to the FLAT reference that already started proliferating at this timepoint (Figure 27c). Even though the relative cell count is still slightly decreasing during the first days of culture, the induction of proliferation for cells on the 81 nm and 124 nm samples is significantly increased compared to smaller pore sizes. This is visible in the increased expression of the proliferation-specific proteins (MKI67, MCM2). These findings indicate a more attractive initial cell-substrate interaction compared to smaller pore samples, even though overall proliferation has not started yet after 48 h. In addition, genes that regulate other standard cell functions such as adhesion (FAK, ITGB1), matrix production (COL1A1, FN1) and contraction (ACTA2) were analyzed. The expression of ACTA2 on nanoporous glass membranes with larger nanopores is slightly reduced in comparison to the FLAT samples. Below 80 nm pore size, a drastic change in expression can be observed as there is a clear upregulation of FAK, while the other essential genes are dramatically downregulated, indicating reduced mean cell vitality.

4.4 Primary hMSCs proliferate readily on nanoporous glasses with different pore sizes

Primary hMSCs were seeded onto nanoporous glasses of three different mean pore sizes (17 nm, 46 nm, 81 nm) and two flat reference samples (FLAT glass / TCPS). Samples were fixated and stained with phalloidin at different timepoints. All samples exhibited good cell adhesion and proliferation, proven by increasing cell density and confluent cell sheets visible by eye. During the first days of culture on the nanoporous glass membranes, cell clustering was observed (Figure 28a). No more clusters were present after day 3, indicating thorough cell spreading.

4.5 Chondrogenic differentiation is induced on glasses with 17 nm mean pore size – Distinct differences in cytoskeletal ordering

mRNA expression analysis was performed to identify any differentiation inducing effects of the nanoporous glass samples on primary hMSCs. For this purpose, mRNA was extracted at different timepoints, converted to cDNA and then analyzed by qPCR. For the sample with 17 nm pore size, we found distinct upregulations for some chondrogenic factors. In comparison to the controls, a clear increase in the cartilage-specific genes SOX9, COL2A1 and COL10 can be observed compared to FLAT and TCPS (Figure 28b and c). Phalloidin stainings of the hMSC actin cytoskeleton at different timepoints display that actin fiber alignment is much more pronounced on the 2D reference surfaces, while the actin cytoskeleton is rather disordered on the nanoporous glass samples (Figure 32).

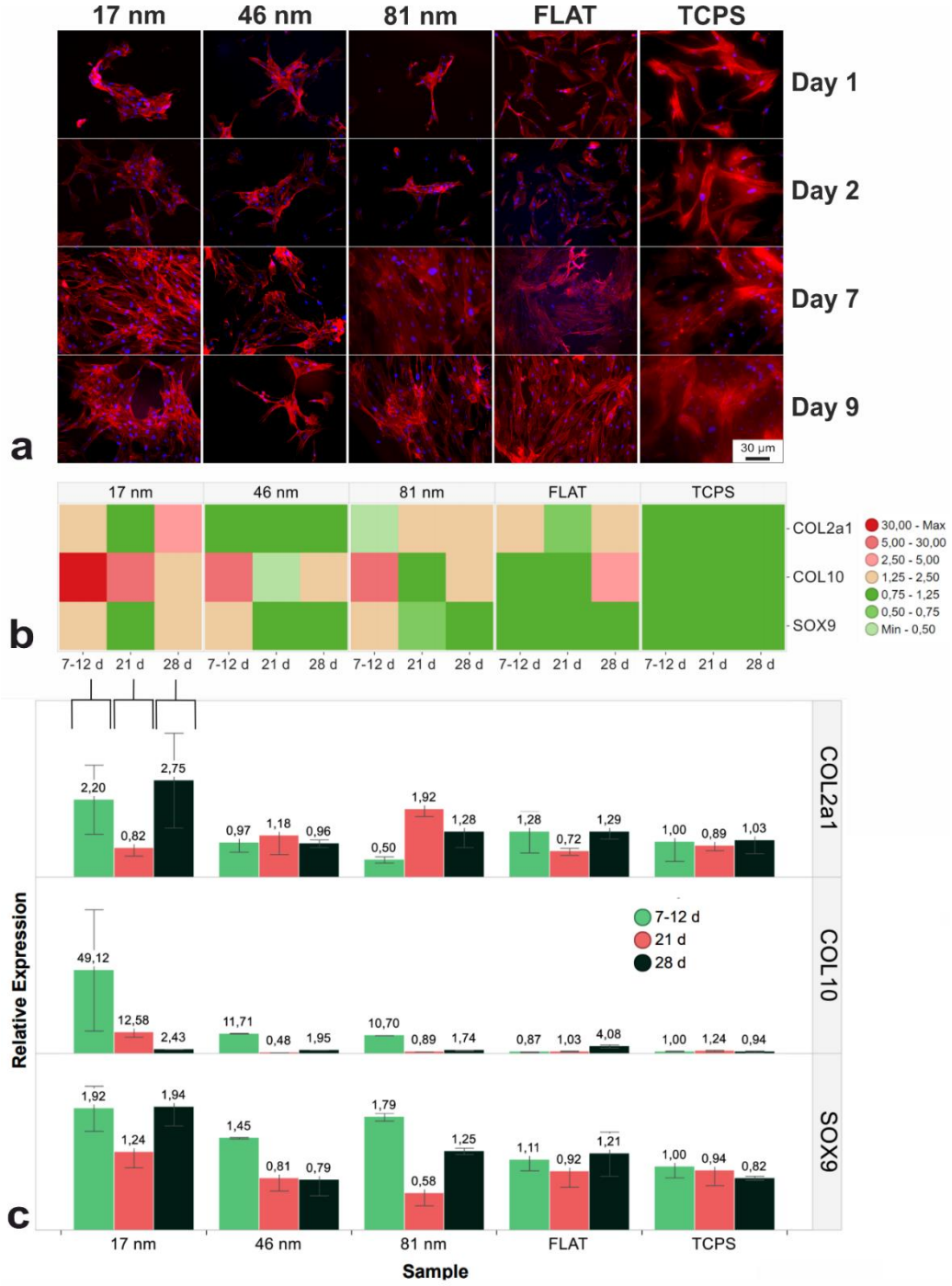

Figure 28: Analysis of the interaction of primary human mesenchymal stem cells (hMSCs) with nanoporous glass samples of different pore sizes (17 nm, 46 nm and 81 nm) and flat references (FLAT glass and TCPS). a) Microscopy images of hMSC at different timepoints with actin cytoskeleton stained by phalloidin and DAPI stained nuclei. b) Heatmap of mRNA expression of chondrogenic biomarkers at different timepoints (7-12 d, 21 d and 28 d). c) Relative mRNA expression of chondrogenic markers at different timepoints (7-12 d, 21 d and 28 d), normed to the expression at the first timepoint on TCPS for each marker.

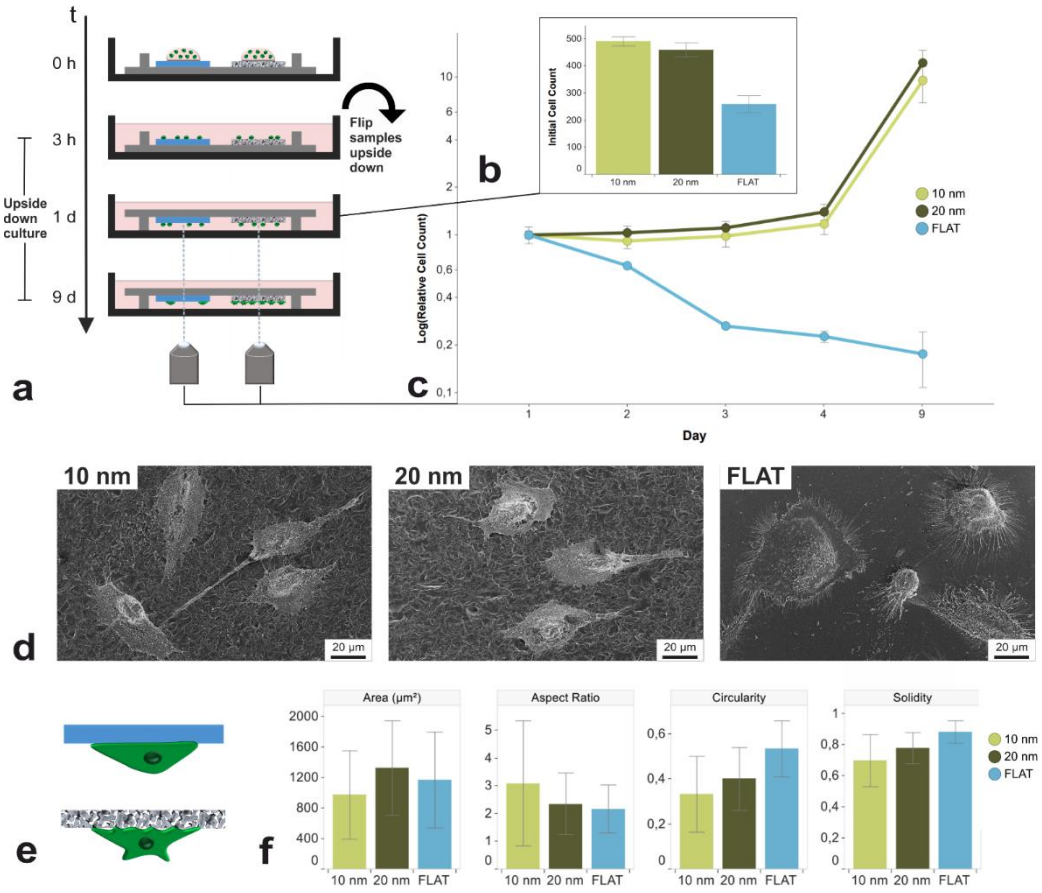

Figure 29: Proliferation experiments of SK-MEL-28 on nanoporous glass samples of different pore sizes (10 nm and 20 nm) and FLAT glass references in upside down culture. a) Schematic illustration of cell seeding and culture. b) Initial cell counts after 3 h adhesion time and subsequent overnight upside down culture. c) Relative cell counts at days 1, 2, 3, 4 and 9 (logarithmic scale on the y axis). d) SEM micrographs of cells on different samples (10 nm and 20 nm mean pore size and FLAT) after 48 h of overhead culture. e) Schematic illustration of morphology on different samples (blue = FLAT, grey = nanoporous glass membrane). f) Mean morphological parameters on different samples, calculated from cropped and binarized cells from SEM micrographs.

4.6 Resisting Gravity: Short-term adhesion and proliferation studies of SK-MEL-28 reveal increased adhesion and cell spreading on nanoporous glass

For the investigation of general cell adhesion and viability on nanoporous glass membranes in upside down culture, we used nanoporous glass membranes with mean pore sizes of 10 nm and 20 nm with 80 % SiO_2. 10 µL droplets of a cell suspension containing ~ 500 SK-MEL-28 melanoma cells were pipetted onto the nanoporous glass membranes and FLAT reference glasses. After 3 h of incubation to allow for slight adhesion, the samples were turned upside-down and cells were incubated under the influence of gravity, putting cell adhesion to the test. Microscopy and cell counting was performed for days 1, 2, 3, 4 and 9 after seeding (Figure 29a). Strikingly, the initial adhesion of SK-MEL-28 cells is significantly increased on nanoporous glass, with 490 ± 18 cells (10 nm) and 459 ± 27 cells (20 nm) versus 259 ± 32 cells on FLAT after 3 h adhesion time (Figure 29b). After the typical resting phase upon seeding on uncoated or non-TCPS surfaces, the cells on nanoporous glass membranes proliferated very strongly even under the influence of gravity, growing to a mean relative cell count of 11.3 ± 2.0 on day 9 after seeding. In contrast, the number of cells on smooth glass surfaces steadily decreased to a mean relative cell count of 0.17 ± 0.05 (Figure 29c). Additional morphological investigations carried out with binarized cell outlines from SEM micrographs (Figure 29d) revealed a significantly higher circularity and solidity for the cells on FLAT surfaces. This indicates a rather passive spreading process with a more circular morphology and less protrusions. Cells on nanoporous samples had more protrusions and an increased area, indicating an active spreading process with strong focal adhesions, clamping the cell body to the topographic surface under the influence of gravity in upside down culture.

4.7 Giving in to Gravity: Deadhesion of MDA-MB-231 Breast Cancer Cells upon Paclitaxel Treatment

To further study the effect of differential cellular adhesion to nanoporous glass compared to the FLAT reference, the effect of a cytoskeleton-altering chemotherapeutic agent on MDA MB 231 breast cancer was investigated. Cells were seeded onto nanoporous glass membranes with different mean pore sizes (17 nm, 26 nm, 46 nm, 81 nm, 124 nm) and onto FLAT samples and were incubated for 24 h in order to achieve homogeneous cell colonization of all substrates. The samples were then cultured upside down (as previously described) for 48 h and divided in two groups: “Control” and “Paclitaxel”. The “Control” samples were cultured in normal culture medium, the “Paclitaxel” group was cultured with 500 nM paclitaxel in the culture medium. Paclitaxel blocks the dynamics of microtubules essential for maintaining focal adhesions. 24 h into the experiment, all cells on “Control” samples are proliferating, except on the 17 nm sample. After 48 h of culture, proliferation has continued on the FLAT and 124 nm sample, while cell numbers only slightly increased on the other samples. In the “Paclitaxel” group, no distinct differences between samples can be observed after 24 h. After 48 h the relative cell count on all nanoporous samples decreases by ~ 35-55 %. The influence on the FLAT substrate is significantly lower, with a drop of ~ 5 % during the first 48 h (Figure 30).

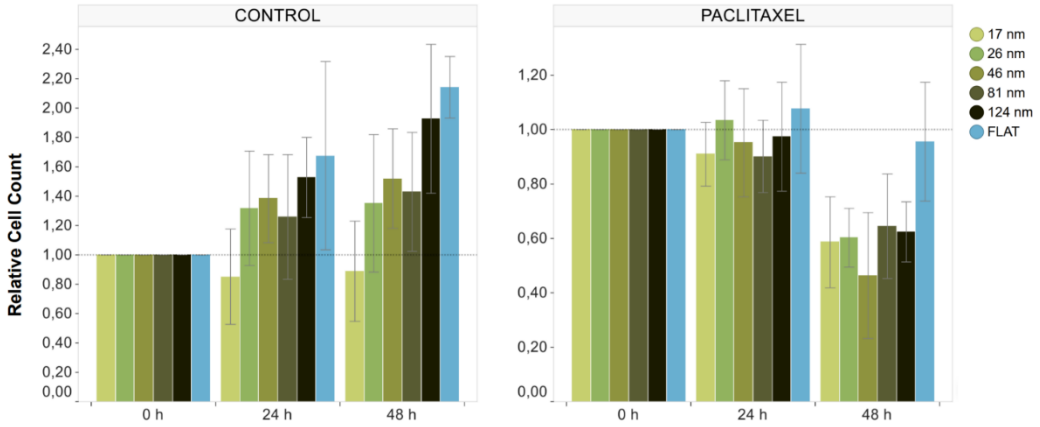

Figure 30: Proliferation experiments of MDA-MB-231 cells on nanoporous glass samples of different pore sizes (17 nm, 26 nm, 46 nm, 81 nm and 124 nm) and FLAT glass references in upside down culture. Left side: Relative cell counts in control experiment (CONTROL). Right side: Relative cell counts under the influence of 500 nM Paclitaxel (PACLITAXEL).

5. Discussion

For a systematic study of the pore size of nanoporous glass on cell behavior, glass membranes of different mean pore sizes were produced and characterized in order to test their applicability as a novel nanostructured topographic cell culture substrate. A membrane thickness of 250 µm was found suitable for robust handling, while thinner samples were more likely to break during the preparation process and in the lab. In comparison to thicker samples, 250 µm samples provided a sufficient optical transparency for basic microscopy tasks even for the macroscopically opaque samples. This opaqueness is caused by the typical coarsening and phase separation occurring during spinodal decomposition of such glass systems[88]. Opacity increased with the demixing temperatures, pointing towards increasing nanopore sizes. The UV/VIS measurements confirmed this assumption with decreased transmission for increasing demixing temperatures - the pores in the system act as a scatterer. This is in good accordance to the Mie-scattering theory, where the in-line transmission decreases at a defined wavelength, if the size of the scatterer increases. The cut-off wavelength for transmission increases with increasing size of the scatterer, i.e. with increasing mean pore sizes[158,159].

We then investigated the interaction of living cells with nanoporous glass membranes by analyzing the proliferation of L929 mouse fibroblast cells, the standard cell line used for biocompatibility testing of novel materials. We used samples with four different mean pore sizes (17 nm, 45 nm, 81 nm, 124 nm) under standard cell culture conditions, and FLAT glass samples and TCPS as controls. As the "gold standard" commercial product for cell behavior studies, TCPS surfaces are optimized for immediate protein adsorption by surface treatment, facilitating initial cell adhesion and proliferation[160]. The TCPS samples exhibited the expected exponential cell proliferation known from conventional cell culture. On the FLAT glass reference, cell proliferation starts after the second day. Compared to TCPS, proliferation is significantly reduced on FLAT, due to the fact that protein adsorption is signifiacntly decreased on non-treated glass[161]. While proteins from the culture medium can still form a uniform, but less dense layer on the FLAT samples, the protein layer adsorbed at the adhesion surface of the nanoporous samples is interrupted by the pores. Thus, surface protein density at the nanoscale is radically reduced, inhibiting cell spreading and cell proferation during the first days of culture. After this initial delay, the proliferation rate constantly increases to near-exponential rates for cells on mean pore sizes $>$ 80 nm until confluence. As fibroblasts are matrix-producing cells that can modify their environment[162], this effect can be ascribed to ongoing matrix secretion by the cells, remodeling the adhesion surface bit by bit – in our study, depending on the pore size of the substrate. In general, larger nanopore sizes ($>$ 80 nm) show a positive influence on cell proliferation, as displayed in the larger increase of the relative cell numbers on nanoporous glass membranes with pore sizes of 124 nm and 81 nm. This clear trend points towards a systematic mechanism for L929 fibroblast adhesion and proliferation on nanoporous glass, indicating a proliferation mechanism and – rate that is closer to the in vivo situation than on flat substrates[151]. It is widely known that cells can perceive the nanoroughness of a surface and that mechanical and topographical properties influence the adhesion and migration

behavior of cells. Cells probe surface features with mechanosensitive elements consisting of actin, myosin, paxillin or filopodia[55,163]. In fact, cell proliferation can be strongly influenced by the (nano)structure of a cell's direct vicinity and the substrate topography[164,165]. Cell proliferation in a lot of cell types is diminished on surfaces exhibiting nanotopographical stimuli[163,166–168]. For example, corneal epithelial cells cultured on nanogrooves mimicking the diameter of collagen fibrils in the corneal stroma exhibited reduced proliferation[163]. Altering the nanoscale roughness by just a few nanometers can have a distinct influence on cell proliferation, highlighting living cells' sensitivity to topographic cues that are one million times smaller than their diameter[169,170]. Milner et al. demonstrated the influence of nanoarchitecture by investigating the proliferation of human fibroblasts on PLLA substrates with randomized nanoscale bumps or nanoislands: The cultures maintained significantly lower densities and lower rates of proliferation on patterns with features > 200 nm. Continued reduction of feature sizes eliminated the discrepancy between nanotextured and flat substrates with respect to cell proliferation[171]. A cut-off size for cell proliferation was also found for human HepG2 cells seeded on nanoporous aluminum surfaces with pore sizes of 40 nm and 270 nm: On the larger pores, cell adhesion and proliferation was much better than on the smaller pores[172]. Two studies on surfaces modified with gold nanodot patterns of different nano-spacings showed results on the integrin clustering at the surface: There is a distinct turnover of adhesion strengths for fibroblasts in the range between 50 and 70 nm for these surfaces[173]. With spacings < 70 nm, the adhesion is highly increased, even for very short adhesion times < 10 min[174]. These results point to a cell-type specific influence of nanoscale topographies on cellular adhesion and proliferation behavior. In agreement to that, our study showed that there is a cut-off size for the proliferation of L929 fibroblast cells on nanoporous glass that could also be fostered for cell cultures that need diminished proliferation rates, e.g. to better reflect *in vivo* proliferation rates in long-term experiments[150,175].

The immediate influence of nanoporous glass on L929 fibroblast cell functions was further investigated in real time PCR experiments. The mRNA expression patterns of L929 cells after 48 h of culture on all samples further elucidate the underlying mechanism of the initial cell reaction to the different substrates. After two days on the respective culture surfaces, two different main types of expression profiles on the nanoporous samples could be distinguished: The mRNA profiles on the three small (17 nm / 26 nm / 46 nm) and on the two larger nanopore samples (81 nm / 124 nm) each show a similar pattern. This indicates a transition of cell behavior for adhesion on smaller versus larger nanopores. On smaller nanopores, the expression of most proteins that play crucial roles in healthy cells was strongly down-regulated after 48 h of culture. This is in good accordance with the trends observed in the L929 proliferation experiments. Additionally, the resemblance of the expression patterns of the larger nanopore samples and the FLAT sample is striking, proving the general cell reaction to the material glass. Taking a closer look at the mRNA expression, the decreased expression of KI67 and MCM2 after 48 h concurrently underlines the diminished proliferation rates on nanoporous glass during the first days of exploring and remodeling the adhesion surface by matrix production. A more and more natural protein layer on the surface, produced by the cells, could then facilitate cell adhesion and proliferation on the nanoporous samples in the subsequent days. The production of ECM molecules like collagen and fibronectin by L929 cells is described in studies on collagen-PLLA hybrid nanopore structures secrete ECM-like structures on the surface, where a similar trend towards larger nanopores was found[176]. In our experiments, the expression of ACTA2 is reduced on larger pores, indicating less tension inside the cell caused by decreased cellular contraction. An overall reduced cytoskeletal elongation and contraction can have a decisive effect on other cell functions such as intracellular transport[136], which can then take place in a more physiological way inside cells that are not artificially contracted by stretching across a surface lacking topographic stimuli. Below 80 nm pore size, another

drastic change in expression can be observed: A peak for FAK (Focal Adhesion Kinase) is clearly visible, which, together with a lower proliferation for small pores, indicates that a large portion of cells on those samples has a tendency towards anoikis - programmed cell death due to poor cell-substrate adhesion[177,178]. Thus, we assume that the up-regulation of FAK is due to the fact that the majority of cells on the smaller nanopores are fighting against anoikis: This could be caused by a lack of properly sized "adhesion-islands" inbetween the pores a high percentage of initially initiated adhesions might be retracted due to a lack of available surface area and should be further examined by high-resolution microscopy in future studies. On samples with larger pores, they are already producing ECM molecules and start to proliferate. After 4 days of delay, sufficient surface remodeling has occurred on the smaller porous samples and proliferation slowly begins.

Furthermore, the nanoporous glass membranes were analyzed for their interaction with primary hMSCs. This specific cell type is a very promising candidate for translation research in tissue engineering due to its differentiation potential. The cell clustering observed during the first days of culture on nanoporous glasses indicates a diminished initial cell adhesion on the uncoated, rough surfaces, where cell-cell contacts are preferred. After three days of culture, no clustering is observed, cells have fully spread onto the surface. An overall good proliferation could be observed on all surfaces, indicating the suitability of nanoporous glass for the robust expansion of mesenchymal stem cells. This fits well with the findings of a study on the interaction of osteogenic cells with nanoporous titanium surfaces with mean pore diameters of ~ 20 nm, where an overall increased adhesion and upregulations of adhesive genes were found[179]. In our mRNA expression experiments on hMSCs, a trend towards chondrogenic differentiation could be observed for nanoporous glass membranes during the first two weeks of culture, most pronounced for samples with a mean pore size of 17 nm. This manifested in the increased expression of COL10, COL2A1 and SOX9, which are

all key players in chondrogenic differentiation[180]. Especially COL2A1 and SOX9 are characteristic for immature chondrocytes[181], potentially indicating early chondrogenic differentiation states after 7-12 days of culture. The rather disordered actin organized on nanoporous samples could also point towards a trend for chondrogenic differentiation. A material-intrinsic differentiation effect, without external stimulation, is a very promising result and has the potential to controllably modulate stem cell fate[182]. The overexpression of COL10 might point to a bias towards hypertrophic differentiation, an effect that could be fostered for the buildup of models for osteochondral ossification on nanoporous membranes[183]. These first results for hMSC interaction with nanoporous glass membranes presented in our study indicate that cell differentiation could be induced by these surfaces without any further media supplements. Furthermore, standard differentiation experiments could be sped up by surfaces that facilitate proliferation[184].

In the short-term cell adhesion and proliferation experiments with SK-MEL-28 melanoma cells, the quick adhesion to the nanoporous glass surface proves the nanoporous glass membranes' function as a nanotopographical, three-dimensional environment for cell adhesion. In contrast to the FLAT glass surfaces, cells on nanoporous glass resist the gravitational force after only 3 h of adhesion time. The initial cell adhesion on the FLAT samples is decreased by 47 %, indicating diminished initial adhesion. In the first four days of upside down culture, the constant relative cell number on the nanoporous glass surfaces is an indicator for the fact that cells on the nanoporous surfaces perceive the gravitational force and that their proliferative behavior is influenced by their struggle for adhesion. However, cell numbers on the nanoporous surfaces did not decrease during the first days of upside down culture while there was a progressing decrease on FLAT samples. While a diminished, but still measurable proliferation could have been attributed to lower cell density caused by the 47 % lower initial cell count, the absence of proliferation displays that the cells are losing their struggle for adhesion and

detach from the surface. The subsequent constant proliferation on the nanoporous glass membranes in contrast to the continuous decay of the relative cell number on the smooth glass surfaces strengthens the hypothesis of positive cell-material interaction: The nanoporous glass surface supports cell adhesion by its inherent nanoscale surface topography. Thus, the cells perceive the nanoporous surfaces as a 3D environment, enabling increased initial cell adhesion by nano-sized topographic stimuli that facilitate the quick manifestation of focal adhesions at the surface after only 3 h of adhesion. This leads to the conclusion that for strongly adherent cells like SK-MEL-28, a nanoporous glass surface – presenting topographic stimuli for filopodia stabilization – is much closer to their natural environment in the human body than smooth 2D surfaces. This result is strengthened by the morphological findings, displaying increased protrusive activity and an increased area on nanoporous glass membranes. This points to an active adhesion mechanism with strong focal adhesions that can resist the gravitational force and keep the cells in place. Furthermore, cells also undergo extensive proliferation on the nanoporous glass membranes. Thus, they manage to partly deadhere, divide and spread on the surface again during the process of mitosis, proving that cells not only adhere but perform their normal function in 3D topographic environments. This is also confirmed in other studies, e.g. it was shown that osteoblast-like SaOS-2 cells adhere much better to titanium surfaces with 0.5 µm and 2.0 µm pores than on flat reference surfaces after an equally short incubation time of 1-2 h[185]. In a study on nanoporous anodic aluminium oxide with a similar anisotropic surface structure, Poinern et al. found an overall good cell adhesion and slightly increased proliferation for the Vera cell line[186]. In our experiment, the nanoporous membranes facilitate initial cell adhesion without additional functionalization/coating, indicating a 3D scaffold effect and an altered adhesion mechanism compared to flat surfaces.

The effect of differential adhesion on nanoporous and flat glass was further examined in a functional drug assay, utilizing one of the most common cell lines

for breast cancer and the prominent anti-cancer drug paclitaxel. The aim of this assay was to find a quick test for having a distinct effect of a drug on a specific cell function. An assay that gives quick outputs for drug effects on patient cells could speed up drug screening in personalized medicine, e.g. to find a suitable drug for a specific patient and cancer type. We probed this in an adhesion assay with MDA-MB-231 breast cancer cells that were treated with paclitaxel in upside down culture. Paclitaxel is an active agent that inhibits the disassembly of microtubules. These play a crucial role in diverse vital processes like the chromosome separation during mitosis, adhesion and focal adhesion disassembly[187]. Microtubule-inhibiting agents are particularly effective in fast dividing cells like cancer cells and are often used for the treatment of breast cancer. Paclitaxel can lead to a dwelling during mitosis due to a mitotic spindle stabilization, followed by apoptosis. Alternatively, it can induce a mitotic block that leads to multipolar cell division and subsequent apoptosis of the daughter cells with reduced chromosome number. Cells on nanoporous glass and FLAT surfaces were pre-incubated for 24 h under standard cell culture conditions (standard procedures, upright cell culture) and then cultured upside down. At this timepoint, all samples exhibited normal, comparable cell densities with spread cells, indicating a good starting point for the assay. For nanoporous surfaces, we observed a pore size independent drop in the relative cell numbers 48 h after 500 nM paclitaxel was added to the medium, while cell numbers on the FLAT surface were almost constant. This indicates an altered cellular adhesion mechanism on the porous glass substrates that seems to be highly dependent on microtubule dynamics. While proliferation is highly diminished or even stopped on all samples, a high number of cells detaches from nanoporous samples while cells on FLAT samples remain adherent. In a recently published study, we found that the microtubule-diminishing drug Benomyl has a similar effect on the adhesion on amoeboid cells of *Dictyostelium discoideum* to nanostructured SiO_2 fibers: Upon drug treatment, almost all of the cells deadhere from the nanostructured fibers, adhesion to flat

glass is persisting[188]. These findings indicate a suitability of these nanoporous substrates for the quick detection of active substances that interfere with cytoskeletal and adhesion processes. This or similar effects found in future studies could be fostered for clinical application, e.g. in personalized cancer treatments to see if a specific patient's cancer cells respond differently to a set of potential drugs or drug combinations.

6. Conclusions

We have shown that nanoporous glass membranes are a bioactive material that provides an adhesion surface for various cell types from pathologic and from healthy human tissue. Our pioneering study targeted the identification of potential effects of nanoporous glass surfaces on different murine and human cell types, for both cell lines and primary cells. We were able to identify cell-type specific effects of certain nanoporous glass membranes within our specific experimental setups. Future studies should aim at confirming these findings for other cell types, identifying differences in cell behavior and broadening the knowledge on cell behavior in different experimental setups.

We found differential adhesion characteristics and modulation of gene expression in L929 fibroblasts, just by changing the pore size, which points towards a direct influence of the pore size on nanoscale cellular processes: Glass with a mean pore size above 80 nm can serve as a macroscopically flat, but intrinsically nanostructured topographic surface for cell culture applications even without additional bio-functionalization. The change in gene expression for L929 and hMSCs as a function of pore size implies a cell-specific cut-off pore size for a positive cell adhesion effect. In future studies, the bioactivity of the nanoporous glass samples could be further tailored towards a positive or negative interaction with specific cell types by varying the pore sizes or introduction of surface functionalization or coating. Potential effects on differentiation, as observed in the trend towards chondrogenic lineage for

hMSCs on nanoporous glass membranes with 17 nm mean pore size, might enable various future applications for nanoporous glass membranes in hMSC research and tissue engineering. Additionally, a strongly increased adhesion and proliferation of SK-MEL-28 cells on nanoporous glass compared to flat glass references in upside down culture was identified. This underlines that nanoporous glass membranes are suitable for use in 3D cell culture vessels or bioreactors with cell adhesion to all surfaces in 3D. The material can provide cell adhesion while still allowing constant perfusion for nutrient flow and cell-cell signalling. Finally, paclitaxel treatment of MDA MB 231 breast cancer cells shows more rapid effects on nanoporous glass membranes in upside down culture compared to FLAT glass references, with strongly diminished cell adhesion and proliferation after only 48 h. Drug assays and the development of personalized treatments could be sped up by fostering this differential cell adhesion effect on nanoporous glass membranes. Furthermore, complex functional assays, including microfluidics and other stimuli, could benefit from a more physiological cell behavior and proliferation rate on nanoporous glass surfaces.

We conclude that nanoporous glass membranes present nanoscale cues that act as bioactive triggers to influence cellular cascades for the regulation of cell functions. This proves the suitability of the substrates as a functional cell culture surface. Our findings underline the versatile application potential of nanoporous glass membranes for cell culture. Deepening the understanding of our findings can can lead to new approaches for existing needs in both science and the biotechnical and biomedical industry.

7. Appendix

7.1 Acknowledgements

We thank Sebastian Kress (Fraunhofer ISC, Würzburg) for providing L929-GFP cells, Franziska Ehlicke (Department of Tissue Engineering and Regenerative Medicine, University Hospital of Würzburg) for isolating and providing human mesenchymal stem cells and Christoph Rücker (Fraunhofer ISC, Würzburg) for his help and guidance in MSC culture.

7.2 Declaration of Interest

7.2.1 Financial Interest

This work was funded by the Fraunhofer Attract 3D NanoCell Program.

Part of this research is part of the US Patent Application #20190345443 “Method for the Culturing and Differentiation of Cells” and the EU Patent Application #19170636.5 “Intrinsisch nanostrukturierte 2.5D-Zell-kulturoberflächen für Stammzell-Differenzierung, Drug-Screening und Zellkultur", both filed by the authors Martin Emmert, Ferdinand Somorowsky and Doris Heinrich.

7.3 Supporting Information

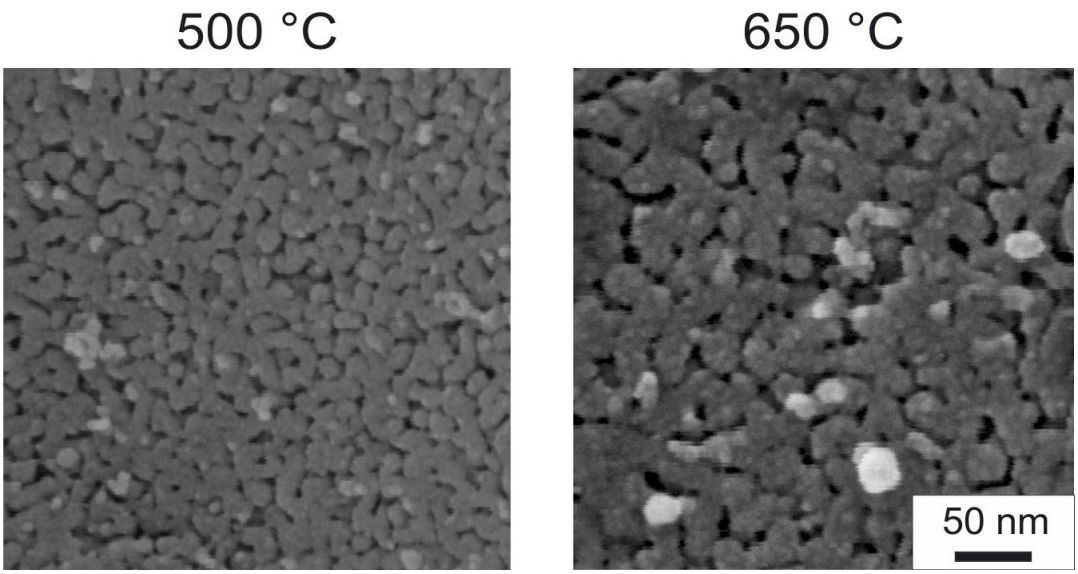

Figure 31: SEM micrographs of nanoporous glass samples with 80 % SiO2 and different demixing temperatures.

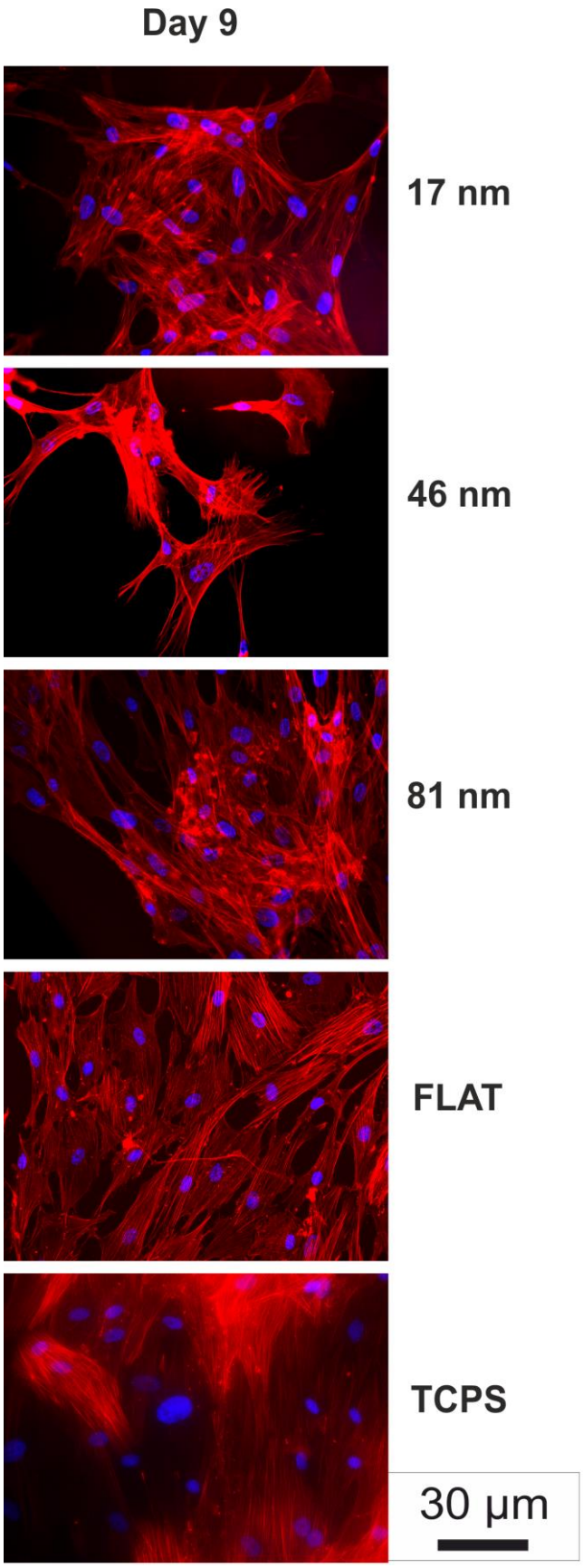

Figure 32: Microscopy images of hMSC at different timepoints with actin cytoskeleton stained by phalloidin and DAPI stained nuclei.

VI. Discussion & Conclusion

1. Discussion

This thesis investigated cell behavior in reaction to different material surfaces. Three distinct studies yielded valuable contributions to better understanding the interaction of living cells with three different types of surface features ranging from micron- to nanoscale:

1. Controlled microtopographies made of PDMS micropillars (Chapter III)
2. Intrinsically nanostructured silica fibers (Chapter IV)
3. Nanoporous glass membranes (Chapter V)

Each of the studies led to the identification of distinct effects of the respective topographies on cell behavior that can be further investigated in future research or be directly moved towards application development. In addition to the detailed discussions within Chapters III-V, this chapter will discuss how the findings can be extended, e.g. to other cell types and how combined approaches of the different findings/setups could be utilized for more realistic cell assays.

1.1 Findings on Amoeboid Cell Behavior

The investigation of amoeboid cell migration **inside controlled PDMS microtopographies** yielded the following findings for the different topographies:

High density pillar regions

- A distinct tendency towards directed pillar-to-pillar runs was observed, which means that **pillars are sensed as attractive stimuli for migrating cells**.
- In addition, we found an inhibition of cell motility for cells in random probing states, which means that **pillars are obstacles for cells in random probing states**.

Gradient density pillar fields

- Amoeboid cell migration displays a **trend towards regimes of inter-pillar spacing close to the cell diameter**.

Locally anisotropic pillar fields

- **Amoeboid cell motility is clearly diminished due to a lack of attractive migration stimuli** in the vicinity of the cell.

The main findings for amoeboid cell behavior on **intrinsically nanostructured silica fibers** are:

Cell Migration

- **Highly increased motility on silica fibers** compared to flat glass.
- On silica fibers, Myosin II null mutants were as active as cells with myosin II. Motility of cells lacking myosin II was greatly hindered on plain glass, which leads to the conclusion that **cell migration on**

instrinsically nanostructured silica fibers is driven by a different migration mechanism than on flat glass.

Cell adhesion

- **Amoeboid cells detached from the fibers after deprivation of mictotubules** by adding an active agent.
- In contrast, amoeboid cells on flat glass remained adherent, elucidating the fact that **amoeboid cell adhesion on nanostructured silica fibers is mediated by a different molecular mechanism than on flat glass**.

In follow-up studies, these distinct effects of micropillar and nanostructured topographies on amoeboid cell migration should be extended towards human cell types exhibiting amoeboid behavior. If only some of these effects can be confirmed there, they could be fostered for novel applications that could better resemble physiological conditions. The potential translation of results from *D. discoideum* amoeboid cells and human amoeboid cells has been shown already: In an interesting study, Sun et al. found that directed cell migration can be triggered by local nano- and microtopographical gradients for amoeboid migration in both *D. discoideum* and human neutrophils[189]. Further analysis revealed that this effect is based on the propagation of intracellular actin waves, an effect that has been investigated and established in *D. discoideum*[66,190–192], e.g. by Driscoll et al.: They probed directed migration of *D. discoideum* on PDMS surfaces exhibiting periodically spaced nanoridges and found increased directed migration parallel to the ridges. In addition, they observed that actin polymerization waves are facilitated by the surface topography, where they can propagate in a directed manner. Thus, they concluded that this contact guidance effect is caused by oscillatory shape dynamics[135]. Interestingly, this is a very active field of research at the moment also for other cell types[193].

Another focus of further research on this topic should point towards the potentially microtubule and actin foci based mechanisms of migration and adhesion on the intrinsically nanostructured silica fibers that greatly differs from the flat glass substrates. If the underlying biochemical pathways and the resulting biophysical mechanism can be elucidated, this could be fostered in potential applications.

In future studies, the investigated features (micropillars and nanostructured surfaces) could be combined in order to systematically evaluate possibilities to achieve even more pronounced effects on amoeboid migration and the behavior of mammalian cells. With increasing availability of micro- and nanofabrication techniques, more and more defined surface features can be realized[152]. For example, it has been shown that the combination of three different PDMS microscale features (holes, pillars, and grooves) on one substrate led to distinct changes in the morphology and adhesion behavior of hMSCs with a stabilization in cell sheet formation and an increase in osteogenic marker expression and calcification. Samples with two different cues (holes and pillars) showed a less pronounced trend, but still had elevated levels of ALP compared to a flat sample[194].

Furthermore, functional studies probing the modulation abilities of silica fiber fleeces on the immune response should be carried out to further elucidate their distinct effect on wound healing. In addition, future investigations should also concentrate on the interaction of silica fibers with other cell types that contribute to wound healing. For example, keratinocytes in ulcers (non-healing wounds) are proliferative, but do not migrate, while in acute, normal wound healing, there are more non-proliferative, migrating keratinocytes[195]. Thus, migration induction by nanostructured silica fibers could potentially facilitate the healing of ulcers. A first clinical study has shown that the fiber material is a well-tolerated biomaterial in wound healing, but did not show increased healing compared to the standard-of-care[196]. Thus, it could be used as a carrier

material to support healing by controlled release of drugs or growth factors, as shown in a study by Czuryszkiewicz et al. in 2002[197]. In a publication by Grotheer et al. on the same fiber material as in this thesis, no negative effect on *in vivo* wound healing in a porcine wound model could be seen. The fiber fleeces used in the study were fully biodegradable and wound closure was normal, underlining the good biocompatibility of the fiber material. Interestingly, they could show a distinct reduction in inflammation, fibrosis, and keratinocyte proliferation[198]. This study is in good accordance with general findings and hypotheses on the therapeutic effects of orthosilic acid, which is the major form of bioavailable silicon for humans and also the major dissolution product of the silica fibers[198]. With a mean diameter of 60 ± 20 µm, they are also suitable for fibroblast adhesion, as the minimum fiber diameter is ~10 µm. Below this limit, fibroblasts in a study carried out on PLLA fibers simply detached from the fibers[199]. The authors of the mentioned publication also suggested to include nanostructures at the fiber surfaces for future investigations, a feature that is intrinsically given by bio-degradation for the fiber material used in this work. In preliminary studies, we have already shown that fibroblasts in a wounded skin model show good adhesion to the silica fibers after 5 days of culture.

1.2 Findings on Mammalian Cell Behavior on Nanoporous Glass

In Chapter V, this thesis presented the first systematic study on the **interaction of mammalian cells with nanoporous glass membranes**. The summarized findings of this work are:

L929 Fibroblasts

1. After initial delay, we observed an **almost exponential cell proliferation of L929 cells on nanoporous glass, with a positive trend for mean pore sizes > 80 nm.**
2. **Gene expression profiles of L929 cells confirmed these trends**, with a distinct difference in profiles below or above 80 nm mean pore size.

Human Mesenchymal Stem Cells (hMSCs)

1. **hMSCs proliferate well on all nanoporous glasses.**
2. In addition, there is a **trend towards upregulation of chondrogenic genes by 17 nm mean pore size glasses.**

SK-MEL-28

1. **Nanoporous glass membranes present a 3D topographic surface that enables cells to adhere against the influence of gravity** after only 3 h of adhesion time.
2. **Cell adhesion & proliferation on flat glass is highly diminished** under the influence of gravity.

MDA-MB-321

1. **Paclitaxel treatment of MDA-MB-231 breast cancer cells shows more rapid effects on nanoporous glass membranes** in upside down culture.

An additional, practical outcome of this work is a process for the fabrication of uniform batches of nanoporous glass membranes that can be used in cell culture. The sample size (16 mm × 16 mm × 250 µm) was defined to perfectly fit into 6-well plates for the conduction of pre-screening studies. In many preliminary experiments, we established protocols for the effective leaching, washing, and sterilization of the nanoporous glass membranes to make them ready for cell culture. On the material side, future studies could focus on further reducing the sample sizes to enable larger screening studies in 24-, 48-, or even 96-well plates.

To this point, there is only one other study on the effects of nanoporous glass membranes as cell culture substrates by Jones et al. that investigated microporous bioglass scaffolds for bone regeneration that had an inherent nanoporosity. They found that the interconnected mesopore system of 2-50 nm pore sized increased the adhesion of osteoprogenitor cells[200]. As they used a completely different material system and synthesis process, this is not comparable to our study. This is why the literature discussion will review similar surfaces and studies in addition to the discussion in the publication.

The tendency for increased attractive interaction for mean pore sizes above 80 nm could be explained by the findings of Patla et al: For the rat fibroblast cell line REF52, they identified that the spacing of focal adhesion integrin complexes is ~45 nm while single adhesion sites are ~25 nm in diameter[201]. This is in the range of the “adhesion islands” of nanoporous glass that are separated by the nanopores, while they are often smaller than this range for smaller nanoporous samples. This could be a good dimensional fit in comparison to the results of the described study. A publication by Poole et al points in the same direction: They compared fibroblast motility and alignment on collagen-coated surfaces with and without the physiological D-periodic banding of 67 nm. Only on the surfaces that exhibited the characteristic collagen periodicity that is present in the human body, fibroblasts showed

directed motility and cell body alignment[202]. On nanogrooved surfaces, human vein endothelial cells (HUVEC) cells show diminished expression of cell cycle and extracellular matrix proteins[203]. In another study with HUVEC cells, Muhammad et al. observed enhanced proliferation on TiO_2 surfaces with nanogratings of ~70 nm, while smooth muscle cells (SMC) displayed a decreased proliferation on the same surfaces[204].

Like shown in this thesis, there are many other examples that point towards an influence of nanoscale surface features on stem cell behavior: In fact, stem cell behavior can be influenced in specific ways by nano- and microstructured materials[205–207]. As MSCs are adherent cells, they directly interact with the topography and chemistry of their substrate by membrane proteins. This influences the concentrations of lineage-specific metabolites inside the cell, increasing the differentiation potential into specific directions[208]. In addition to surface topographic cues themselves, the degree of topography order can play an important role in differentiation processes[209,210].

In several experiments on the influence of micro- vs. nanoscale silicon pillar topographies on the behavior of rat MSCs compared to flat surfaces, Brammer et al. elucidated that the nanosized cues had a significantly higher impact on cell adhesion and growth. MSCs on the nanopillar surfaces were less spread than on micropillar and flat surfaces, pointing towards a distinct change in the adhesion mechanism for nanopillars. Furthermore, osteogenic differentiation was induced by the nanoscale topographical cues and an increased mineralization could be measured[211]. In another study, Lavenus et al. found that for mesenchymal stem cells cultured on titanium surfaces with nanopores of 30 nm and 150 nm, osteogenic differentiation is induced, indicated by the increased expression of ALP, COL1A1, RUNX2, BSP, and OCN. For the 30 nm pores, a more branched morphology of hMSCs was observed[212]. Oh et al. showed that hMSCs cultured on Ti nanotubes showed higher initial cell numbers an increased tendency for osteogenic differentiation on

nanotubular/nanoporous surfaces of 30 nm, 70 nm, and 100 nm average poresize. For pore sizes < 70 nm, a 10-fold increase in cell elongation could be observed, leading to increased cytoskeletal stress. This activated mechanotransductive pathways that lead to differentiation into osteoblast-like cells.[213] In contrast, Zhao et al. did not observe increased initial cell adhesion for hMSCs on titania nanopores, showing the need to be cautious with results from a single study[214,215]. In their study from 2012, they saw a slightly diminished hMSC proliferation during the first day, which corresponds to the findings in this work for all proliferation studies on nanoporous glass membranes. For all nanoporous samples, they saw upregulations of osteogenic genes[215].

In good accordance with our findings for the overhead culture of SK-MEL-28 melanoma cells, a study on initial cell adhesion on porous silicon surfaces concludes that nanoporous silicon surfaces with an average pore sizes of 36 nm provide anchoring points for filopodia growth. They found that the nanotopographies act as a support for cell attachment, development and migration in stem cells and the breast cancer cell line MCF-7[216]. The fact that there is a systematic, pore-size dependent interaction with nanoscale features in mammalian cells is also underlined by a study of Dalby et al.: Utilizing polymer demixing, they prepared micro-islands with a controlled height of 27 nm on flat surfaces and investigated the behavior of fibroblasts. They observed increased initial and long-term adhesion on the surfaces exhibiting nanoscale features[217]. Similar findings were reported in a study published by Cai et al., who investigated osteoblast viability and proliferation on titanium surfaces with different nanoscale surface roughness[218].

2. Conclusion & Outlook

If the effects found for amoeboid cell migration in this work can be confirmed for human immune cells, this may be fostered for the buildup of a novel type of bioactive wound implants. For instance, utilizing the effect of the intrinsically nanostructured fiber surfaces could enable immune cells to immigrate the wound site faster and accelerate the immune response in all three dimensions. This increased immigration of immune cells could also help to dampen the overall immune response and, thus, reduce the cytotoxicity of the wound site to promote tissue regeneration instead of scar formation[41,148].

Additionally, combinations of different stimuli could enhance the effects found for the three different topographies investigated here. For example, micropillar arrays of nanoporous glass could in the future be manufactured via Fe-based glass 3D printing, which is already possible at larger scales[219]. This approach of hierarchically structured topographies at the micro- and nanoscale has been shown to strengthen individual adhesion sites[220]. And even more interesting, hierarchically structured nanoporous glass substrates could not only be used for migratory studies, but also for hMSC applications: For example, it was shown that a combination of micron- (~1–2 µm) and meso-scale (~100-1000 µm) topographic features influences hMSC morphology and also organizes neo-tissue formation by aligning the fibrillar collagen produced by hMSCs[221]. Thus, the hierarchical combination of topographic stimuli could yield next generation bioactive substrates that combine different bioactive stimuli.

Additionally, surface functionalization and wettability can have a great influence on adsorbed proteins and cell adhesion[222]. The observed effects on cell behavior could be further enhanced by surface modification, which could easily be performed on both the silica fibers and the nanoporous glass membranes via silanization processes. For example, positively charged amino groups at the surface can improve MSC adhesion and induce osteogenic differentiation, while carboxy surface functionalization leads to more rounded

cells that show a trend towards chondrogenic differentiation[223]. In a study combining surface topography and functionalization, Kafi et al. showed that nanopillars fabricated of RGD oligopeptides enhanced cell functions of several cell lines compared to surfaces with 2D nanodots and a flat surface made of the same material[224].

Besides the adherent tissue cell types that are typically tested in studies on biocompatible or bioactive materials, it is extremely important to have the overall complexity of physiological systems in mind and to steadily increase the complexity of the models and assays used. A systematic investigation on the response of specific cell types to specific material surfaces will contribute to the elucidation of an increasing number of details on cell-material interaction, but it cannot reflect physiological situations. Thus, it is of utmost importance to develop more and more complex test models for "functional units" inside the body. Steps towards this are on the way, e.g. by including cells from the immune system: In a recently published study on the cell response to nanoporous microstructures, Chen et al. report that activated macrophages cultured on their nanoporous surfaces showed anti-inflammatory effects compared to macrophages cultured on flat surfaces. They showed a more spread morphology and an increased expression of important autophagy pathway components. Furthermore, for macrophages cultured on surfaces with pore sizes of 50 nm and 100 nm had more than 2-fold increases in the release of the osteogenic factors (BMP2, BMP6, WNT10b), pointing towards a differentiation-regulating function of macrophages. When rat bone marrow stem cells (rBMSCs) were cultured on the same surfaces, osteogenic differentiation was promoted when a medium conditioned by macrophages on 50 nm surfaces was used.[225] The importance of topographies on macrophage response was also highlighted in a study carried out by Ghrebi et al., where macrophages were cultured on different surfaces exhibiting a micro-topography. They also found an increased activation of macrophages on structured surfaces, accompanied by a more spread cell morphology[226]. Bota et al. could show that expanded

PTFE materials exhibiting microtopographies decreased the thickness of fibrous capsules in wound healing *in vivo* and distinct differences in the release of inflammatory cytokines from macrophages *in vitro*[227]. Including macrophages can also be beneficial for the build-up of more realistic *in vitro* tumor models to study the effect of novel drugs[228].

An interesting approach for future studies could also be the partial in-situ leaching of nanoporous glasses in cell culture: Ionic dissolution products from inorganic materials can provoke specific cell responses.[229] Thus, scaffolds or culture substrates made of only partially leached out nanoporous glass that is doped with defined inorganic trace elements could induce specific cellular pathways.

To draw a conclusion, the studies presented in this work showed novel and distinct effects of micro- and nanoscale topographies on the behavior of various types of living cells. These examples display how versatile the potential for applications of bioactive materials could become in the next years and decades. And yet this variety of different alterations of cell functions due to topographic cues also shows the crucial part of this field of research: Carving out distinct, robust correlations of external cues and cell behavior is of utmost importance to derive definitive design implications that can lead to scientifically, clinically and commercially successful products.

VII. ADDENDUM

This chapter was published as a mini-review as

“Challenges in tissue engineering – towards cell control inside artificial scaffolds”

by Martin Emmert, Patrick Witzel and Doris Heinrich

in Soft Matter, 2016, 12, 4287–4294

Julius-Maximilians-
UNIVERSITÄT
WÜRZBURG

Fakultät für
CHEMIE UND
PHARMAZIE

Erklärung zur Autor:innenschaft

Challenges in tissue engineering – towards cell control inside artificial scaffolds
Martin Emmert*, Patrick Witzel and Doris Heinrich Soft Matter, 2016, 12, 4287–4294 (* = Hauptautor:innen)

Detaillierte Darstellung der Anteile an der Veröffentlichung (in %)
Angabe Autor:innen (ggf. Haupt- / Ko- / korrespondierende/r Autor:in) mit Vorname Nachname (Initialen)

Martin Emmert (me), Patrick Witzel (pw), Doris Heinrich (dh)

Autor:in	me	pw	dh	A4	A5	A6	A7	A8	A9	A10	A11	∑ in Prozent
Verfassen der Veröffentlichung	35%	35%	30%									100%
Korrektur der Veröffentlichung	33,3%	33,3%	33,3%									100%
Koordination der Veröffentlichung	35%	35%	30%									100%
Summe	34,4%	34,4%	31,1%									100%

1. Abstract

Control of living cells is vital for the survival of organisms. Each cell inside an organism is exposed to diverse external mechano-chemical cues, all coordinated in a spatio-temporal pattern triggering individual cell functions. This complex interplay between external chemical cues and mechanical 3D environments is translated into intracellular signaling loops. Here, we describe how external mechano-chemical cues control cell functions, especially cell migration, and influence intracellular information transport. In particular, this work focuses on the quantitative analysis of (1) intracellular vesicle transport to understand intracellular state changes in response to external cues, (2) cellular sensing of external chemotactic cues, and (3) the cells' ability to migrate in 3D structured environments, artificially fabricated to mimic the 3D environment of tissue in the human body.

2. Introduction

To ensure the viability of living cells, a great variety of biochemical and physical processes have to be coordinated[17]. This sophisticated out-of-equilibrium system is orchestrated by complex interdependent processes within the extremely crowded and active cell interior. Chemical and physical signals in and outside of cells determine biological processes, such as cell migration and morphogenesis[18]. Mechanisms of cell functions are based on highly organized intracellular structures and systems, ranging in size from the nano- to the micron-scale. These structures are intrinsically dynamic, exhibiting active and passive transport phenomena to pass on information between different regions inside the cell[19].

While the genome provides the blueprint for all vital processes, the interaction of living cells with their environment determines cell functions. Not only molecular concentration gradients[20] but also mechanical interactions with 3D

scaffolds of the extracellular matrix determine functionality of living cells, such as adhesion, migration, proliferation and differentiation[21].

The ability of cells to migrate in 3D environments under defined external cues (*i.e.* in the form of chemical or topographic gradients) in the host organism is essential for life. Malfunction of these processes often results in diseases in living organisms.

A new insight into disease mechanisms is of utmost importance to develop novel strategies for curing diseases like neuronal degeneracy[22,23], cancer[24], and inflammation[25] or to identify the mechanistic origins of rare diseases. Additionally, this understanding will promote the development of innovative cell guiding strategies, e.g. for scaffold design in tissue engineering and innovative cell sorting techniques for diagnostic purposes.

This review summarizes studies that advance the abilities to control and analyse cellular functions using physical methods (Figure 33), with a focus on amoeboid cells. Central questions are:

1. How does the seemingly random noise pattern of intracellular transport reflect the plasticity of the cell interior? And how can this be analyzed to extract relevant motion states?
2. How is a living cell capable of precisely sensing chemotactic cues from the environment?
3. How are active dynamic control mechanisms changing the global shape of the cell by microtubule-actin crosstalk to adapt to the 3D environment? And how do cells perform directed migration in 3D environments?

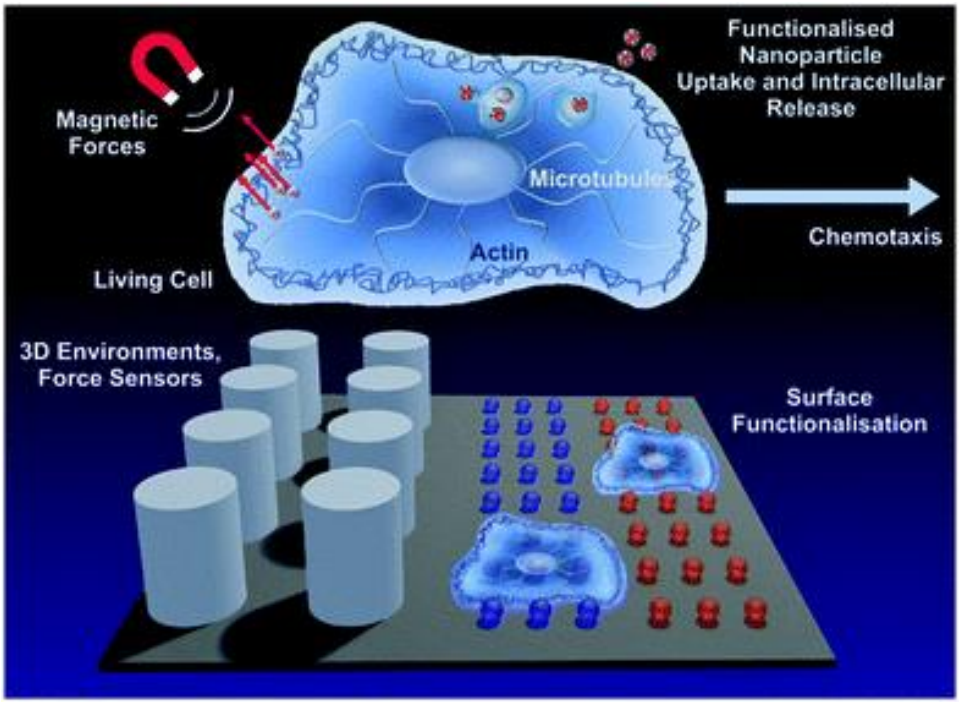

Figure 33: Schematic overview of experimental approaches to elucidate cell behavior, signal processing and cell-substrate interaction. Intracellular information and material transport are probed by uptake and intracellular release of functionalized nanoparticles, in addition to magnetic force application. Cell-substrate interactions are controlled by cell type specific surface functionalization. 3D environments are investigated and specifically adapted to match individual cell requirements for scaffold design, in addition to force sensors for the analysis of cellular pulling and pushing forces.

To answer these questions, it is essential to exert boundary conditions to living cells by applying external cues which keep key cell functions in a defined state. A controlled change of these predefined conditions induces state changes in living cells which can be quantified by extracting the relevant motion data. The following sections will display the importance of a mechanistic understanding of intracellular transport states (Section 2), chemotaxis (Section 3) and topographic cell guidance (Section 4) for the development of novel solutions for medical diagnosis and therapy. This systematic approach will facilitate the design of cell type specific 3D environments that allow for cell guidance and provide culture conditions similar to the cells' physiological environment.

3. Intracellular information and material transport

A living organism is a highly dynamic system that depends on the accurate interaction and performance of every subunit. In a densely crowded cell interior under non-equilibrium conditions, the transport of proteins, vesicles, and cellular building blocks is crucial for fast adaptation and for response mechanisms in reaction to extracellular cues. These cellular state changes are characterized by distinct transitions in intracellular transport processes. Extracting these state transitions from intracellular motion data will serve as a readout of cell response to mechanical or chemical cues and as a novel tool for the analysis of cell–material interactions.

To advance our understanding of the impact of cellular architecture on intracellular dynamics, several methods have been developed for automated, reliable and time-resolved identification of motility signatures of cytoplasmic tracers[17,123,230–234]. Such approaches are both experimentally challenging and of fundamental importance. As an example, investigations on intracellular trajectories of beads moved by optical tweezers revealed anomalous diffusion behavior depending on the particle diameter[231].

In living cells, motile vesicles undergo two types of motion (Figure 34): directed transport, driven by molecular motors on filaments, and thermal diffusion in the crowded, active medium[123,139,235–239]. The combination of random and directed motion phases in the cytoplasm exhibit great advantages. Directed motion by bio-motors along microtubules (MT) rapidly transports vesicles between the periphery and the cell center[233,234]. In contrast, random walks are very slow considering the high viscosity of the cytoplasm. This motion alone would explore the whole space but it would be too slow to ensure viability. The combination of these two motions facilitates very effective intracellular transport with fast-directed motion phases and diffusion, to ensure efficient search modes for chemical reactions to occur in the cell. This

efficiency of combined directed and random motions in cells has also been predicted by theoretical studies[17,240].

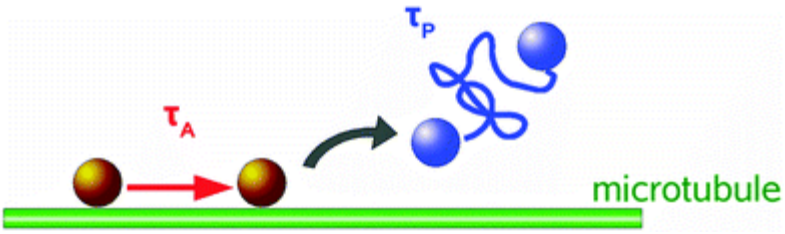

Figure 34: Two state distribution of tracer bead motion: State 1 – molecular motor associated motion along microtubules with attachment duration τA. State 2 – detachment from microtubule and diffusive motion of duration τP.

A basic and general analysis method to investigate intracellular transport motions is the mean squared displacement (MSD) method applied to trajectories of intracellular tracers[19]. A more detailed local MSD method with directional persistence analysis of the tracer path distinguishes diffusive motion from directed transport along MTs, by reliably separating diffusive and directed motion phenomena of particles[123]. To extract these two motion modes, particle motion is analyzed in terms of a two-state motility model, yielding distributions of state durations as well as state parameters, i.e. velocities during directed motion phases and diffusion coefficients.

Experiments with colloidal probes engulfed by *Dictyostelium discoideum* cells exhibit the described two-state motion in the cytoplasmic space: random walks and directed motions with high velocities. Thus, transport of intracellular cargoes proceeds by successive phases of diffusion and directed motion. The calculated local velocities are best characterized in terms of very broad log-normal distributions comprising velocities over 3 orders of magnitude up to a few microns per second[70,123].

The velocity distributions reveal subtle changes in the intracellular transport behavior caused by modifications of the cytoskeleton composition due to mutations, hormones, or drugs[123,235,237]. To identify the precise effect of

different components of the cellular micro- and nanoarchitecture on vesicle transport, cytoskeleton parts were selectively disturbed by using depolymerising drugs. Examples are the decomposition of the MT network by benomyl and of the actin cortex by latrunculin A. In both cases, the fast motion states vanish. The removal of myosin II motors results in a decrease of the overall velocities corresponding to an apparent increase in the cytoplasm viscosity. Determined active state durations obey a decaying exponential distribution, whereas the durations of the random states follow log-normal distributions[241]. The diffusion coefficients exhibit a broad log-normal distribution revealing that the random walks are not pure Brownian motions[238]. Such behavior is typical for diffusion in complex fluids with fractal dimensionality[70].

3.1 Langevin model of intracellular subdiffusion

The subdiffusive regime is particularly interesting for inferring information about the dynamics of the cytoskeleton morphology and intracellular transport. To investigate the more complex intracellular transport processes leading to subdiffusion, all directed motion was excluded.[16] Experimental results are compared to simulations of a data-driven Langevin model with finite correlations, capturing essential statistical features of the local MSD analysis[123,139,235]. The statistics of this local MSD algorithm were calculated and a stochastic model of intracellular subdiffusion was developed for random motion with Gaussian velocity fluctuations, with a given correlation function[139]. Thus, subdiffusive transport in *D. discoideum* cells can be described by Brownian motion with correlated Gaussian velocity fluctuations. In the experimental data, increments are Gaussian only to a certain approximation and no higher order or nonlinear correlations were incorporated in the model[235].

Both microtubules and actin filaments act as the cause of intracellular subdiffusion[235]. In general, microtubule sweeping motions liquefy the cytoplasm on all time scales, whereas actin-microtubule cross-talk generates a liquefying effect only at time scales longer than 0.2 s. The F-actin induced decrease in effective diffusion coefficients was revealed at all investigated time scales[235]. Furthermore, intracellular motion in the sub-diffusive regime is qualitatively distinct from overdamped Brownian motion. Negative correlations between increments of motion generate this sub-diffusive behavior. This suggests another class of Langevin-type models for the velocity, generating Gaussian fluctuations with correlations characteristic of an anti-persistent motion[139].

3.2 Dimensionality in intracellular transport

To reduce the complexity of the 3D cell interior, a quasi-1D cell system was realized by special surface treatment, confining cell adhesion to pre-patterned quasi-1D surface lines[236,242]. On these quasi-1D surface structures of 1 µm width, straight cellular outgrowth of up to several 100 µm was observed for PC12 cells[236]. Quasi-1D intracellular transport phases of inserted fluorescent nanoparticles (NPs) were analyzed by the two-state local MSD analysis as described in Section 2.1. Upon direct insertion of non-functionalized NPs into the cells, which could not bind to bio-motors for directed transport, sub-diffusive intracellular transport was predominant. However, this transport behavior reverses completely towards directed transport when attachment to bio-motors is possible. Thus, tuning the attachment rate to intracellular bio-motors is a useful tool to control the efficiency of intracellular transport processes[236].

To further investigate the aspects of dimensionality in intracellular transport, 3D trajectories of fluorescent NPs inside living cells were analyzed by local MSD calculation and compared to their 2D projections.[21] This way, the impact of

each dimension for directed transport and diffusion was identified. Two cell types were compared: *D. discoideum* cells exhibiting a rather 3D morphology during adhesion and migration and HUH7 cells that are rather flat (2D-like) when adhered to a flat substrate. It was found that directed transport along microtubules is performed isotropically in *D. discoideum* cells. Here, the projection of the transport trajectories into 2D showed significant deviations from 3D directed transport behavior. In contrast, the 2D projection of the directed phase trajectories did not result in a significant change in motion characteristics in the more 2D-organized HUH7 cells, where directed transport along MTs occurs predominantly in the 2D plane of adhesion. Diffusion coefficients obtained from 2D projections of the 3D tracks were underestimated in both cell types, proving that intracellular diffusion is a complex, anisotropic process in living cells with distinct 3D features[239].

3.3 Force application inside living cells by magnetic tweezers

The micro-viscoelasticity of the intracellular space of *D. discoideum* cells was studied by evaluating the intracellular transport of magnetic force probes and their viscoelastic responses to force pulses in the pN to nN regime[241,243]. Magnetic tweezer technology was applied by pulling super-paramagnetic micro- and nano-scaled particles inside cells *via* an inhomogeneous, external magnetic field[237,241,243].

The robustness of intracellular transport processes can be correlated with the resistance against external force application. In general, it was found that nN forces exerted on magnetic beads attached to microtubules (MTs) are balanced by traction forces. Those arise at the MT ends coupled to the actin cortex and the microtubule organising centre (MTOC), respectively. Mechanical coupling between the MTs and the viscoelastic actin cortex provides cells with high mechanical stability despite the softness of the cytoplasm. Stronger external

forces have to be balanced by the interplay of the traction forces in the MT network and the shear stress in the viscoelastic actin cortex[237].

Therefore, the cytoplasmic space of cells is an active body that is mechanically stabilized by interactive crosstalk between the viscoelastic shell and the aster-like array of microtubules embedded in the viscoplastic cytoplasmatic space[243]. External cues strongly influence these mechanisms and recent investigations showed that mechano-transduction also occurs in the nucleus and is therefore not only restricted to adhesion sites and cell surface receptors[244].

4. Control of cell motion by spatio-temporally controlled external chemical stimuli

The prime example of complex intracellular feedback on fast time scales is chemotaxis, the capability of cells to sense[20,245], polarise[132] and migrate towards an external chemical stimulus[20]. In this orchestrated process, chemoattractants bind to cell surface receptors and induce cell polarization and the subsequent generation of protrusions in the direction of the gradient (Figure 35)[246,247]. Chemotaxis is essential for embryogenesis[248], neuron guidance[249], and inflammatory response[25], but also in pathologic aberrations like metastasis[24,250]. Understanding the key mechanisms of chemotaxis will allow for active cell guidance. This will greatly facilitate artificial tissue formation in tissue engineering and novel approaches for regenerative medicine, *e.g.* by directing the migration of specific cell types towards defined regions inside 3D scaffolds. Additionally, the elucidation of chemotactic processes in metastasis might lead to the discovery of potential targets for tumor therapy.

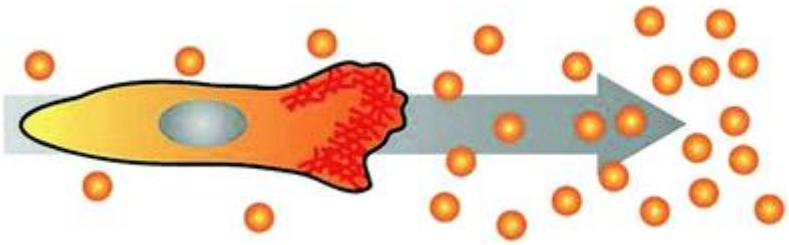

Figure 35: Cell polarising its actin cortex (red) towards the source of a chemical gradient and initiating directed migration.

Therefore, many recent developments in microfluidics aim at a better experimental setup to stimulate cells in highly controlled, spatio-temporally varying gradient fields. Micropipette[251,252] and diffusion chamber[253–255] assays are easily applicable methods to create chemical gradients, while for the generation of temporally stable gradients, chemical mixing in cascade microfluidic structures is applied experimentally[110,111,256]. Y-chambers even add the advantage of temporal on/off-switching[257,258]. For rapid chemotactic stimulation, photo-induced release of chemotactic agents was implemented[259–261]. However, this technique leads to temporal and local inhomogeneities.

4.1 Cell motion analysis in alternating gradient fields

The creation of realistic artificial cell environments needs both aspects: stable gradients and fast changes in the gradient direction. This was first achieved by a complex valve-based approach examining migratory responses of neutrophils to fast gradient variations[110]. An even higher stability accompanied by faster switching frequencies and a less complex setup is gained using a 3-inlet microfluidic gradient generator. This technique allows for the generation of highly stable, homogeneous gradients on large scales to address many cells in parallel[112]. The cells sense chemotactic fields arising from two opposite directions, which can be switched on alternatingly at any frequency, to adapt to the exposure times the cells experience in the currently applied chemotactic field. Two fundamentally different cell repolarization and migration types were identified during reorientation of *D. discoideum* cells towards the new gradient

directions: repolarization and U-turn behavior. Even dynamical cell trapping was performed at high gradient switching frequencies. Here, the cells could not follow the changing stimulus and therefore were trapped[112]. This can be used to probe the mechanistic time scales of the sensing abilities of cells.

Intracellular repolymerization dynamics visualized by the GFP fusion protein LimEΔcc in *D. discoideum* cells has been quantified by a fluorescence dipole moment correlating the direction of the actin front to the gradient direction (Figure 36). Repolymerization behavior involves reorganization of the actin cortex towards the new migration direction and the establishment of a new migration front at the opposite end of the cell[112]. The temporal evolution of this process is shown in Figure 36.

Future experiments need to combine these highly stable but temporarily variable gradient fields with further external stimuli and internal cell readouts to clarify the still remaining questions regarding chemotactically induced movement.

4.2 Influcence of cell shape on chemotaxis

Amoeboid cell motion in general occurs by cyclic formation of protrusions (pseudopods) at the cell front, followed by active retraction of the cell rear[107]. Cell shape changes have been investigated in more detail to extract optimal combinations of cell shape changes and migration behavior for the sensing of chemotactic fields at the sensing limit[262,263]. Results show that *D. discoideum* cells are capable of chemotaxis at the fundamental limit of gradient sensing, as predicted by a static absorber model[264]. This model shows that an amoeboid cell exhibits the same average sensing precision as a spherical object binding the chemoattractant permanently to its surface.

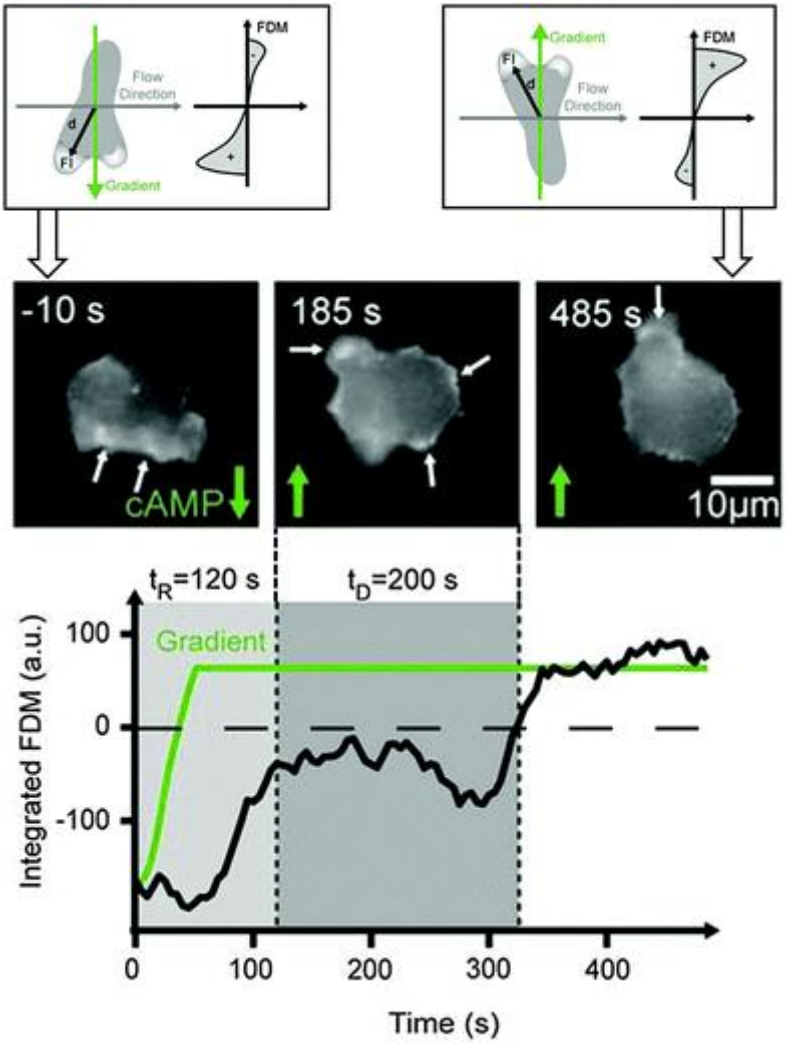

Figure 36: Schematic illustration of a cell polarising towards alternating gradient directions (top). Actin polymerization is quantified by LimEΔcc GFP and the fluorescence dipole moment (FDM) quantifies the amount of fluorescence in the upper versus the lower hemisphere of the cell during this reorientation process (bottom). Cell polarization (mid image gallery) and fluorescence dipole moment (black line in plot) following the gradient direction (green line in plot)[112].

Additional insight was gained about a windshield effect produced by the flow of a chemotactic medium across a cell. This effect interferes with accurate chemotaxis, but cells are capable of compensating for this effect, if it is caused by their own motion[264]. The highly correlated shapes and motion behaviors of amoeba are strategies for coping with such motion induced gradients at a low signal-to-noise-ratio in chemotaxis[103]. It was found that sideway sensing strategies fit with experimentally observed pseudopod splitting and zig-zag movement up the gradient[262]. Furthermore, a stopping and sensing strategy was revealed, exhibiting reduced speed accompanied by cell shape

oscillations[61]. A third strategy would be the compensation by chemoattractant secretion at the rear of the cell, which *D. discoideum* is known to do. Since similar cell behavior is observed in a diverse range of cell types[262], these could be conserved traits in evolution and could be used for medical applications, *e.g.* for guiding the migration of cell ensembles or immune cells by utilizing cell–cell signalling.

5. Cellular adhesion and motion control in predefined quasi-3D environments

In the absence of external cues, motile amoeboid cells migrate by the formation of stochastically generated pseudopods. The current model assumes two alternating motility modes: a random probing mode and a directed, fast migration mode[60]. This efficient "search strategy" is highly dynamic and can be characterized by distinct differences in the protrusion frequency and angle distribution of successive turns in the migration direction[61]. Cell velocity and shape analysis during these random migration phases led to simple models of amoeboid random walk[62]. In the last decade, a refined view emerged considering correlations between the cellular orientation and the migration direction[63–66]. In the presence of mechanical or chemical cues, the protrusions can be stabilized and trigger directed migration by cell polarization[67]. This specific type of cell migration is observed in several eukaryotic cell types, *e.g.* stem cells, specific immune cells or metastatic tumor cells[68], which can travel long distances inside the complex tissues of the human body to reach their point of destination[69]. Thus, a profound understanding of the mechanisms governing amoeboid migration in 3D environments will facilitate novel approaches in diagnostics and therapy. It will give rise to the development of novel drugs in cancer therapy, targeting specific cytoskeletal parts or intracellular proteins that have been shown to promote tumor metastasis. Furthermore, the abilities for cell guidance by topographic cues will be of

utmost importance for the 3D distribution of cells inside artificial scaffolds in tissue engineering.

5.1 Cell-substrate interactions in amoeboid migration

Spontaneous generation of pseudopods at random sites is a basic activity of vital cells and can be found in homogeneous cell migration environments lacking topographic and chemotactic stimuli. *D. discoideum* cells perform a special kind of random motion consisting of zig-zag-like motions over distances of about 20 µm and a subsequent change in the direction[61,70,71]. This motion behavior is correlated with the dynamics of pseudopod spreading. Pseudopods protrude constantly for several microns and stop abruptly. Then, the cell rear is retracted by unbinding from the substrate, decreasing the contact area. Subsequently, migration in a new direction is induced. Hence, cell motion is characterized by a concomitant cyclic variation of the contact area[70].

The influence of surface structure and chemistry on this type of cell dynamics in *D. discoideum* cells during adhesion has been investigated quantitatively for different actin manipulating proteins by tracking the cell adhesion area and the protein distribution during the adhesion process[66,67,68,69,71,61–66] The analysis of the gain and loss of contact area revealed fluctuations in forces of protrusion and retraction that prevent *D. discoideum* cells from approaching a steady-state of interaction with a substrate. In conclusion, non-monotonic cell spreading is induced by spatio-temporal patterns resulting from the interplay of motor proteins and regulatory proteins, either promoting or terminating the polymerization of actin[66].

The importance of substrate adhesion and interaction was stressed by investigations on the size and number of actin foci in *D. discoideum*, where a negative correlation between the actin foci number and the cell velocity was found[72]. Thus, amoeboid cell motility strongly depends on the interaction with

the substrate. This is a very important principle for future studies and potential applications, as similar correlations between focal adhesion dynamics and cell motility have been found for other types of cell migration[73].

5.2 Influence of quasi-3D structures on amoeboid cell motility

3D structures influence adhesion and migration behavior of living cells by inducing local and global changes in cellular morphology and protein expression[55,226,265].

To analyse differences in cell migration in 3D structured environments *versus* on flat substrates (2D), the motion behavior of *D. discoideum* cells has been investigated in micro-pillar arrays with defined geometry and density[60,138]. Results elucidate that microstructures on surfaces are not sensed as simple obstacles, leading to a deflection of the cell path, but can trap cells in contact with these structures and stop cell motion. This dynamic cell trapping effect depends on the cell's initial motility mode, which is enhanced with increasing number of surface structures the cell is in contact with at a given time (Figure 37)[60,138].

Additionally, switching from a randomly formed pseudopod (random motility mode) into a stabilized pseudopod (directed migration) is enhanced by surface contact, meaning that cells migrate by maximising contact with available surface structures. However, cells lacking microtubules do not show pronounced attraction to surface pillars, leading to the conclusion that microtubules mediate cellular interaction with surface structures[60]. The general dependence of focal adhesion build-up and disassembly on microtubules has also been observed in fibroblasts[266,267] and proves the relevance of the principles derived from investigations on amoeboid cells.

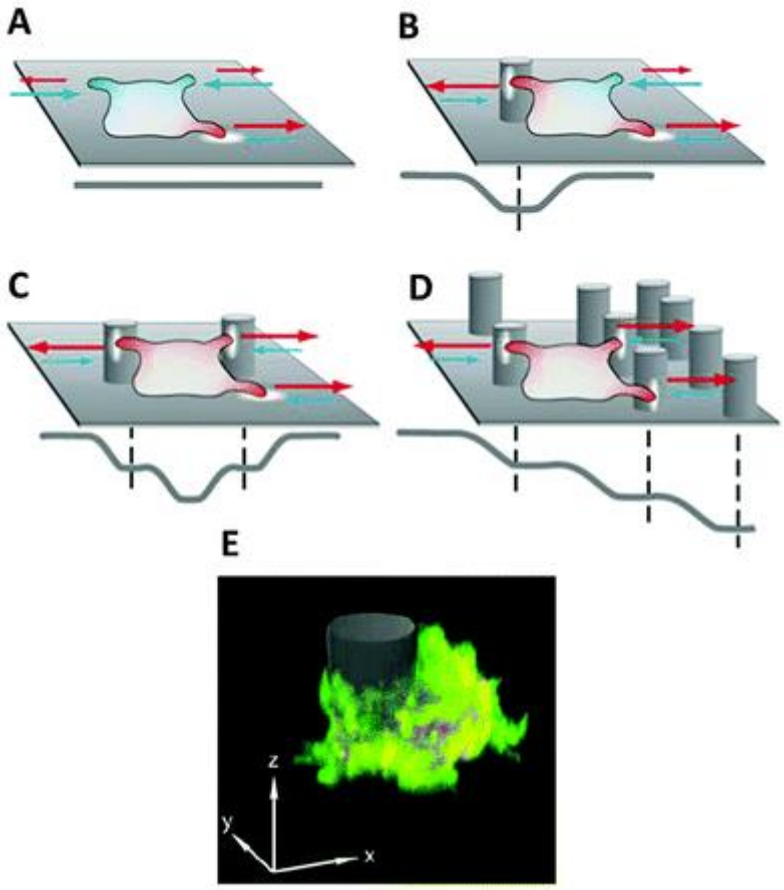

Figure 37: Schematic illustration of cell behavior on differently structured substrates, characterized by protrusion spreading (red) and retraction (blue), where extracellular obstacles can be described as potential wells mediating cellular motion processes; the resulting potential level is displayed in grey: (A) random protrusion formation on flat substrates, (B) protrusion stabilization and subsequent adhesion to the additional surface contact with 3D structures, (C) dynamic cell trapping effect by adhesion to multiple 3D structures in the absence of other structures in the cell vicinity, (D) topographic guidance effect by a gradual increase of the adhesion surface, (E) fluorescent microscopy image of a D. discoideum cell expressing LimEΔcc RFP and Arp2/3-GFP while adhering to a pillar structure.

Further investigations revealed that the spatial density of the quasi-3D environment has a distinct effect on cell migration, *e.g.* the number of directed pillar-to-pillar runs is increased by higher pillar densities, triggering cell polarization[60,138]. A long-term shift of cell migration towards regions with pillar distances in the range of the cell diameter was observed. This effect is based on directed migration from low density regions and a contrary passive drift from high density regions where cells are spatially confined[65]. This "topophoresis" effect opens the possibility of guiding or sorting different cell types according to the spatial geometry and density of the 3D environment. Additionally, in *D. discoideum* cells exposed to traction forces by 3D spatial confinement, a

transition from actin-driven pseudopod formation towards bleb-driven motility can be observed[252]. Interestingly, the migration of mesenchymal-like cells shows a plasticity depending on the adhesion to the substrate and spatial confinement. They exhibited a tendency to perform amoeboid-like migration for low substrate adhesion and spatial confinement inside artificial environments[252]. This finding underlines the importance of amoeboid migration for the development of novel materials for cell guidance in tissue engineering.

6. Outlook

This review summarizes recent research on the influence of chemical and mechanical stimuli on cell behavior and the underlying processes, with a focus on amoeboid migration. The survival of cells in organisms depends on their ability to respond to external cues with changes in their intracellular signalling pathways. The extraction of these state changes from intracellular motion data will serve as a novel readout tool for the precise analysis of cell interactions with materials and active agents, e.g. for more efficient screening assays in drug development.

Future research should aim at advancing the mechanistic understanding of the complex interplay of extracellular cues and intracellular states in setups combining mechanical and chemical stimuli in 3D, successively approaching physiological conditions. The systematic analysis and elucidation of these interactions will greatly facilitate the buildup of a toolbox for the design of cell-type specific surface structures and 3D scaffolds and initiate novel approaches in biomedical research. The crucial step here is to optimize the combination of stimuli for manipulating cell functions with bioactive materials, ranging in size from the micron to the nanoscale. Mechanical stimuli will be provided by 3D scaffolds to promote or hinder directed cell migration, guiding cells to desired destinations and providing ideal conditions for specific cell types. To enhance

these effects, local chemotactic gradients will be generated inside the scaffolds by incorporated nanocarriers, altering the cytoskeleton or triggering local changes in cell functions.

The presented approach mimics the amount of information a cell has to compute *in vivo* and will elucidate the decision making process in living cells. This will be greatly facilitated by computational studies, helping to find consistent biophysical models for cellular behavior[268,269]. In a greater scheme, this will allow for the design of more realistic drug screening assays, organs-on-a-chip, bioactive scaffolds and open up new prospects for applications in tissue engineering and regenerative medicine.

VIII. REFERENCES

(1) Tageja, N. Bridging the translation gap - new hopes, new challenges. *Fundamental & clinical pharmacology* **2011**, *25* (2), 163–171. DOI: 10.1111/j.1472-8206.2010.00903.x.

(2) Pampaloni, F.; Reynaud, E. G.; Stelzer, E. H. K. The third dimension bridges the gap between cell culture and live tissue. *Nature reviews. Molecular cell biology* **2007**, *8* (10), 839–845. DOI: 10.1038/nrm2236.

(3) Doke, S. K.; Dhawale, S. C. Alternatives to animal testing: A review. *Saudi pharmaceutical journal : SPJ : the official publication of the Saudi Pharmaceutical Society* **2015**, *23* (3), 223–229. DOI: 10.1016/j.jsps.2013.11.002.

(4) Bailey, J.; Balls, M. Recent efforts to elucidate the scientific validity of animal-based drug tests by the pharmaceutical industry, pro-testing lobby groups, and animal welfare organisations. *BMC Medical Ethics* **2019**, *20.* DOI: 10.1186/s12910-019-0352-3.

(5) Jaroch, K.; Jaroch, A.; Bojko, B. Cell cultures in drug discovery and development: The need of reliable in vitro-in vivo extrapolation for pharmacodynamics and pharmacokinetics assessment. *Journal of pharmaceutical and biomedical analysis* **2018**, *147*, 297–312. DOI: 10.1016/j.jpba.2017.07.023.

(6) Langhans, S. A. Three-Dimensional in Vitro Cell Culture Models in Drug Discovery and Drug Repositioning. *Frontiers in pharmacology* **2018**, *9*, 6. DOI: 10.3389/fphar.2018.00006.

(7) Adiga, S. P.; Jin, C.; Curtiss, L. A.; Monteiro-Riviere, N. A.; Narayan, R. J. Nanoporous membranes for medical and biological applications. *Wiley interdisciplinary reviews. Nanomedicine and nanobiotechnology* **2009**, *1* (5), 568–581. DOI: 10.1002/wnan.50.

(8) Rambani, R.; Kepecs, D. M.; Mäkinen, T. J.; Safir, O. A.; Gross, A. E.; Kuzyk, P. R. Revision Total Hip Arthroplasty for Fractured Ceramic Bearings:A Review of Best Practices for Revision Cases. *The Journal of arthroplasty* **2017**, *32* (6), 1959–1964. DOI: 10.1016/j.arth.2016.12.050.

(9) Teo, W. Z. W.; Schalock, P. C. Metal Hypersensitivity Reactions to Orthopedic Implants. *Dermatology and therapy* **2017**, *7* (1), 53–64. DOI: 10.1007/s13555-016-0162-1.

(10) Cheung, A. C.; Banerjee, S.; Cherian, J. J.; Wong, F.; Butany, J.; Gilbert, C.; Overgaard, C.; Syed, K.; Zywiel, M. G.; Jacobs, J. J.; Mont, M. A. Systemic cobalt toxicity from total hip arthroplasties:Review of a rare condition Part 1 - history, mechanism, measurements, and pathophysiology. *The bone & joint journal* **2016**, *98-B* (1), 6–13. DOI: 10.1302/0301-620X.98B1.36374.

(11) Gallo, J.; Goodman, S. B.; Konttinen, Y. T.; Raska, M. Particle disease:Biologic mechanisms of periprosthetic osteolysis in total hip arthroplasty. *Innate immunity* **2013**, *19* (2), 213–224. DOI: 10.1177/1753425912451779.

(12) Palchesko, R. N.; Zhang, L.; Sun, Y.; Feinberg, A. W. Development of polydimethylsiloxane substrates with tunable elastic modulus to study cell mechanobiology in muscle and nerve. *PloS one* **2012**, *7* (12), e51499. DOI: 10.1371/journal.pone.0051499.

(13) Steinberg, T.; Schulz, S.; Spatz, J. P.; Grabe, N.; Mussig, E.; Kohl, A.; Komposch, G.; Tomakidi, P. Early keratinocyte differentiation on micropillar interfaces. *Nano letters* **2007**, *7* (2), 287–294. DOI: 10.1021/nl062271z.

(14) Raper, K. B. Dictyostelium discoideum, a new species of slime mold from decaying forest leaves. *J. Agric. Res.* **1935** (50), 135–147.

(15) Kursawe, M.; Glaubitt, W.; Thierauf, A. Biodegradable Silica Fibers from Sols. *Journal of Sol-Gel Science and Technology* **1998**, *13* (1/3), 267–271. DOI: 10.1023/A:1008651505705.

(16) Müller, R.; Anders, N.; Titus, J.; Enke, D. Ultra-thin porous glass membranes--an innovative material for the immobilization of active species for optical chemosensors. *Talanta* **2013**, *107*, 255–262. DOI: 10.1016/j.talanta.2012.12.038.

(17) Loverdo, C.; Bénichou, O.; Moreau, M.; Voituriez, R. Enhanced reaction kinetics in biological cells. *Nature Physics* **2008**, *4* (2), 134–137. DOI: 10.1038/nphys830.

(18) Pollard, T. D.; Borisy, G. G. Cellular Motility Driven by Assembly and Disassembly of Actin Filaments. *Cell* **2003**, *112* (4), 453–465. DOI: 10.1016/S0092-8674(03)00120-X.

(19) Caspi, A.; Granek, R.; Elbaum, M. Enhanced diffusion in active intracellular transport. *Physical review letters* **2000**, *85* (26 Pt 1), 5655–5658. DOI: 10.1103/PhysRevLett.85.5655.

(20) Parent, C. A. A Cell's Sense of Direction. *Science* **1999**, *284* (5415), 765–770. DOI: 10.1126/science.284.5415.765.

(21) Fletcher, D. A.; Mullins, R. D. Cell mechanics and the cytoskeleton. *Nature* **2010**, *463* (7280), 485–492. DOI: 10.1038/nature08908.

(22) Williamson, T. L.; Cleveland, D. W. Slowing of axonal transport is a very early event in the toxicity of ALS-linked SOD1 mutants to motor neurons. *Nature neuroscience* **1999**, *2* (1), 50–56. DOI: 10.1038/4553.

(23) Hafezparast, M.; Klocke, R.; Ruhrberg, C.; Marquardt, A.; Ahmad-Annuar, A.; Bowen, S.; Lalli, G.; Witherden, A. S.; Hummerich, H.; Nicholson, S.; Morgan, P. J.; Oozageer, R.; Priestley, J. V.; Averill, S.; King, V. R.; Ball, S.; Peters, J.; Toda, T.; Yamamoto, A.; Hiraoka, Y.; Augustin, M.; Korthaus, D.; Wattler, S.; Wabnitz, P.; Dickneite, C.; Lampel, S.; Boehme, F.; Peraus, G.; Popp, A.; Rudelius, M.; Schlegel, J.; Fuchs, H.; Hrabe de Angelis, M.; Schiavo, G.; Shima, D. T.; Russ, A. P.; Stumm, G.; Martin, J. E.; Fisher, E. M. C. Mutations in dynein link motor neuron degeneration to defects in retrograde transport. *Science (New York, N.Y.)* **2003**, *300* (5620), 808–812. DOI: 10.1126/science.1083129.

(24) Coultas, L.; Chawengsaksophak, K.; Rossant, J. Endothelial cells and VEGF in vascular development. *Nature* **2005**, *438* (7070), 937–945. DOI: 10.1038/nature04479.

(25) Martin, P.; Leibovich, S. J. Inflammatory cells during wound repair: the good, the bad and the ugly. *Trends in cell biology* **2005**, *15* (11), 599–607. DOI: 10.1016/j.tcb.2005.09.002.

(26) Tracy, L. E.; Minasian, R. A.; Caterson, E. J. Extracellular Matrix and Dermal Fibroblast Function in the Healing Wound. *Advances in wound care* **2016**, *5* (3), 119–136. DOI: 10.1089/wound.2014.0561.

(27) Harper, P. A.; Juliano, R. L. Two distinct mechanisms of fibroblast adhesion. *Nature* **1981**, *290* (5802), 136–138. DOI: 10.1038/290136a0.

(28) Sharma, A.; Mori, T.; Mahnen, C. J.; Everson, H. R.; Leslie, M. T.; Nielsen, A. D.; Lussier, L.; Zhu, C.; Malcuit, C.; Hegmann, T.; McDonough, J. A.; Freeman, E. J.; Korley, L. T. J.; Clements, R. J.; Hegmann, E. Effects of Structural Variations on the Cellular Response and Mechanical Properties of Biocompatible, Biodegradable, and Porous Smectic Liquid Crystal Elastomers. *Macromolecular bioscience* **2017**, *17* (2). DOI: 10.1002/mabi.201600278.

(29) Frantz, C.; Stewart, K. M.; Weaver, V. M. The extracellular matrix at a glance. *Journal of cell science* **2010**, *123* (Pt 24), 4195–4200. DOI: 10.1242/jcs.023820.

(30) Woods, A.; Wang, G.; Beier, F. Regulation of chondrocyte differentiation by the actin cytoskeleton and adhesive interactions. *Journal of cellular physiology* **2007**, *213* (1), 1–8. DOI: 10.1002/jcp.21110.

(31) McKee, T. J.; Perlman, G.; Morris, M.; Komarova, S. V. Extracellular matrix composition of connective tissues: a systematic review and meta-analysis. *Scientific reports* **2019**, *9* (1), 10542. DOI: 10.1038/s41598-019-46896-0.

(32) Wang, C.-C.; Jamal, L.; Janes, K. A. Normal morphogenesis of epithelial tissues and progression of epithelial tumors. *Wiley interdisciplinary reviews. Systems biology and medicine* **2011**, *4* (1), 51–78. DOI: 10.1002/wsbm.159.

(33) Kato, Y.; Miyakawa, T.; Tanokura, M. Overview of the mechanism of cytoskeletal motors based on structure. *Biophysical reviews* **2018**, *10* (2), 571–581. DOI: 10.1007/s12551-017-0368-1.

(34) Petry, S. Mechanisms of Mitotic Spindle Assembly. *Annual review of biochemistry* **2016**, *85*, 659–683. DOI: 10.1146/annurev-biochem-060815-014528.

(35) Herrmann, H.; Bär, H.; Kreplak, L.; Strelkov, S. V.; Aebi, U. Intermediate filaments: from cell architecture to nanomechanics. *Nature reviews. Molecular cell biology* **2007**, *8* (7), 562–573. DOI: 10.1038/nrm2197.

(36) Herrmann, H.; Strelkov, S. V.; Burkhard, P.; Aebi, U. Intermediate filaments: primary determinants of cell architecture and plasticity. *The Journal of clinical investigation* **2009**, *119* (7), 1772–1783. DOI: 10.1172/JCI38214.

(37) Embl. *Picture Release - Press Release - EMBL*. https://www.embl.de/aboutus/communication_outreach/media_relations/2008/081203_heidelberg-pic/ (accessed 2020-10-15.222Z).

(38) Friedl, P.; Borgmann, S.; Bröcker, E. B. Amoeboid leukocyte crawling through extracellular matrix:Lessons from the Dictyostelium paradigm of cell movement. *Journal of leukocyte biology* **2001**, *70* (4), 491–509.

(39) Gurtner, G. C.; Werner, S.; Barrandon, Y.; Longaker, M. T. Wound repair and regeneration. *Nature* **2008**, *453* (7193), 314–321. DOI: 10.1038/nature07039.

(40) Hanna, J. R.; Giacopelli, J. A. A review of wound healing and wound dressing products. *The Journal of foot and ankle surgery : official publication of the American College of Foot and Ankle Surgeons* **1997**, *36* (1), 2-14; discussion 79.

(41) Wilgus, T. A. Immune cells in the healing skin wound:Influential players at each stage of repair. *Pharmacological research* **2008**, *58* (2), 112–116. DOI: 10.1016/j.phrs.2008.07.009.

(42) Khalili, A. A.; Ahmad, M. R. A Review of Cell Adhesion Studies for Biomedical and Biological Applications. *International journal of molecular sciences* **2015**, *16* (8), 18149–18184. DOI: 10.3390/ijms160818149.

(43) Bentley, K. L.; Klebe, R. J. Fibronectin binding properties of bacteriologic petri plates and tissue culture dishes. *Journal of biomedical materials research* **1985**, *19* (7), 757–769. DOI: 10.1002/jbm.820190704.

(44) Wood, W.; Martin, P. Structures in focus—filopodia. *The International Journal of Biochemistry & Cell Biology* **2002**, *34* (7), 726–730. DOI: 10.1016/S1357-2725(01)00172-8.

(45) Mattila, P. K.; Lappalainen, P. Filopodia:Molecular architecture and cellular functions. *Nature reviews. Molecular cell biology* **2008**, *9* (6), 446–454. DOI: 10.1038/nrm2406.

(46) Heckman, C. A.; Plummer, H. K. Filopodia as sensors. *Cellular signalling* **2013**, *25* (11), 2298–2311. DOI: 10.1016/j.cellsig.2013.07.006.

(47) Altay, G.; Larrañaga, E.; Tosi, S.; Barriga, F. M.; Batlle, E.; Fernández-Majada, V.; Martínez, E. Self-organized intestinal epithelial monolayers in crypt and villus-like domains show effective barrier function. *Scientific reports* **2019**, *9* (1), 10140. DOI: 10.1038/s41598-019-46497-x.

(48) Choi, N. W.; Cabodi, M.; Held, B.; Gleghorn, J. P.; Bonassar, L. J.; Stroock, A. D. Microfluidic scaffolds for tissue engineering. *Nature materials* **2007**, *6* (11), 908. DOI: 10.1038/nmat2022.

(49) Lee, J. Y.; Schmidt, C. E. Pyrrole-hyaluronic acid conjugates for decreasing cell binding to metals and conducting polymers. *Acta biomaterialia* **2010**, *6* (11), 4396–4404. DOI: 10.1016/j.actbio.2010.06.011.

(50) Okeyo, K. O.; Kurosawa, O.; Yamazaki, S.; Oana, H.; Kotera, H.; Nakauchi, H.; Washizu, M. Cell Adhesion Minimization by a Novel Mesh Culture Method Mechanically Directs Trophoblast Differentiation and Self-Assembly Organization of Human Pluripotent Stem Cells. *Tissue engineering. Part C, Methods* **2015**, *21* (10), 1105–1115. DOI: 10.1089/ten.TEC.2015.0038.

(51) Jones, M. C.; Zha, J.; Humphries, M. J. Connections between the cell cycle, cell adhesion and the cytoskeleton. *Philosophical transactions of the Royal Society of London. Series B, Biological sciences* **2019**, *374* (1779), 20180227. DOI: 10.1098/rstb.2018.0227.

(52) Jongsma, M. L. M.; Berlin, I.; Neefjes, J. On the move: organelle dynamics during mitosis. *Trends in cell biology* **2015**, *25* (3), 112–124. DOI: 10.1016/j.tcb.2014.10.005. Published Online: Nov. 18, 2014.

(53) Gérard, C.; Goldbeter, A. The balance between cell cycle arrest and cell proliferation: control by the extracellular matrix and by contact inhibition. *Interface focus* **2014**, *4* (3), 20130075. DOI: 10.1098/rsfs.2013.0075.

(54) Malumbres, M.; Barbacid, M. Cell cycle, CDKs and cancer: a changing paradigm. *Nature reviews. Cancer* **2009**, *9* (3), 153–166. DOI: 10.1038/nrc2602.

(55) Charras, G.; Sahai, E. Physical influences of the extracellular environment on cell migration. *Nature reviews. Molecular cell biology* **2014**, *15* (12), 813–824. DOI: 10.1038/nrm3897.

(56) Croker, B. A.; Lawson, B. R.; Rutschmann, S.; Berger, M.; Eidenschenk, C.; Blasius, A. L.; Moresco, E. M. Y.; Sovath, S.; Cengia, L.; Shultz, L. D.; Theofilopoulos, A. N.; Pettersson, S.; Beutler, B. A. Inflammation and autoimmunity caused by a SHP1 mutation depend on IL-1, MyD88, and a microbial trigger. *Proceedings of the National Academy of Sciences of the United States of America* **2008**, *105* (39), 15028–15033. DOI: 10.1073/pnas.0806619105.

(57) Rosenblum, M. D.; Remedios, K. A.; Abbas, A. K. Mechanisms of human autoimmunity. *The Journal of clinical investigation* **2015**, *125* (6), 2228–2233. DOI: 10.1172/JCI78088.

(58) Bravo-Cordero, J. J.; Hodgson, L.; Condeelis, J. Directed cell invasion and migration during metastasis. *Current opinion in cell biology* **2012**, *24* (2), 277–283. DOI: 10.1016/j.ceb.2011.12.004.

(59) Panková, K.; Rösel, D.; Novotný, M.; Brábek, J. The molecular mechanisms of transition between mesenchymal and amoeboid invasiveness in tumor cells. *Cellular and molecular life sciences : CMLS* **2010**, *67* (1), 63–71. DOI: 10.1007/s00018-009-0132-1.

(60) Arcizet, D.; Capito, S.; Gorelashvili, M.; Leonhardt, C.; Vollmer, M.; Youssef, S.; Rappl, S.; Heinrich, D. Contact-controlled amoeboid motility induces dynamic cell trapping in 3D-microstructured surfaces. *Soft matter* **2012**, *8* (5), 1473–1481. DOI: 10.1039/c1sm05615h.

(61) Li, L.; Nørrelykke, S. F.; Cox, E. C. Persistent cell motion in the absence of external signals:A search strategy for eukaryotic cells. *PloS one* **2008**, *3* (5), e2093. DOI: 10.1371/journal.pone.0002093.

(62) van Haastert, P. J. M. A model for a correlated random walk based on the ordered extension of pseudopodia. *PLoS computational biology* **2010**, *6* (8). DOI: 10.1371/journal.pcbi.1000874.

(63) Kemkemer, R.; Jungbauer, S.; Kaufmann, D.; Gruler, H. Cell orientation by a microgrooved substrate can be predicted by automatic control theory. *Biophysical journal* **2006**, *90* (12), 4701–4711. DOI: 10.1529/biophysj.105.067967.

(64) Kaiser, J.-P.; Reinmann, A.; Bruinink, A. The effect of topographic characteristics on cell migration velocity. *Biomaterials* **2006**, *27* (30), 5230–5241. DOI: 10.1016/j.biomaterials.2006.06.002.

(65) Del Alamo, J. C.; Meili, R.; Alonso-Latorre, B.; Rodríguez-Rodríguez, J.; Aliseda, A.; Firtel, R. A.; Lasheras, J. C. Spatio-temporal analysis of eukaryotic cell motility by improved force cytometry. *Proceedings of the National Academy of Sciences of the United States of America* **2007**, *104* (33), 13343–13348. DOI: 10.1073/pnas.0705815104.

(66) Heinrich, D.; Youssef, S.; Schroth-Diez, B.; Engel, U.; Aydin, D.; Blümmel, J.; Spatz, J. P.; Gerisch, G. Actin-cytoskeleton dynamics in non-monotonic cell spreading. *Cell Adhesion & Migration* **2008**, *2* (2), 58–68. DOI: 10.4161/cam.2.2.6190.

(67) Nabi, I. R. The polarization of the motile cell. *Journal of cell science* **1999**, *112 (Pt 12)*, 1803–1811.

(68) Friedl, P. Prespecification and plasticity:Shifting mechanisms of cell migration. *Current opinion in cell biology* **2004**, *16* (1), 14–23. DOI: 10.1016/j.ceb.2003.11.001.

(69) La Rosa, G. de; Longo, N.; Rodríguez-Fernández, J. L.; Puig-Kroger, A.; Pineda, A.; Corbí, A. L.; Sánchez-Mateos, P. Migration of human blood dendritic cells across endothelial cell monolayers: adhesion molecules and chemokines involved in subset-specific transmigration. *Journal of leukocyte biology* **2003**, *73* (5), 639–649. DOI: 10.1189/jlb.1002516.

(70) Sackmann, E.; Keber, F.; Heinrich, D. Physics of Cellular Movements. *Annu. Rev. Condens. Matter Phys.* **2010**, *1* (1), 257–276. DOI: 10.1146/annurev-conmatphys-070909-104105.

(71) Schindl, M.; Wallraff, E.; Deubzer, B.; Witke, W.; Gerisch, G.; Sackmann, E. Cell-substrate interactions and locomotion of Dictyostelium wild-type and mutants defective in three cytoskeletal proteins: a study using quantitative reflection interference contrast microscopy. *Biophysical journal* **1995**, *68* (3), 1177–1190. DOI: 10.1016/S0006-3495(95)80294-8.

(72) Uchida, K. S. K.; Yumura, S. Dynamics of novel feet of Dictyostelium cells during migration. *Journal of cell science* **2004**, *117* (Pt 8), 1443–1455. DOI: 10.1242/jcs.01015.

(73) Kim, D.-H.; Wirtz, D. Focal adhesion size uniquely predicts cell migration. *FASEB journal : official publication of the Federation of American Societies for Experimental Biology* **2013**, *27* (4), 1351–1361. DOI: 10.1096/fj.12-220160.

(74) Jaenisch, R.; Bird, A. Epigenetic regulation of gene expression: how the genome integrates intrinsic and environmental signals. *Nature genetics* **2003**, *33 Suppl*, 245–254. DOI: 10.1038/ng1089.

(75) Edwards, T. M.; Myers, J. P. Environmental exposures and gene regulation in disease etiology. *Environmental health perspectives* **2007**, *115* (9), 1264–1270. DOI: 10.1289/ehp.9951.

(76) Romero, I. G.; Ruvinsky, I.; Gilad, Y. Comparative studies of gene expression and the evolution of gene regulation. *Nature reviews. Genetics* **2012**, *13* (7), 505–516. DOI: 10.1038/nrg3229.

(77) Caplan, A. I.; Bruder, S. P. Mesenchymal stem cells:Building blocks for molecular medicine in the 21st century. *Trends in molecular medicine* **2001**, *7* (6), 259–264.

(78) McKee, C.; Chaudhry, G. R. Advances and challenges in stem cell culture. *Colloids and surfaces. B, Biointerfaces* **2017**, *159*, 62–77. DOI: 10.1016/j.colsurfb.2017.07.051.

(79) Acikgoz, C.; Hempenius, M. A.; Huskens, J.; Vancso, G. J. Polymers in conventional and alternative lithography for the fabrication of nanostructures. *European Polymer Journal* **2011**, *47* (11), 2033–2052. DOI: 10.1016/j.eurpolymj.2011.07.025.

(80) Tran, K. T.; Nguyen, T. D. Lithography-based methods to manufacture biomaterials at small scales. *Journal of Science: Advanced Materials and Devices* **2017**, *2* (1), 1–14. DOI: 10.1016/j.jsamd.2016.12.001.

(81) Babul Singh. *Silicones Market Research with COVID-19 | DowDuPont, China National Bluestar (Group), KCC*. https://primefeed.in/news/4266672/silicones-market-research-with-covid-19-dowdupont-china-national-bluestar-group-kcc/ (accessed 2021-07-27).

(82) Sébastien Cargou. Introduction about soft-lithography for microfluidics. *Elveflow* **2020**.

(83) Danks, A. E.; Hall, S. R.; Schnepp, Z. The evolution of 'sol–gel' chemistry as a technique for materials synthesis. *Mater. Horiz.* **2016**, *3* (2), 91–112. DOI: 10.1039/C5MH00260E.

(84) Livage, J. Basic Principles of Sol-Gel Chemistry. *ChemInform* **2006**, *37* (7). DOI: 10.1002/chin.200607233.

(85) Biswas, A.; Friend, C. S.; Prasad, P. N. Ceramic Nanocomposites with Organic Phases, Optics of. In *Encyclopedia of materials*:*Science and technology*; Buschow, K. H. J., Ed.; Elsevier, 2001; pp 1072–1080. DOI: 10.1016/B0-08-043152-6/00198-4.

(86) Taylor, S. R. Coatings for Corrosion Protection: Inorganic. In *Encyclopedia of materials*:*Science and technology*; Buschow, K. H. J., Ed.; Elsevier, 2001; pp 1263–1269. DOI: 10.1016/B0-08-043152-6/00238-2.

(87) Innocenzi, P. Understanding sol–gel transition through a picture. A short tutorial. *Journal of Sol-Gel Science and Technology* **2020**, *94* (3), 544–550. DOI: 10.1007/s10971-020-05243-w.

(88) Enke, D.; Janowski, F.; Schwieger, W. Porous glasses in the 21st century––a short review. *Microporous and Mesoporous Materials* **2003**, *60* (1-3), 19–30. DOI: 10.1016/S1387-1811(03)00329-9.

(89) Inayat, A.; Reinhardt, B.; Herwig, J.; Küster, C.; Uhlig, H.; Krenkel, S.; Raedlein, E.; Enke, D. Recent advances in the synthesis of hierarchically porous silica materials

on the basis of porous glasses. *New J. Chem.* **2016**, *40* (5), 4095–4114. DOI: 10.1039/C5NJ03591K.

(90) Ferdinand Somorowsky. Entwicklung von nanoporösen Gläsern mit kontrollierten Sorptionseigenschaften zur Verbesserung des Innenraumklimas. Dissertation, Universität Würzburg, 2016.

(91) Kickelbick, G. *Hybrid Materials*; Wiley-VCH, 2007.

(92) Braga, M. S.; Gomes, O. F.; Jaimes, R. F. V. V.; Braga, E. R.; Borysow, W.; Salcedo, W. J. Multispectral colorimetric portable system for detecting metal ions in liquid media. In *2019 4th International Symposium on Instrumentation Systems, Circuits and Transducers (INSCIT)*; Staff, I., Ed.; IEEE: Piscataway, 2019; pp 1–6. DOI: 10.1109/INSCIT.2019.8868861.

(93) Stockert, J. C.; Blázquez-Castro, A. *Fluorescence Microscopy In Life Sciences*, 1st ed.; Bentham Science Publishers, 2017.

(94) Recillas-Targa, F. Multiple Strategies for Gene Transfer, Expression, Knockdown, and Chromatin Influence in Mammalian Cell Lines and Transgenic Animals. *MB* **2006**, *34* (3), 337–354. DOI: 10.1385/MB:34:3:337.

(95) Chalfie, M.; Tu, Y.; Euskirchen, G.; Ward, W. W.; Prasher, D. C. Green fluorescent protein as a marker for gene expression. *Science (New York, N.Y.)* **1994**, *263* (5148), 802–805. DOI: 10.1126/science.8303295.

(96) Specht, E. A.; Braselmann, E.; Palmer, A. E. A Critical and Comparative Review of Fluorescent Tools for Live-Cell Imaging. *Annual review of physiology* **2017**, *79*, 93–117. DOI: 10.1146/annurev-physiol-022516-034055.

(97) *What is the difference between fluorescence, phosphorescence and luminescence?* https://www.enzolifesciences.com/science-center/technotes/2019/december/what-is-the-difference-between-fluorescence-phosphorescence-and-luminescence?/ (accessed 2021-04-01.191Z).

(98) Colding-christensen, C. S. From Fluorophores to Filters: A guide to Fluorescence Microscopy. *Science Squared Ltd,* Apr 18, 2017. https://

bitesizebio.com/33529/fluorescence-microscopy-the-magic-of-fluorophores-and-filters/ (accessed 2021-04-02.820Z).

(99) Saxton, M. J.; Jacobson, K. Single-particle tracking: applications to membrane dynamics. *Annual review of biophysics and biomolecular structure* **1997**, *26*, 373–399. DOI: 10.1146/annurev.biophys.26.1.373.

(100) Evans, E. New physical concepts for cell amoeboid motion. *Biophysical journal* **1993**, *64* (4), 1306–1322. DOI: 10.1016/S0006-3495(93)81497-8.

(101) Fisher, P. R.; Merkl, R.; Gerisch, G. Quantitative analysis of cell motility and chemotaxis in Dictyostelium discoideum by using an image processing system and a novel chemotaxis chamber providing stationary chemical gradients. *The Journal of cell biology* **1989**, *108* (3), 973–984.

(102) Iwadate, Y.; Yumura, S. Actin-based propulsive forces and myosin-II-based contractile forces in migrating Dictyostelium cells. *Journal of cell science* **2008**, *121* (Pt 8), 1314–1324. DOI: 10.1242/jcs.021576.

(103) Maeda, Y. T.; Inose, J.; Matsuo, M. Y.; Iwaya, S.; Sano, M. Ordered patterns of cell shape and orientational correlation during spontaneous cell migration. *PloS one* **2008**, *3* (11), e3734. DOI: 10.1371/journal.pone.0003734.

(104) Bénichou, O.; Loverdo, C.; Moreau, M.; Voituriez, R. Two-dimensional intermittent search processes:An alternative to Lévy flight strategies. *Physical review. E, Statistical, nonlinear, and soft matter physics* **2006**, *74* (2 Pt 1), 20102. DOI: 10.1103/PhysRevE.74.020102.

(105) Dalous, J.; Burghardt, E.; Müller-Taubenberger, A.; Bruckert, F.; Gerisch, G.; Bretschneider, T. Reversal of cell polarity and actin-myosin cytoskeleton reorganization under mechanical and chemical stimulation. *Biophysical journal* **2008**, *94* (3), 1063–1074. DOI: 10.1529/biophysj.107.114702.

(106) Devreotes, P. N.; Zigmond, S. H. Chemotaxis in eukaryotic cells:A focus on leukocytes and Dictyostelium. *Annual review of cell biology* **1988**, *4*, 649–686. DOI: 10.1146/annurev.cb.04.110188.003245.

(107) Ridley, A. J.; Schwartz, M. A.; Burridge, K.; Firtel, R. A.; Ginsberg, M. H.; Borisy, G.; Parsons, J. T.; Horwitz, A. R. Cell migration:Integrating signals from front to back. *Science* **2003**, *302* (5651), 1704–1709. DOI: 10.1126/science.1092053.

(108) Manahan, C. L.; Iglesias, P. A.; Long, Y.; Devreotes, P. N. Chemoattractant signaling in dictyostelium discoideum. *Annual review of cell and developmental biology* **2004**, *20*, 223–253. DOI: 10.1146/annurev.cellbio.20.011303.132633.

(109) Li Jeon, N.; Baskaran, H.; Dertinger, S. K. W.; Whitesides, G. M.; van de Water, L.; Toner, M. Neutrophil chemotaxis in linear and complex gradients of interleukin-8 formed in a microfabricated device. *Nature biotechnology* **2002**, *20* (8), 826–830. DOI: 10.1038/nbt712.

(110) Irimia, D.; Liu, S.-Y.; Tharp, W. G.; Samadani, A.; Toner, M.; Poznansky, M. C. Microfluidic system for measuring neutrophil migratory responses to fast switches of chemical gradients. *Lab Chip* **2006**, *6* (2), 191–198. DOI: 10.1039/b511877h.

(111) Song, L.; Nadkarni, S. M.; Bödeker, H. U.; Beta, C.; Bae, A.; Franck, C.; Rappel, W.-J.; Loomis, W. F.; Bodenschatz, E. Dictyostelium discoideum chemotaxis:Threshold for directed motion. *European journal of cell biology* **2006**, *85* (9-10), 981–989. DOI: 10.1016/j.ejcb.2006.01.012.

(112) Meier, B.; Zielinski, A.; Weber, C.; Arcizet, D.; Youssef, S.; Franosch, T.; Rädler, J. O.; Heinrich, D. Chemotactic cell trapping in controlled alternating gradient fields. *Proceedings of the National Academy of Sciences of the United States of America* **2011**, *108* (28), 11417–11422. DOI: 10.1073/pnas.1014853108.

(113) Verkhovsky, A. B.; Svitkina, T. M.; Borisy, G. G. Self-polarization and directional motility of cytoplasm. *Current Biology* **1999**, *9* (1), 11-S1. DOI: 10.1016/S0960-9822(99)80042-6.

(114) Lo, C.-M.; Wang, H.-B.; Dembo, M.; Wang, Y. Cell Movement Is Guided by the Rigidity of the Substrate. *Biophysical journal* **2000**, *79* (1), 144–152. DOI: 10.1016/S0006-3495(00)76279-5.

(115) Saez, A.; Ghibaudo, M.; Buguin, A.; Silberzan, P.; Ladoux, B. Rigidity-driven growth and migration of epithelial cells on microstructured anisotropic substrates.

Proceedings of the National Academy of Sciences of the United States of America **2007**, *104* (20), 8281–8286. DOI: 10.1073/pnas.0702259104.

(116) Kemkemer, R.; Neidlinger-Wilke, C.; Claes, L.; Gruler, H. Cell orientation induced by extracellular signals. *Cell biochemistry and biophysics* **1999**, *30* (2), 167–192. DOI: 10.1007/BF02738066.

(117) Frey, M. T.; Tsai, I. Y.; Russell, T. P.; Hanks, S. K.; Wang, Y. Cellular responses to substrate topography:Role of myosin II and focal adhesion kinase. *Biophysical journal* **2006**, *90* (10), 3774–3782. DOI: 10.1529/biophysj.105.074526.

(118) Tan, J.; Shen, H.; Saltzman, W. M. Micron-Scale Positioning of Features Influences the Rate of Polymorphonuclear Leukocyte Migration. *Biophysical journal* **2001**, *81* (5), 2569–2579. DOI: 10.1016/S0006-3495(01)75901-2.

(119) Tan, J.; Shen, H.; Carter, K. L.; Saltzman, W. M. Controlling human polymorphonuclear leukocytes motility using microfabrication technology. *Journal of biomedical materials research* **2000**, *51* (4), 694–702.

(120) Ladam, G.; Vonna, L.; Sackmann, E. Protrusion force transmission of amoeboid cells crawling on soft biological tissue. *Acta biomaterialia* **2005**, *1* (5), 485–497. DOI: 10.1016/j.actbio.2005.06.002.

(121) Delanoë-Ayari, H.; Rieu, J. P.; Sano, M. 4D traction force microscopy reveals asymmetric cortical forces in migrating Dictyostelium cells. *Physical review letters* **2010**, *105* (24), 248103. DOI: 10.1103/PhysRevLett.105.248103.

(122) Youssef, S.; Gude, S.; Rädler, J. O. Automated tracking in live-cell time-lapse movies. *Integrative biology : quantitative biosciences from nano to macro* **2011**, *3* (11), 1095–1101. DOI: 10.1039/c1ib00035g.

(123) Arcizet, D.; Meier, B.; Sackmann, E.; Rädler, J. O.; Heinrich, D. Temporal analysis of active and passive transport in living cells. *Physical review letters* **2008**, *101* (24), 248103. DOI: 10.1103/PhysRevLett.101.248103.

(124) Le Berre, M.; Liu, Y.-J.; Hu, J.; Maiuri, P.; Bénichou, O.; Voituriez, R.; Chen, Y.; Piel, M. Geometric friction directs cell migration. *Physical review letters* **2013**, *111* (19), 198101. DOI: 10.1103/PhysRevLett.111.198101.

(125) Weijer, C. J. Collective cell migration in development. *Journal of cell science* **2009**, *122* (Pt 18), 3215–3223. DOI: 10.1242/jcs.036517.

(126) Kurosaka, S.; Kashina, A. Cell biology of embryonic migration. *Birth defects research. Part C, Embryo today : reviews* **2008**, *84* (2), 102–122. DOI: 10.1002/bdrc.20125.

(127) Lee, S. J.; Choi, J. S.; Park, K. S.; Khang, G.; Lee, Y. M.; Lee, H. B. Response of MG63 osteoblast-like cells onto polycarbonate membrane surfaces with different micropore sizes. *Biomaterials* **2004**, *25* (19), 4699–4707. DOI: 10.1016/j.biomaterials.2003.11.034.

(128) Friedl, P.; Bröcker, E. B. The biology of cell locomotion within three-dimensional extracellular matrix. *Cellular and molecular life sciences : CMLS* **2000**, *57* (1), 41–64. DOI: 10.1007/s000180050498.

(129) Oakes, P. W.; Patel, D. C.; Morin, N. A.; Zitterbart, D. P.; Fabry, B.; Reichner, J. S.; Tang, J. X. Neutrophil morphology and migration are affected by substrate elasticity. *Blood* **2009**, *114* (7), 1387–1395. DOI: 10.1182/blood-2008-11-191445.

(130) Wolf, K.; Müller, R.; Borgmann, S.; Bröcker, E.-B.; Friedl, P. Amoeboid shape change and contact guidance:T-lymphocyte crawling through fibrillar collagen is independent of matrix remodeling by MMPs and other proteases. *Blood* **2003**, *102* (9), 3262–3269. DOI: 10.1182/blood-2002-12-3791.

(131) Annesley, S. J.; Fisher, P. R. Dictyostelium discoideum--a model for many reasons. *Molecular and cellular biochemistry* **2009**, *329* (1-2), 73–91. DOI: 10.1007/s11010-009-0111-8.

(132) Weiner, O. D. Regulation of cell polarity during eukaryotic chemotaxis:The chemotactic compass. *Current opinion in cell biology* **2002**, *14* (2), 196–202.

(133) Lämmermann, T.; Sixt, M. Mechanical modes of 'amoeboid' cell migration. *Current opinion in cell biology* **2009**, *21* (5), 636–644. DOI: 10.1016/j.ceb.2009.05.003.

(134) Albuschies, J.; Vogel, V. The role of filopodia in the recognition of nanotopographies. *Scientific reports* **2013**, *3*, 1658. DOI: 10.1038/srep01658.

(135) Driscoll, M. K.; Sun, X.; Guven, C.; Fourkas, J. T.; Losert, W. Cellular contact guidance through dynamic sensing of nanotopography. *ACS nano* **2014**, *8* (4), 3546–3555. DOI: 10.1021/nn406637c.

(136) Emmert, M.; Witzel, P.; Heinrich, D. Challenges in tissue engineering - towards cell control inside artificial scaffolds. *Soft matter* **2016**, *12* (19), 4287–4294. DOI: 10.1039/c5sm02844b.

(137) Preedy, E.; Perni, S.; Nipiĉ, D.; Bohinc, K.; Prokopovich, P. Surface roughness mediated adhesion forces between borosilicate glass and gram-positive bacteria. *Langmuir : the ACS journal of surfaces and colloids* **2014**, *30* (31), 9466–9476. DOI: 10.1021/la501711t.

(138) Gorelashvili, M.; Emmert, M.; Hodeck, K. F.; Heinrich, D. Amoeboid migration mode adaption in quasi-3D spatial density gradients of varying lattice geometry. *New J. Phys.* **2014**, *16* (7), 75012. DOI: 10.1088/1367-2630/16/7/075012.

(139) Nandi, A.; Heinrich, D.; Lindner, B. Distributions of diffusion measures from a local mean-square displacement analysis. *Physical review. E, Statistical, nonlinear, and soft matter physics* **2012**, *86* (2 Pt 1), 21926. DOI: 10.1103/PhysRevE.86.021926.

(140) Tan, J.; Saltzman, W. M. Topographical control of human neutrophil motility on micropatterned materials with various surface chemistry. *Biomaterials* **2002**, *23* (15), 3215–3225.

(141) Song, K. H.; Park, S. J.; Kim, D. S.; Doh, J. Sinusoidal wavy surfaces for curvature-guided migration of T lymphocytes. *Biomaterials* **2015**, *51*, 151–160. DOI: 10.1016/j.biomaterials.2015.01.071.

(142) Jay, P. Y.; Pham, P. A.; Wong, S. A.; Elson, E. L. A mechanical function of myosin II in cell motility. *Journal of cell science* **1995**, *108 (Pt 1)*, 387–393.

(143) Fukui, Y.; Lozanne, A. de; Spudich, J. A. Structure and function of the cytoskeleton of a Dictyostelium myosin-defective mutant. *The Journal of cell biology* **1990**, *110* (2), 367–378.

(144) Pasternak, C.; Spudich, J. A.; Elson, E. L. Capping of surface receptors and concomitant cortical tension are generated by conventional myosin. *Nature* **1989**, *341* (6242), 549–551. DOI: 10.1038/341549a0.

(145) Yumura, S. How does myosin II localize within aDictyostelium cell? *J. Plant Res.* **1997**, *110* (4), 501–510. DOI: 10.1007/BF02506812.

(146) Shelden, E.; Knecht, D. A. Dictyostelium cell shape generation requires myosin II. *Cell Motil. Cytoskeleton* **1996**, *35* (1), 59–67. DOI: 10.1002/(SICI)1097-0169(1996)35:1<59:AID-CM5>3.0.CO;2-D.

(147) Grabham, P. W.; Reznik, B.; Goldberg, D. J. Microtubule and Rac 1-dependent F-actin in growth cones. *Journal of cell science* **2003**, *116* (Pt 18), 3739–3748. DOI: 10.1242/jcs.00686.

(148) Zins, S. R.; Amare, M. F.; Anam, K.; Elster, E. A.; Davis, T. A. Wound trauma mediated inflammatory signaling attenuates a tissue regenerative response in MRL/MpJ mice. *Journal of inflammation (London, England)* **2010**, *7*, 25. DOI: 10.1186/1476-9255-7-25.

(149) Hulsman, M.; Hulshof, F.; Unadkat, H.; Papenburg, B. J.; Stamatialis, D. F.; Truckenmüller, R.; van Blitterswijk, C.; Boer, J. de; Reinders, M. J. T. Analysis of high-throughput screening reveals the effect of surface topographies on cellular morphology. *Acta biomaterialia* **2015**, *15*, 29–38. DOI: 10.1016/j.actbio.2014.12.019.

(150) Edmondson, R.; Broglie, J. J.; Adcock, A. F.; Yang, L. Three-Dimensional Cell Culture Systems and Their Applications in Drug Discovery and Cell-Based Biosensors. *Assay and Drug Development Technologies* **2014**, *12* (4), 207–218. DOI: 10.1089/adt.2014.573.

(151) Mirbagheri, M.; Adibnia, V.; Hughes, B. R.; Waldman, S. D.; Banquy, X.; Hwang, D. K. Advanced cell culture platforms: a growing quest for emulating natural tissues. *Mater. Horiz.* **2019**, *6* (1), 45–71. DOI: 10.1039/C8MH00803E.

(152) Ermis, M.; Antmen, E.; Hasirci, V. Micro and Nanofabrication methods to control cell-substrate interactions and cell behavior: A review from the tissue engineering perspective. *Bioactive materials* **2018**, *3* (3), 355–369. DOI: 10.1016/j.bioactmat.2018.05.005.

(153) Porter, J. R.; Ruckh, T. T.; Popat, K. C. Bone tissue engineering:A review in bone biomimetics and drug delivery strategies. *Biotechnology progress* **2009**, *25* (6), 1539–1560. DOI: 10.1002/btpr.246.

(154) Marwick, C. Implant Recommendations. *JAMA* **2000**, *283* (7), 869. DOI: 10.1001/jama.283.7.869-JMN0216-2-1.

(155) Biggs, M. J. P.; Richards, R. G.; Dalby, M. J. Nanotopographical modification:A regulator of cellular function through focal adhesions. *Nanomedicine : nanotechnology, biology, and medicine* **2010**, *6* (5), 619–633. DOI: 10.1016/j.nano.2010.01.009.

(156) Hoess, A.; Thormann, A.; Friedmann, A.; Heilmann, A. Self-supporting nanoporous alumina membranes as substrates for hepatic cell cultures. *Journal of biomedical materials research. Part A* **2012**, *100* (9), 2230–2238. DOI: 10.1002/jbm.a.34158.

(157) Hench, L. L.; Day, D. E.; Höland, W.; Rheinberger, V. M. Glass and Medicine. *International Journal of Applied Glass Science* **2010**, *1* (1), 104–117. DOI: 10.1111/j.2041-1294.2010.00001.x.

(158) Peelen, J. G. J.; Metselaar, R. Light scattering by pores in polycrystalline materials:Transmission properties of alumina. *Journal of Applied Physics* **1974**, *45* (1), 216–220. DOI: 10.1063/1.1662961.

(159) Chen, W. W.; Dunn, B. Characterization of Pore Size Distribution by Infrared Scattering in Highly Dense ZnS. *J American Ceramic Society* **1993**, *76* (8), 2086–2092. DOI: 10.1111/j.1151-2916.1993.tb08337.x.

(160) Ramsey, W. S.; Hertl, W.; Nowlan, E. D.; Binkowski, N. J. Surface treatments and cell attachment. *In Vitro* **1984**, *20* (10), 802–808. DOI: 10.1007/BF02618296.

(161) Cooke, M. J.; Phillips, S. R.; Shah, D. S. H.; Athey, D.; Lakey, J. H.; Przyborski, S. A. Enhanced cell attachment using a novel cell culture surface presenting functional domains from extracellular matrix proteins. *Cytotechnology* **2008**, *56* (2), 71–79. DOI: 10.1007/s10616-007-9119-7.

(162) Scherzer, M. T.; Waigel, S.; Donninger, H.; Arumugam, V.; Zacharias, W.; Clark, G.; Siskind, L. J.; Soucy, P.; Beverly, L. Fibroblast-Derived Extracellular Matrices:An Alternative Cell Culture System That Increases Metastatic Cellular Properties. *PloS one* **2015**, *10* (9), e0138065. DOI: 10.1371/journal.pone.0138065.

(163) Liliensiek, S. J.; Campbell, S.; Nealey, P. F.; Murphy, C. J. The scale of substratum topographic features modulates proliferation of corneal epithelial cells and corneal fibroblasts. *Journal of biomedical materials research. Part A* **2006**, *79* (1), 185–192. DOI: 10.1002/jbm.a.30744.

(164) Flemming, R. G.; Murphy, C. J.; Abrams, G. A.; Goodman, S. L.; Nealey, P. F. Effects of synthetic micro- and nano-structured surfaces on cell behavior. *Biomaterials* **1999**, *20* (6), 573–588. DOI: 10.1016/S0142-9612(98)00209-9.

(165) Bettinger, C. J.; Langer, R.; Borenstein, J. T. Engineering substrate topography at the micro- and nanoscale to control cell function. *Angewandte Chemie (International ed. in English)* **2009**, *48* (30), 5406–5415. DOI: 10.1002/anie.200805179.

(166) Kim, D.-H.; Provenzano, P. P.; Smith, C. L.; Levchenko, A. Matrix nanotopography as a regulator of cell function. *The Journal of cell biology* **2012**, *197* (3), 351–360. DOI: 10.1083/jcb.201108062.

(167) Bettinger, C. J.; Zhang, Z.; Gerecht, S.; Borenstein, J. T.; Langer, R. Enhancement of In Vitro Capillary Tube Formation by Substrate Nanotopography. *Advanced materials (Deerfield Beach, Fla.)* **2008**, *20* (1), 99–103. DOI: 10.1002/adma.200702487.

(168) Dulgar-Tulloch, A. J.; Bizios, R.; Siegel, R. W. Human mesenchymal stem cell adhesion and proliferation in response to ceramic chemistry and nanoscale topography. *Journal of biomedical materials research. Part A* **2009**, *90* (2), 586–594. DOI: 10.1002/jbm.a.32116.

(169) Washburn, N. R.; Yamada, K. M.; Simon, C. G.; Kennedy, S. B.; Amis, E. J. High-throughput investigation of osteoblast response to polymer crystallinity: influence of nanometer-scale roughness on proliferation. *Biomaterials* **2004**, *25* (7-8), 1215–1224. DOI: 10.1016/j.biomaterials.2003.08.043.

(170) Brunetti, V.; Maiorano, G.; Rizzello, L.; Sorce, B.; Sabella, S.; Cingolani, R.; Pompa, P. P. Neurons sense nanoscale roughness with nanometer sensitivity. *Proceedings of the National Academy of Sciences of the United States of America* **2010**, *107* (14), 6264–6269. DOI: 10.1073/pnas.0914456107.

(171) Milner, K. R.; Siedlecki, C. A. Fibroblast response is enhanced by poly(L-lactic acid) nanotopography edge density and proximity. *International Journal of Nanomedicine* **20**, *2* (2), 201–211.

(172) Friedmann, A.; Hoess, A.; Cismak, A.; Heilmann, A. Investigation of cell-substrate interactions by focused ion beam preparation and scanning electron microscopy. *Acta Biomater* **2011**, *7* (6), 2499–2507. DOI: 10.1016/j.actbio.2011.02.024.

(173) Cavalcanti-Adam, E. A.; Micoulet, A.; Blümmel, J.; Auernheimer, J.; Kessler, H.; Spatz, J. P. Lateral spacing of integrin ligands influences cell spreading and focal adhesion assembly. *European journal of cell biology* **2006**, *85* (3-4), 219–224. DOI: 10.1016/j.ejcb.2005.09.011.

(174) Selhuber-Unkel, C.; López-García, M.; Kessler, H.; Spatz, J. P. Cooperativity in adhesion cluster formation during initial cell adhesion. *Biophysical journal* **2008**, *95* (11), 5424–5431. DOI: 10.1529/biophysj.108.139584.

(175) Gurski, L. A.; Petrelli, N. J.; Jia, X.; Farach-Carson, M. C. 3D Matrices for Anti-Cancer Drug Testing and Development. *Oncology Issues* **2010**, *25* (1), 20–25. DOI: 10.1080/10463356.2010.11883480.

(176) Tateishi, T.; Chen, G.; Ushida, T. Biodegradable porous scaffolds for tissue engineering. *J Artif Organs* **2002**, *5* (2), 77–83. DOI: 10.1007/s100470200014.

(177) Frisch, S. M.; Vuori, K.; Ruoslahti, E.; Chan-Hui*, P.-Y. Control of adhesion-dependent cell survival by focal adhesion kinase. *J Cell Biol* **1996**, *134* (3), 793–799. DOI: 10.1083/jcb.134.3.793.

(178) Paoli, P.; Giannoni, E.; Chiarugi, P. Anoikis molecular pathways and its role in cancer progression. *Biochimica et biophysica acta* **2013**, *1833* (12), 3481–3498. DOI: 10.1016/j.bbamcr.2013.06.026.

(179) Guadarrama Bello, D.; Fouillen, A.; Badia, A.; Nanci, A. A nanoporous titanium surface promotes the maturation of focal adhesions and formation of filopodia with distinctive nanoscale protrusions by osteogenic cells. *Acta biomaterialia* **2017**, *60*, 339–349. DOI: 10.1016/j.actbio.2017.07.022.

(180) Mackie, E. J.; Ahmed, Y. A.; Tatarczuch, L.; Chen, K.-S.; Mirams, M. Endochondral ossification: how cartilage is converted into bone in the developing skeleton. *The International Journal of Biochemistry & Cell Biology* **2008**, *40* (1), 46–62. DOI: 10.1016/j.biocel.2007.06.009.

(181) Aghajanian, P.; Mohan, S. The art of building bone: emerging role of chondrocyte-to-osteoblast transdifferentiation in endochondral ossification. *Bone research* **2018**, *6*, 19. DOI: 10.1038/s41413-018-0021-z.

(182) Li, Y. Y.; Choy, T. H.; Ho, F. C.; Chan, P. B. Scaffold composition affects cytoskeleton organization, cell-matrix interaction and the cellular fate of human mesenchymal stem cells upon chondrogenic differentiation. *Biomaterials* **2015**, *52*, 208–220. DOI: 10.1016/j.biomaterials.2015.02.037.

(183) Lydon, H.; Getgood, A.; Henson, F. M. D. Healing of Osteochondral Defects via Endochondral Ossification in an Ovine Model. *Cartilage* **2019**, *10* (1), 94–101. DOI: 10.1177/1947603517713818.

(184) Nooeaid, P.; Salih, V.; Beier, J. P.; Boccaccini, A. R. Osteochondral tissue engineering: scaffolds, stem cells and applications. *Journal of cellular and molecular medicine* **2012**, *16* (10), 2247–2270. DOI: 10.1111/j.1582-4934.2012.01571.x.

(185) Zhu, X.; Chen, J.; Scheideler, L.; Altebaeumer, T.; Geis-Gerstorfer, J.; Kern, D. Cellular reactions of osteoblasts to micron- and submicron-scale porous structures of titanium surfaces. *Cells Tissues Organs (Print)* **2004**, *178* (1), 13–22. DOI: 10.1159/000081089.

(186) Poinern, G. E. J.; Le, X. T.; O'Dea, M.; Becker, T.; Fawcett, D. Chemical synthesis, characterisation, and biocompatibility of nanometre scale porous anodic aluminium oxide membranes for use as a cell culture substrate for the vero cell line:A preliminary study. *BioMed research international* **2014**, *2014*, 238762. DOI: 10.1155/2014/238762.

(187) Kaverina, I.; Straube, A. Regulation of cell migration by dynamic microtubules. *Seminars in cell & developmental biology* **2011**, *22* (9), 968–974. DOI: 10.1016/j.semcdb.2011.09.017.

(188) Emmert, M.; Witzel, P.; Rothenburger-Glaubitt, M.; Heinrich, D. Nanostructured surfaces of biodegradable silica fibers enhance directed amoeboid cell migration in a microtubule-dependent process. *RSC Adv.* **2017**, *7* (10), 5708–5714. DOI: 10.1039/C6RA25739A.

(189) Sun, X.; Driscoll, M. K.; Guven, C.; Das, S.; Parent, C. A.; Fourkas, J. T.; Losert, W. Asymmetric nanotopography biases cytoskeletal dynamics and promotes unidirectional cell guidance. *Proceedings of the National Academy of Sciences of the United States of America* **2015**, *112* (41), 12557–12562. DOI: 10.1073/pnas.1502970112.

(190) Bretschneider, T.; Anderson, K.; Ecke, M.; Müller-Taubenberger, A.; Schroth-Diez, B.; Ishikawa-Ankerhold, H. C.; Gerisch, G. The three-dimensional dynamics of actin waves, a model of cytoskeletal self-organization. *Biophysical journal* **2009**, *96* (7), 2888–2900. DOI: 10.1016/j.bpj.2008.12.3942.

(191) Bretschneider, T.; Jonkman, J.; Köhler, J.; Medalia, O.; Barisic, K.; Weber, I.; Stelzer, E. H. K.; Baumeister, W.; Gerisch, G. Dynamic organization of the actin system in the motile cells of Dictyostelium. *Journal of muscle research and cell motility* **2002**, *23* (7-8), 639–649.

(192) Vicker, M. G. Reaction-diffusion waves of actin filament polymerization/depolymerization in Dictyostelium pseudopodium extension and cell locomotion. *Biophysical chemistry* **2000**, *84* (2), 87–98.

(193) Inagaki, N.; Katsuno, H. Actin Waves:Origin of Cell Polarization and Migration? *Trends in cell biology* **2017**, *27* (7), 515–526. DOI: 10.1016/j.tcb.2017.02.003.

(194) Li, S.; Kuddannaya, S.; Chuah, Y. J.; Bao, J.; Zhang, Y.; Wang, D. Combined effects of multi-scale topographical cues on stable cell sheet formation and differentiation of mesenchymal stem cells. *Biomaterials science* **2017**, *5* (10), 2056–2067. DOI: 10.1039/c7bm00134g.

(195) Usui, M. L.; Mansbridge, J. N.; Carter, W. G.; Fujita, M.; Olerud, J. E. Keratinocyte migration, proliferation, and differentiation in chronic ulcers from patients with diabetes and normal wounds. *The journal of histochemistry and cytochemistry : official journal of the Histochemistry Society* **2008**, *56* (7), 687–696. DOI: 10.1369/jhc.2008.951194.

(196) Brown, A.; Augustin, M.; Jünger, M.; Zutt, M.; Dissemond, J.; Rabe, E.; Kaufmann, R.; Simon, M.; Stücker, M.; Karrer, S.; Koenen, W.; Vanscheidt, W.; Scharfetter-Kochanek, K.; Wollina, U.; Krieg, T.; Eming, S. A. Randomized standard-of-care-controlled trial of a silica gel fibre matrix in the treatment of chronic venous leg ulcers. *European journal of dermatology : EJD* **2014**, *24* (2), 210–216. DOI: 10.1684/ejd.2014.2344.

(197) Czuryszkiewicz, T.; Ahvenlammi, J.; Kortesuo, P.; Ahola, M.; Kleitz, F.; Jokinen, M.; Lindén, M.; Rosenholm, J. B. Drug release from biodegradable silica fibers. *Journal of Non-Crystalline Solids* **2002**, *306* (1), 1–10. DOI: 10.1016/S0022-3093(02)01060-8.

(198) Grotheer, V.; Goergens, M.; Fuchs, P. C.; Dunda, S.; Pallua, N.; Windolf, J.; Suschek, C. V. The performance of an orthosilicic acid-releasing silica gel fiber fleece in wound healing. *Biomaterials* **2013**, *34* (30), 7314–7327. DOI: 10.1016/j.biomaterials.2013.06.012.

(199) Sun, T.; Norton, D.; Ryan, A. J.; MacNeil, S.; Haycock, J. W. Investigation of fibroblast and keratinocyte cell-scaffold interactions using a novel 3D cell culture system. *Journal of materials science. Materials in medicine* **2007**, *18* (2), 321–328. DOI: 10.1007/s10856-006-0696-3.

(200) Jones, J. R.; Lin, S.; Yue, S.; Lee, P. D.; Hanna, J. V.; Smith, M. E.; Newport, R. J. Bioactive glass scaffolds for bone regeneration and their hierarchical characterisation. *Proceedings of the Institution of Mechanical Engineers. Part H, Journal of engineering in medicine* **2010**, *224* (12), 1373–1387. DOI: 10.1243/09544119JEIM836.

(201) Patla, I.; Volberg, T.; Elad, N.; Hirschfeld-Warneken, V.; Grashoff, C.; Fässler, R.; Spatz, J. P.; Geiger, B.; Medalia, O. Dissecting the molecular architecture of integrin

adhesion sites by cryo-electron tomography. *Nature cell biology* **2010**, *12* (9), 909–915. DOI: 10.1038/ncb2095.

(202) Poole, K.; Khairy, K.; Friedrichs, J.; Franz, C.; Cisneros, D. A.; Howard, J.; Mueller, D. Molecular-scale topographic cues induce the orientation and directional movement of fibroblasts on two-dimensional collagen surfaces. *Journal of molecular biology* **2005**, *349* (2), 380–386. DOI: 10.1016/j.jmb.2005.03.064.

(203) Gasiorowski, J. Z.; Liliensiek, S. J.; Russell, P.; Stephan, D. A.; Nealey, P. F.; Murphy, C. J. Alterations in gene expression of human vascular endothelial cells associated with nanotopographic cues. *Biomaterials* **2010**, *31* (34), 8882–8888. DOI: 10.1016/j.biomaterials.2010.08.026.

(204) Muhammad, R.; Lim, S. H.; Goh, S. H.; Law, J. B. K.; Saifullah, M. S. M.; Ho, G. W.; Yim, E. K. F. Sub-100 nm patterning of TiO 2 film for the regulation of endothelial and smooth muscle cell functions. *Biomater. Sci.* **2014**, *2* (12), 1740–1749. DOI: 10.1039/C4BM00212A.

(205) McNamara, L. E.; McMurray, R. J.; Biggs, M. J. P.; Kantawong, F.; Oreffo, R. O. C.; Dalby, M. J. Nanotopographical control of stem cell differentiation. *Journal of tissue engineering* **2010**, *2010*, 120623. DOI: 10.4061/2010/120623.

(206) Sun, Y.; Chen, C. S.; Fu, J. Forcing stem cells to behave:A biophysical perspective of the cellular microenvironment. *Annual review of biophysics* **2012**, *41*, 519–542. DOI: 10.1146/annurev-biophys-042910-155306.

(207) Song, W.; Lu, H.; Kawazoe, N.; Chen, G. Adipogenic differentiation of individual mesenchymal stem cell on different geometric micropatterns. *Langmuir : the ACS journal of surfaces and colloids* **2011**, *27* (10), 6155–6162. DOI: 10.1021/la200487w.

(208) González-Cruz, R. D.; Fonseca, V. C.; Darling, E. M. Cellular mechanical properties reflect the differentiation potential of adipose-derived mesenchymal stem cells. *Proceedings of the National Academy of Sciences of the United States of America* **2012**, *109* (24), E1523-9. DOI: 10.1073/pnas.1120349109.

(209) Higuera, G. A.; van Boxtel, A.; van Blitterswijk, C. A.; Moroni, L. The physics of tissue formation with mesenchymal stem cells. *Trends in biotechnology* **2012**, *30* (11), 583–590. DOI: 10.1016/j.tibtech.2012.07.007.

(210) Dalby, M. J.; Gadegaard, N.; Tare, R.; Andar, A.; Riehle, M. O.; Herzyk, P.; Wilkinson, C. D. W.; Oreffo, R. O. C. The control of human mesenchymal cell differentiation using nanoscale symmetry and disorder. *Nature materials* **2007**, *6* (12), 997–1003. DOI: 10.1038/nmat2013.

(211) Brammer, K. S.; Choi, C.; Frandsen, C. J.; Oh, S.; Jin, S. Hydrophobic nanopillars initiate mesenchymal stem cell aggregation and osteo-differentiation. *Acta biomaterialia* **2011**, *7* (2), 683–690. DOI: 10.1016/j.actbio.2010.09.022.

(212) Lavenus, S.; Berreur, M.; Trichet, V.; Pilet, P.; Louarn, G.; Layrolle, P. Adhesion and osteogenic differentiation of human mesenchymal stem cells on titanium nanopores. *eCM* **2011**, *22*, 84–96. DOI: 10.22203/eCM.v022a07.

(213) Oh, S.; Brammer, K. S.; Li, Y. S. J.; Teng, D.; Engler, A. J.; Chien, S.; Jin, S. Stem cell fate dictated solely by altered nanotube dimension. *Proceedings of the National Academy of Sciences of the United States of America* **2009**, *106* (7), 2130–2135. DOI: 10.1073/pnas.0813200106.

(214) Zhao, L.; Mei, S.; Wang, W.; Chu, P. K.; Zhang, Y.; Wu, Z. Suppressed primary osteoblast functions on nanoporous titania surface. *Journal of biomedical materials research. Part A* **2011**, *96* (1), 100–107. DOI: 10.1002/jbm.a.32918.

(215) Zhao, L.; Liu, L.; Wu, Z.; Zhang, Y.; Chu, P. K. Effects of micropitted/nanotubular titania topographies on bone mesenchymal stem cell osteogenic differentiation. *Biomaterials* **2012**, *33* (9), 2629–2641. DOI: 10.1016/j.biomaterials.2011.12.024.

(216) Collart-Dutilleul, P.-Y.; Panayotov, I.; Secret, E.; Cunin, F.; Gergely, C.; Cuisinier, F.; Martin, M. Initial stem cell adhesion on porous silicon surface: molecular architecture of actin cytoskeleton and filopodial growth. *Nanoscale research letters* **2014**, *9* (1), 564. DOI: 10.1186/1556-276X-9-564.

(217) Dalby, M. J.; Giannaras, D.; Riehle, M. O.; Gadegaard, N.; Affrossman, S.; Curtis, A. Rapid fibroblast adhesion to 27nm high polymer demixed nano-topography. *Biomaterials* **2004**, *25* (1), 77–83. DOI: 10.1016/S0142-9612(03)00475-7.

(218) Cai, K.; Bossert, J.; Jandt, K. D. Does the nanometre scale topography of titanium influence protein adsorption and cell proliferation? *Colloids and surfaces. B, Biointerfaces* **2006**, *49* (2), 136–144. DOI: 10.1016/j.colsurfb.2006.02.016.

(219) Li, N.; Zhang, J.; Xing, W.; Di Ouyang; Liu, L. 3D printing of Fe-based bulk metallic glass composites with combined high strength and fracture toughness. *Materials & Design* **2018**, *143*, 285–296. DOI: 10.1016/j.matdes.2018.01.061.

(220) Arnold, M.; Schwieder, M.; Blümmel, J.; Cavalcanti-Adam, E. A.; López-Garcia, M.; Kessler, H.; Geiger, B.; Spatz, J. P. Cell interactions with hierarchically structured nano-patterned adhesive surfaces. *Soft matter* **2009**, *5* (1), 72–77. DOI: 10.1039/B815634D.

(221) Gilchrist, C. L.; Ruch, D. S.; Little, D.; Guilak, F. Micro-scale and meso-scale architectural cues cooperate and compete to direct aligned tissue formation. *Biomaterials* **2014**, *35* (38), 10015–10024. DOI: 10.1016/j.biomaterials.2014.08.047.

(222) Arima, Y.; Iwata, H. Effect of wettability and surface functional groups on protein adsorption and cell adhesion using well-defined mixed self-assembled monolayers. *Biomaterials* **2007**, *28* (20), 3074–3082. DOI: 10.1016/j.biomaterials.2007.03.013.

(223) Curran, J. M.; Chen, R.; Hunt, J. A. Controlling the phenotype and function of mesenchymal stem cells in vitro by adhesion to silane-modified clean glass surfaces. *Biomaterials* **2005**, *26* (34), 7057–7067. DOI: 10.1016/j.biomaterials.2005.05.008.

(224) Abdul Kafi, M.; El-Said, W. A.; Kim, T.-H.; Choi, J.-W. Cell adhesion, spreading, and proliferation on surface functionalized with RGD nanopillar arrays. *Biomaterials* **2012**, *33* (3), 731–739. DOI: 10.1016/j.biomaterials.2011.10.003.

(225) Chen, Z.; Ni, S.; Han, S.; Crawford, R.; Lu, S.; Wei, F.; Chang, J.; Wu, C.; Xiao, Y. Nanoporous microstructures mediate osteogenesis by modulating the osteo-immune response of macrophages. *Nanoscale* **2017**, *9* (2), 706–718. DOI: 10.1039/c6nr06421c.

(226) Ghrebi, S.; Hamilton, D. W.; Douglas Waterfield, J.; Brunette, D. M. The effect of surface topography on cell shape and early ERK1/2 signaling in macrophages; linkage with FAK and Src. *Journal of biomedical materials research. Part A* **2013**, *101* (7), 2118–2128. DOI: 10.1002/jbm.a.34509.

(227) Bota, P. C. S.; Collie, A. M. B.; Puolakkainen, P.; Vernon, R. B.; Sage, E. H.; Ratner, B. D.; Stayton, P. S. Biomaterial topography alters healing in vivo and monocyte/macrophage activation in vitro. *Journal of biomedical materials research. Part A* **2010**, *95* (2), 649–657. DOI: 10.1002/jbm.a.32893.

(228) Linde, N.; Gutschalk, C. M.; Hoffmann, C.; Yilmaz, D.; Mueller, M. M. Integrating macrophages into organotypic co-cultures:A 3D in vitro model to study tumor-associated macrophages. *PloS one* **2012**, *7* (7), e40058. DOI: 10.1371/journal.pone.0040058.

(229) Hoppe, A.; Güldal, N. S.; Boccaccini, A. R. A review of the biological response to ionic dissolution products from bioactive glasses and glass-ceramics. *Biomaterials* **2011**, *32* (11), 2757–2774. DOI: 10.1016/j.biomaterials.2011.01.004.

(230) Brangwynne, C. P.; Koenderink, G. H.; MacKintosh, F. C.; Weitz, D. A. Intracellular transport by active diffusion. *Trends in cell biology* **2009**, *19* (9), 423–427. DOI: 10.1016/j.tcb.2009.04.004.

(231) Caspi, A.; Granek, R.; Elbaum, M. Diffusion and directed motion in cellular transport. *Physical review. E, Statistical, nonlinear, and soft matter physics* **2002**, *66* (1 Pt 1), 11916. DOI: 10.1103/PhysRevE.66.011916.

(232) Levi, V.; Gratton, E. Exploring dynamics in living cells by tracking single particles. *CBB* **2007**, *48* (1), 1–15. DOI: 10.1007/s12013-007-0010-0.

(233) Welte, M. A. Bidirectional transport along microtubules. *Current biology : CB* **2004**, *14* (13), R525-37. DOI: 10.1016/j.cub.2004.06.045.

(234) Salman, H.; Gil, Y.; Granek, R.; Elbaum, M. Microtubules, motor proteins, and anomalous mean squared displacements. *Chemical Physics* **2002**, *284* (1-2), 389–397. DOI: 10.1016/S0301-0104(02)00669-9.

(235) Otten, M.; Nandi, A.; Arcizet, D.; Gorelashvili, M.; Lindner, B.; Heinrich, D. Local motion analysis reveals impact of the dynamic cytoskeleton on intracellular subdiffusion. *Biophysical journal* **2012**, *102* (4), 758–767. DOI: 10.1016/j.bpj.2011.12.057.

(236) Pelzl, C.; Arcizet, D.; Piontek, G.; Schlegel, J.; Heinrich, D. Axonal guidance by surface microstructuring for intracellular transport investigations. *Chemphyschem : a European journal of chemical physics and physical chemistry* **2009**, *10* (16), 2884–2890. DOI: 10.1002/cphc.200900555.

(237) Mahowald, J.; Arcizet, D.; Heinrich, D. Impact of external stimuli and cell micro-architecture on intracellular transport states. *Chemphyschem : a European journal of chemical physics and physical chemistry* **2009**, *10* (9-10), 1559–1566. DOI: 10.1002/cphc.200900226.

(238) Götz, M.; Hodeck, K. F.; Witzel, P.; Nandi, A.; Lindner, B.; Heinrich, D. Probing cytoskeleton dynamics by intracellular particle transport analysis. *Eur. Phys. J. Spec. Top.* **2015**, *224* (7), 1169–1183. DOI: 10.1140/epjst/e2015-02453-4.

(239) Dupont, A.; Gorelashvili, M.; Schüller, V.; Wehnekamp, F.; Arcizet, D.; Katayama, Y.; Lamb, D. C.; Heinrich, D. Three-dimensional single-particle tracking in live cells: news from the third dimension. *New J. Phys.* **2013**, *15* (7), 75008. DOI: 10.1088/1367-2630/15/7/075008.

(240) Klumpp, S.; Lipowsky, R. Active diffusion of motor particles. *Physical review letters* **2005**, *95* (26), 268102. DOI: 10.1103/PhysRevLett.95.268102.

(241) Heinrich, D.; Sackmann, E. Active mechanical stabilization of the viscoplastic intracellular space of Dictyostelia cells by microtubule-actin crosstalk. *Acta biomaterialia* **2006**, *2* (6), 619–631. DOI: 10.1016/j.actbio.2006.05.014.

(242) Gunawardena, S.; Her, L.-S.; Brusch, R. G.; Laymon, R. A.; Niesman, I. R.; Gordesky-Gold, B.; Sintasath, L.; Bonini, N. M.; Goldstein, L. S. Disruption of Axonal Transport by Loss of Huntingtin or Expression of Pathogenic PolyQ Proteins in Drosophila. *Neuron* **2003**, *40* (1), 25–40. DOI: 10.1016/S0896-6273(03)00594-4.

(243) Sackmann, E.; Reuther, A.; Heinrich, D. Micromechanics of Cells. In *Mechanics of the 21st Century*:*Proceedings of the 21st International Congress of Theoretical*

and Applied Mechanics, Warsaw, Poland, 15-21 August 2004; Gutkowski, W., Kowalewski, T. A., Eds.; Springer, 2005; pp 313–328. DOI: 10.1007/1-4020-3559-4_21.

(244) Guilluy, C.; Osborne, L. D.; van Landeghem, L.; Sharek, L.; Superfine, R.; Garcia-Mata, R.; Burridge, K. Isolated nuclei adapt to force and reveal a mechanotransduction pathway in the nucleus. *Nature cell biology* **2014**, *16* (4), 376–381. DOI: 10.1038/ncb2927.

(245) Janetopoulos, C.; Firtel, R. A. Directional sensing during chemotaxis. *FEBS letters* **2008**, *582* (14), 2075–2085. DOI: 10.1016/j.febslet.2008.04.035.

(246) Bosgraaf, L.; van Haastert, P. J. M. Navigation of chemotactic cells by parallel signaling to pseudopod persistence and orientation. *PloS one* **2009**, *4* (8), e6842. DOI: 10.1371/journal.pone.0006842.

(247) Soll, D. R.; Wessels, D.; Heid, P. J.; Zhang, H. A contextual framework for characterizing motility and chemotaxis mutants in Dictyostelium discoideum. *Journal of muscle research and cell motility* **2002**, *23* (7-8), 659–672. DOI: 10.1023/a:1024459124427.

(248) Reig, G.; Pulgar, E.; Concha, M. L. Cell migration: from tissue culture to embryos. *Development (Cambridge, England)* **2014**, *141* (10), 1999–2013. DOI: 10.1242/dev.101451.

(249) Song, H.; Poo, M. The cell biology of neuronal navigation. *Nature cell biology* **2001**, *3* (3), E81-8. DOI: 10.1038/35060164.

(250) Müller, A.; Homey, B.; Soto, H.; Ge, N.; Catron, D.; Buchanan, M. E.; McClanahan, T.; Murphy, E.; Yuan, W.; Wagner, S. N.; Barrera, J. L.; Mohar, A.; Verástegui, E.; Zlotnik, A. Involvement of chemokine receptors in breast cancer metastasis. *Nature* **2001**, *410* (6824), 50–56. DOI: 10.1038/35065016.

(251) Futrelle, R. P. Dictyostelium chemotactic response to spatial and temporal gradients. Theories of the limits of chemotactic sensitivity and of pseudochemotaxis. *Journal of cellular biochemistry* **1982**, *18* (2), 197–212. DOI: 10.1002/jcb.1982.240180207.

(252) Zatulovskiy, E.; Tyson, R.; Bretschneider, T.; Kay, R. R. Bleb-driven chemotaxis of Dictyostelium cells. *The Journal of cell biology* **2014**, *204* (6), 1027–1044. DOI: 10.1083/jcb.201306147.

(253) Zicha, D.; Dunn, G. A.; Brown, A. F. A new direct-viewing chemotaxis chamber. *Journal of cell science* **1991**, *99 (Pt 4)*, 769–775.

(254) BOYDEN, S. The chemotactic effect of mixtures of antibody and antigen on polymorphonuclear leucocytes. *The Journal of experimental medicine* **1962**, *115*, 453–466. DOI: 10.1084/jem.115.3.453.

(255) García, S.; Sunyer, R.; Olivares, A.; Noailly, J.; Atencia, J.; Trepat, X. Generation of stable orthogonal gradients of chemical concentration and substrate stiffness in a microfluidic device. *Lab on a chip* **2015**, *15* (12), 2606–2614. DOI: 10.1039/c5lc00140d.

(256) Dertinger, S. K. W.; Chiu, D. T.; Jeon, N. L.; Whitesides, G. M. Generation of Gradients Having Complex Shapes Using Microfluidic Networks. *Anal. Chem.* **2001**, *73* (6), 1240–1246. DOI: 10.1021/ac001132d.

(257) Lin, F.; Nguyen, C. M.-C.; Wang, S.-J.; Saadi, W.; Gross, S. P.; Jeon, N. L. Neutrophil migration in opposing chemoattractant gradients using microfluidic chemotaxis devices. *Annals of biomedical engineering* **2005**, *33* (4), 475–482. DOI: 10.1007/s10439-005-2503-6.

(258) Lin, F.; Butcher, E. C. T cell chemotaxis in a simple microfluidic device. *Lab on a chip* **2006**, *6* (11), 1462–1469. DOI: 10.1039/b607071j.

(259) Beta, C.; Wyatt, D.; Rappel, W.-J.; Bodenschatz, E. Flow photolysis for spatiotemporal stimulation of single cells. *Anal. Chem.* **2007**, *79* (10), 3940–3944. DOI: 10.1021/ac070033y.

(260) Kuczenski, B.; Ruder, W. C.; Messner, W. C.; Leduc, P. R. Probing cellular dynamics with a chemical signal generator. *PloS one* **2009**, *4* (3), e4847. DOI: 10.1371/journal.pone.0004847.

(261) Kress, H.; Park, J.-G.; Mejean, C. O.; Forster, J. D.; Park, J.; Walse, S. S.; Zhang, Y.; Wu, D.; Weiner, O. D.; Fahmy, T. M.; Dufresne, E. R. Cell stimulation with optically

manipulated microsources. *Nature methods* **2009**, *6* (12), 905–909. DOI: 10.1038/nmeth.1400.

(262) Tweedy, L.; Meier, B.; Stephan, J.; Heinrich, D.; Endres, R. G. Distinct cell shapes determine accurate chemotaxis. *Scientific reports* **2013**, *3*, 2606. DOI: 10.1038/srep02606.

(263) van Haastert, P. J. M.; Postma, M. Biased random walk by stochastic fluctuations of chemoattractant-receptor interactions at the lower limit of detection. *Biophysical journal* **2007**, *93* (5), 1787–1796. DOI: 10.1529/biophysj.107.104356.

(264) Endres, R. G.; Wingreen, N. S. Accuracy of direct gradient sensing by single cells. *Proceedings of the National Academy of Sciences of the United States of America* **2008**, *105* (41), 15749–15754. DOI: 10.1073/pnas.0804688105.

(265) Cukierman, E.; Pankov, R.; Stevens, D. R.; Yamada, K. M. Taking cell-matrix adhesions to the third dimension. *Science (New York, N.Y.)* **2001**, *294* (5547), 1708–1712. DOI: 10.1126/science.1064829.

(266) Ezratty, E. J.; Partridge, M. A.; Gundersen, G. G. Microtubule-induced focal adhesion disassembly is mediated by dynamin and focal adhesion kinase. *Nature cell biology* **2005**, *7* (6), 581–590. DOI: 10.1038/ncb1262.

(267) Krylyshkina, O.; Anderson, K. I.; Kaverina, I.; Upmann, I.; Manstein, D. J.; Small, J. V.; Toomre, D. K. Nanometer targeting of microtubules to focal adhesions. *The Journal of cell biology* **2003**, *161* (5), 853–859. DOI: 10.1083/jcb.200301102.

(268) Hecht, I.; Levine, H.; Rappel, W.-J.; Ben-Jacob, E. "Self-assisted" amoeboid navigation in complex environments. *PloS one* **2011**, *6* (8), e21955. DOI: 10.1371/journal.pone.0021955.

(269) Niculescu, I.; Textor, J.; Boer, R. J. de. Crawling and Gliding: A Computational Model for Shape-Driven Cell Migration. *PLoS computational biology* **2015**, *11* (10), e1004280. DOI: 10.1371/journal.pcbi.1004280.